MICROWAVE METAMATERIAL APPLICATIONS USING COMPLEMENTARY SPLIT RING RESONATORS AND HIGH GAIN RECTIFYING REFLECTARRAY FOR WIRELESS POWER TRANSMISSION

A Dissertation

by

CHI HYUNG AHN

Submitted to the Office of Graduate Studies of
Texas A&M University
in partial fulfillment of the requirements for the degree of

DOCTOR OF PHILOSOPHY

August 2010

Major Subject: Electrical Engineering

MICROWAVE METAMATERIAL APPLICATIONS USING COMPLEMENTARY SPLIT RING RESONATORS AND HIGH GAIN RECTIFYING REFLECTARRAY FOR WIRELESS POWER TRANSMISSION

A Dissertation

by

CHI HYUNG AHN

Submitted to the Office of Graduate Studies of
Texas A&M University
in partial fulfillment of the requirements for the degree of

DOCTOR OF PHILOSOPHY

Approved by:

Chair of Committee, Kai Chang
Committee Members, Robert D. Nevels
Laszlo Kish
Hae-Kwon Jeong
Head of Department, Costas N. Georghiades

August 2010

Major Subject: Electrical Engineering

ABSTRACT

Microwave Metamaterial Applications Using Complementary Split Ring Resonators and High Gain Rectifying Reflectarray for Wireless Power Transmission. (August 2010)

Chi Hyung Ahn, B.S., Inha University;

M.S., Pohang University of Science and Technology

Chair of Advisory Committee: Dr. Kai Chang

In the past decade, artificial materials have attracted considerable attention as potential solutions to meet the demands of modern microwave technology for simultaneously achieving component minimization and higher performance in mobile communications, medical, and optoelectronics applications. To realize this potential, more research on metamaterials is needed.

In this dissertation, new bandpass filter and diplexer as microwave metamaterial applications have been developed. Unlike the conventional complementary split ring (CSRR) filters, coupled lines are used to provide larger coupling capacitance, resulting in better bandpass characteristics with two CSRRs only. The modified bandpass filters are used to deisgn a compact diplexer. A new CSRR antenna fed by coplanar waveguide has also been developed as another metamaterial application. The rectangular shape CSRRs antenna achieves dual band frequency properties without any special matching network. The higher

resonant frequency is dominantly determined by the outer slot ring, while the lower resonant frequency is generated by the coupling between two CSRRs. The proposed antenna achieves about 35% size reduction, compared with the conventional slot antennas at the low resonant frequencies.

As a future alternative energy solution, space solar power transmission and wireless power transmission have received much attention. The design of efficient rectifying antennas called rectennas is very critical in the wireless power transmission system. The conventional method to obtain long distance range and high output power is to use a large antenna array in rectenna design. However, the use of array antennas has several problems: the relatively high loss of the array feed networks, difficultiy in feeding network design, and antenna radiator coupling that degrades rectenna array performance.

In this dissertation, to overcome the above problems, a reflectarray is used to build a rectenna system. The spatial feeding method of the reflectarray eliminates the energy loss and design complexity of a feeding network. A high gain rectifying antenna has been developed and located at the focal point of the reflectarray to receive the reflected RF singals and genterate DC power. The technologies are very useful for high power wireless power transmission applications.

DEDICATION

To my mother and the memory of my father,

my two sisters, and my lovely wife and son

ACKNOWLEDGMENTS

I would like to express my deepest appreciation to Dr. Kai Chang for his support and guidance throughout my Ph.D. education at Texas A&M University. I also appreciate Dr. Robert D. Nevels, Dr. Laszlo Kish, and Dr. Hae-Kwon Jeong for serving as my committee members and for their helpful comments.

I would also like to thank Mr. Ming-Yi Li for his technical assistance. I gratefully acknowledge Mr. Seongwon Oh, Mr. Jeongkyu Lee, Mr. Chanho Kim, Mr. Travis Eubanks, Mr. Jihyung Yu, Mr. Jonathan Hansen, Mr. Dongjin Jeong, and other members of the Electromagnetics and Microwaves Laboratory at Texas A&M University for invaluable discussions. I would also like to give special thanks to Yu-Juin Ren at RIM Inc., Dr. Chulmin Han at Ethetronics Inc. and Dr. Shih-Hsun Hsu at AOI Inc. for their helpful suggestions in the development of the technologies described in this dissertation.

Lastly, I would like to express my deep appreciation to my mother and my two sisters for their constant love, encouragement, and support. I also thank my son, Woojin for his love. Finally, my sincere thanks are given to my lovely wife, Soyoung, for all her patience, love, and support during my graduate studies.

TABLE OF CONTENTS

Page

CHAPTER Page

LIST OF FIGURES

FIGURE Page

FIGURE Page

FIGURE Page

FIGURE Page

LIST OF TABLES

TABLE Page

CHAPTER I

INTRODUCTION

1. Background

A. Left-Handed Metamaterials

This dissertation is divided into two main topics. Topic one covers metamaterial applications applied to novel microwave antenna and filter designs using complementary split ring resonators. Topic two covers a microwave rectifying reflectarray for wireless power transmission.

The history of metamaterials started in 1967 with a theoretical investigation by Russian physicist Viktor Veselago. One year later, the paper was published in English as *" The electrodynamics of substances with simultaneously negative values of* ε *and* μ *"* [1]. Veselago's hypothesis on the substances with negative dielectric constant and the negative magnetive permeability, which was called left-handed substances in the paper, leads to very unusual electromagnetic phenomenons; left-handed wave propagation and a negative refractive index as compared with ordinary materials. These unique electromagnetic characteristics were not investigated further because no realization of any artificial components with these properties hypothsized existed at that time. In 1998

This dissertation follows the style of IEEE Transactions on Microwave Theory and Techniques.

and 1999, J. B Pendry published two important papers about a thin wire component producing negative permittivity and positive permeability [2] and a split ring resonator (SRR) producing negative permeability and positive permittivity [3]. In 2000, he introduced the concept of superlenses, negative refractive index materials, which are able to reproduce perfect 2D images of both the propagating waves and evanescent waves of an object [4]. Pendry's contributions inspired the first left-handed structure realization. In 2000, D. R. Smith et al. [5] experimentally succeeded in synthesizing the first left-handed substance producing negative effective permittivity and permeability, 33 years after Veselago's hypothesis. This composite structure was combined of Pendry's two structures: a thin wire structure and a split ring resonator. This paper showed electromagnetic wave propagation experimentally at certain resonant band when effective ε and μ are both negative, and compared with the non propagation characteristics when one of the constants is negative. Finally, Smith and Shelby experimentally verificate a negative refracive index in 2001 [6].

In recent years, metamaterials have been greatly attentioned for many possible uses in microwave and optics fields. Many metamateiral applications about the backward coupler, phase compensation resulting in electrically small resonators, sub-wavelength waveguides with lateral dimensions below diffraction limits, and Čerenkov radiation, and doppler effect have been studied [7]-[14].

B.Wireless Power Transmission

The history of wireless power transmission started with a successful experiment by

Nikola Tesla [15] over a hundred year ago. He made it to transmit wireless power from his oscillators operating up to 100 MV at 150 KHz to two bulbs. From this success, several WPT studies had been conducted in Japan [16] and U.S. [17] in the 1920's and 1930's. In the 1950's, the development of high power and efficiency micrwave tube by Raytheon Company [18] opened the modern WPT era.

The first rectenna was invented in the 1960's by combining a half-wave dipole antenna and a single diode by W.C. Brown for 2.45GHz RF-to DC power conversion [19]. To achieve high conversion efficency, Brown later used a GaAs-Pt shottky barrier diode and aluminum bar dipole with 90.6 % conversion efficiency in 1977 [20].

The 1970's oil embargo encouraged the proposal for a solar power satellite (SPS) by P. E. Glaser [21] leaded great development on microwave power transmission technology. The SPS collects solar energy directily from space and transfers it to ground stations on the earth using microwave power transmission technology [22]-[23]. The possibiltiy of SPS as a future energy solution resulted in the great improvement of the rectenna technology.

The technology of a large-scale wireless power transmission are necessary for efficient SPS system, and normally many rectennas are combined into an array to rectify large amount of power. In 1975, the Jet Propulsion Laboratory and Raytheon built a 18 x 24 ft^2 rectenna array with 5000 elements working at 2.45 GHz [24]. A 30 kW output power of the rectenna array was achieved at a distance of one mile. In 1998, N. Shinohara in Japan built another 2.45 GHz rectenna array consisting of 2,294 dipoles for high power conversion [25]. In 2000, a dual-polarized rectenna array at 8.51 GHz was

developed by JPL with 50 V output [26]. In 2003, B. Strassner and K. Chang at Texas A&M University reported a C-band circularly polarized high efficency rectenna array with high gain rhombic loop antennas [27]-[28].

Several rectenna array types have been studied with high gain properties to achieve long distance WPT, higher DC power output, and reduced receiving areas. The rectenna array design has several challenges including design difficulties and the relatively high loss of array feeding networks, and antenna element coupling causing reduced rectenna array performance. A new rectenna array design method was necessary to overcome these challenges.

The rectenna array design presented in this dissertation combines a high gain single rectenna element with a reflectarray instead of array antenna elements. The reflectarray has several advantages over the parabolic reflector antenna (the most often used high gain antenna), such as: being flat, having a low-profile, and being easier to manufacture [29]-[30]. The reflectarray features can be adapted to a rectenna for the WPT system. The reflectarray normally achieves high gain and a feed network is not needed. A linearly polarized pentagonal loop rectenna with high gain can be used and placed at the reflectarray focal point to rectify the received microwave energy. The proposed novel rectenna array suggests a new type of long distance MPT system.

2. Dissertation Organization

This dissertation covers a variety of topics, consisting of microwave parallel coupled line bandpass filter and diplexer based on CSRRs, dual frequency CSRR

antenna fed by CPW, high gain rectifying reflectarray, wideband transition between coplanar stripline to double-sided parallel-strip line, dual band omni-directional antenna, and dual polarized conformal array antenna. Eight chapters comprise this dissertation.

Chapter II reviews the fundalmental theory of left-handed metamaterials with electromagnetic theories. Theoretical analysis for negative phase constant, negative phase velocity, and negative index of refraction in DNG medium are described. Then realization of metamaterial components, especially for SRR and CSRR, are presented.

Chapter III introduces a new design for microwave compact bandpass filter and diplexer based on complementary split ring resonators. The parallel coupled transmission lines on one CSRR is analyzed with its equivalent circuit model. Then a compact bandpass filter design using dual CSRRs is discussed. This bandpass filter does not need multi-casecades for improved bandpass characteristics. Finally, based on the CSRR bandpass filter design concept, a compact microwave diplexer casecading two parallel coupled line CSRR filters is proposed.

Chapter IV presents a novel complementary split ring resonator antenna fed by complanar waveguide. Two concentric slot rings with split generate dual resonating frequencies at 2.6 GHz and 4.5 GHz. The CPW fed slot antenna does not need any special matching networks for good impedance matching. For better understanding of the proposed antenna's characteristics, several design parameters are analyzed.

Chapter V reviews WPT system and rectenna operation theory. A high gain rectenna based on CPS structrue is presented. A dual pentagonal loop antenna generates a high gain of 10.2 dBi. The proposed antenna is used for a cominbed rectifying

reflectarray as a feed antenna. Maximum conversion efficiency of the single element is 75%.

Chapter VI discusses a new rectifying array antenna combining a reflectarry with 23 x 24 elements of a high gain 5.8 GHz rectenna element. The reflectarray with compact unit cells, a combination of inner circlular patch and outer ring, is discussed. A rectenna element located at the focal point of the reflectarray consists of 2X1 pentagonal loop antennas. The proposed rectenna element shows 10.2 dBi high gain at 5.8 GHz. The performances of combination of a reflectarray and a rectenna element is presented. The conversion efficiency of the rectifying reflectarray goes up to 71 %.

Chapter VII introduces two microwave applications. By using the basic theory of double-sided parallel-strip line (DSPSL), wideband CPS to DSPSL transition is developed. The transition achieves low insertion loss from 2.4 GHz to 10.7 GHz. A dual frequency omni-directional antenna is discussed. The antenna provides horizontally polarized radiation patterns, which is useful for polarization diversity application for MIMO systems.

Chapter VIII concludes this dissertation with a summary, discussion of the research accomplishments, and recommendations for future studies.

CHAPTER II

FUNDAMENTALS OF METAMATERIALS

1. Introduction

Metamaterials are defined as artificial effectively homogenous electromagnetic structures with unusual properties not readily available in nature. More than 40 years have passed since Veselago's first theoretical investigation [1] of left-handed material simulatenously exhibiting negative permittivity and permeability. In the last decade, the artificial materials have attracted considerable attention as potentional solutions to meet the demands of modern microwave technology for simultaneously achieving component minimization and higher performances in mobile communications, medical, and optoelectronics applications [31]-[35].

2. Fundamentals of Metamaterials

To understand the fundamentals of left-handed metamaterials exhibiting antiparallelism between the phase and group velocities, and negative refractive index in left-handed materials, Maxwell's equations are reiterated in the frequency domain.

$$\nabla \times \overline{E} = -j\omega \overline{B} - \overline{M} \tag{1}$$

$$\nabla \times \overline{H} = -j\omega \overline{D} + \overline{J} \tag{2}$$

$$\nabla \times \overline{D} = \rho_e \tag{3}$$

$$\nabla \times \overline{B} = \rho_M \tag{4}$$

where $\overline{E}$ [V/m] and $\overline{H}$ [H/m] are the electric and magnetic field intensity, respectively, and $\overline{D}$ [C/m^2] and $\overline{B}$ [W/m^2] are the electric and magnetic flux density, respectively, $\overline{J}$ [A/m^2] and $\overline{M}$ [V/m^2] are the electric and magnetic current density, respectively, and ρ_e [C/m^3] and ρ_m [C/m^3] are the electric and magnetic charge density, respectively. In linear and nondispersive medium, the constituitive equations are given by

$$\overline{D} = \varepsilon_0 \varepsilon_r \overline{E} = \varepsilon_0 (\varepsilon_r^{'} - j\varepsilon_r^{''}) \overline{E} \tag{5}$$

$$\overline{B} = \mu_0 \mu_r \overline{H} = \mu_0 (\mu_r^{'} - j\mu_r^{''}) \overline{H} \tag{6}$$

where $\varepsilon_0 = 8.854 \times 10^{-12}$ [F/m] is the permittivity and $\mu_0 = 4\pi \times 10^{-7}$ [H/m] is the permeability of free space, and $\varepsilon_r^{'}$ and $\mu_r^{'}$ are the medium's relative permittivity and permeability, respectively, and $\varepsilon_r^{''}$ and $\mu_r^{''}$ are the losses in ε_r and μ_r, respectively, due to dielectric and magnetic damping and finite conductivity. Note that $\varepsilon_r^{''}$ and $\mu_r^{''}$ must be positive due to the conservation of energy.

For simplicity, the medium is lossless ($\varepsilon_r^{''} = 0$, $\mu_r^{''} = 0$) in source free ($\overline{M} = 0$, $\overline{J} = 0$) region. From Maxwell's equations, Helmholtz's equations to obtain $\overline{E}$ and $\overline{H}$ can be expressed as

$$\nabla^2 \overline{E} + k^2 \overline{E} = 0 \tag{7}$$

$$\nabla^2 \overline{H} + k^2 \overline{H} = 0 \tag{8}$$

where $k^2 = \omega^2 \varepsilon \ \mu$ is the propagation constant. The propagation constant can be defined

for the medium as $k=\alpha+j\beta$ where α is the attenuation constant and β is the phase constant. In the lossless case, $\alpha=0$ and $k=j\beta$. Phase constant β is expressed by

$$\beta=\pm\omega\sqrt{\varepsilon\mu} \tag{9}$$

With the equations above, observation shows how medium characteristics (ε_r , μ_r) affect electromagnetic fields (α , β) traveling through the medium in four different cases.

A. Double Positive (DPS) Medium ($\varepsilon_r > 0$, $\mu_r > 0$)

When $\varepsilon_r > 0$ and $\mu_r > 0$, phase constant in equation (9) is

$$\beta=+\omega\sqrt{\varepsilon\mu} \tag{10}$$

By substituting the expressinos of the plane wave in these mediums into the first two Maxwell's equations, the following relations among the wave vector, the electric intensities, and magnetic intenisities are obtained.

$$\overline{\beta}\times\overline{E}=+\omega\mu\overline{H} \tag{11}$$

$$\overline{\beta}\times\overline{H}=-\omega\varepsilon\overline{E} \tag{12}$$

These results show that the electric field intensity $\overline{E}$, the magnetic field intensity $\overline{H}$, and the wave vector $\overline{\beta}$ build a right-handed triad.

B. Double Negative (DNG) Medium ($\varepsilon_r < 0$, $\mu_r < 0$)

When $\varepsilon_r < 0$ and $\mu_r < 0$, phase constant and field relations are

$$\beta=-\omega\sqrt{\left|\varepsilon'\right|\left|\mu'\right|}\,. \tag{13}$$

$$\overline{\beta} \times \overline{E} = -\omega |\mu| \overline{H} \tag{14}$$

$$\overline{\beta} \times \overline{H} = +\omega |\varepsilon| \overline{E} \tag{15}$$

These results indicate that in DNG medium, the electric field intensity $\overline{E}$, the magnetic field intensity $\overline{H}$, and the wave vector $\overline{\beta}$ build a left-handed triad.

C. Epsilon Negative (ENG) ($\varepsilon_r < 0$, $\mu_r > 0$) & Mu Negative (MNG) ($\varepsilon_r > 0$, $\mu_r < 0$) Medium

In the ENG case ($\varepsilon_r < 0$ and $\mu_r < 0$) or MNG ($\varepsilon_r > 0$, $\mu_r < 0$), both phase constants are

$$\beta = 0 \tag{16}$$

which means that the waves in this medium become evanescent waves and do not propagate ($\beta = 0$). The phase velocity in a medium is defined as

$$v_p = \frac{\omega}{\beta} \tag{17}$$

The case studies show that the phase constant β in a left-handed medium (DNG) is negative since the phase constant is positive in DPS medium, and phase velocity v_p in DNG becomes negative and v_p becomes positive in DPS medium. All lossless materials in terms of the signs of permittivity ε_r and permeability μ_r can be classified as shown in Figure 1.

Another interesting characteristic with negative phase constant can be found with the following equation.

$$\beta = nk_0 = n\frac{\omega}{c} \tag{18}$$

where refractive index n is

$$n = \pm\sqrt{\varepsilon_r \mu_r} \tag{19}$$

These equations indicate that the refractive index becomes negative in a DNG medium (negative permittivity and negative permeability) due to negative phase constant while it is positive in a DPS medium.

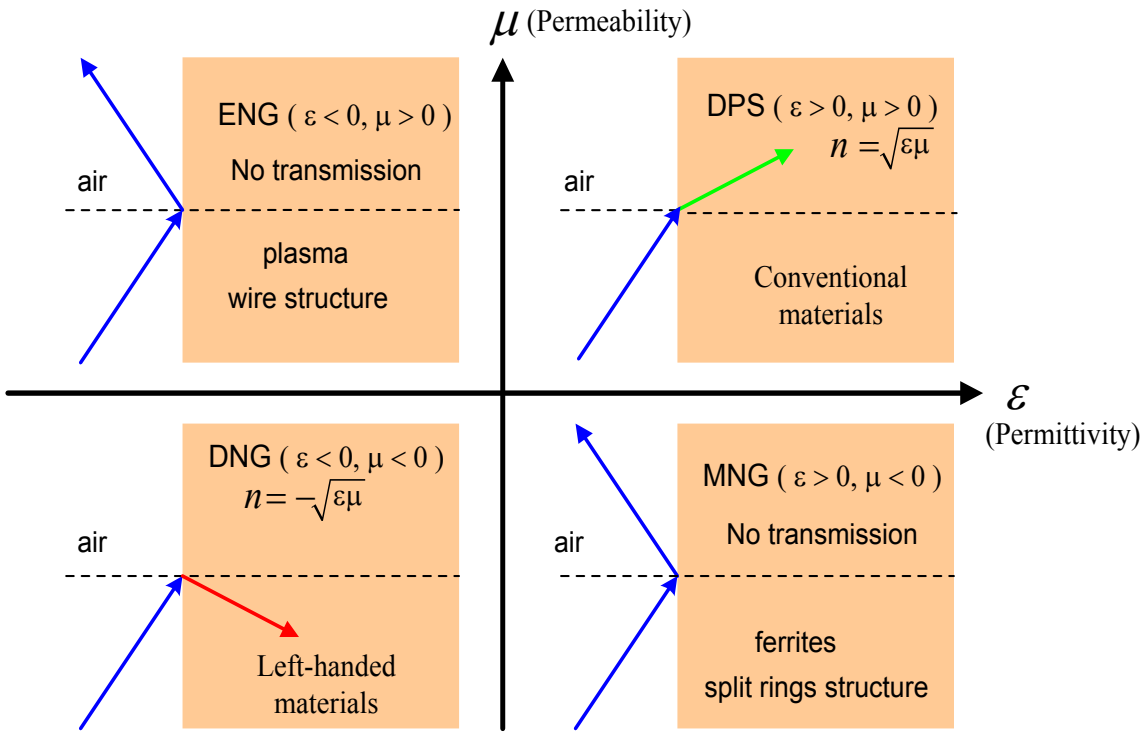

Fig. 1. Classifcation of materials (DPS : double positive, ENG: epsilon negative, DNG: double negative, MNG: mu negative)

3. Metamaterial Resonators – SRR/CSRR

The first 'split ring resonator' was invented by Hardy [36] in 1981 as shown in Figure 2(a). The structure consists of two metallic tubes with a split on inner tube only. The gap between two tubes increases capacitance and the outer tube impounds the magnetic field to make outer region magnetic flux equal to the inner region magnetic flux as

$$BS_O = -BS_i \tag{20}$$

Where $S_i = \pi R_i^2$, $S_o = \pi [R_o^2 - (R_i + w)^2]$ and w is the inner tube thickness and R_o and R_i are the radii of the outer and inner structures, respectively. The resonant frequency of the split ring tube resonator can be determined as

$$W_O = \sqrt{1 + \frac{S_i}{S_o}} \sqrt{\frac{g}{\pi} w} \frac{c}{R_i} \tag{21}$$

where g is the split width. This structure, based on the analytical equation, was available

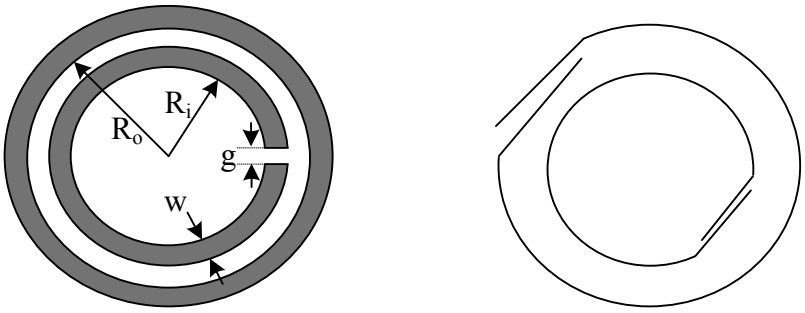

(a) (b)

Fig. 2. Structures of (a) the first SRR tube and (b) early SRR element

from 20 MHz to 2 GHz. A frequency range extension to 4 GHz was researched by Zonta [37]. In 1993, another metallic element to achieve artificial medium effect was introduced [38] shown in Figure 2 (b). Metallic structure resonance was achieved by combining capacitance and inductance configurations.

Pendry in 1999 [3] introduced a conducting non-magnetic ring array, which became popular metamaterial components called SRRs. The difference from other early elements in configuration is that Pendry's structure consists of two concentric rings with splits on opposite sides as shown in Figure 3 (a). Inductance from the structure can be obtained by each ring itself or their mutual combination. Capacitance can be controlled by gap between rings or split gap. For simplicity, the gap capacitance and mutual inductance are ignored since they don't affect the current flow significantly. More simplification is possible when the self-inductance of each ring is equal to the average value of the two rings. From the assumption, the resonant frequency of a SRR structure

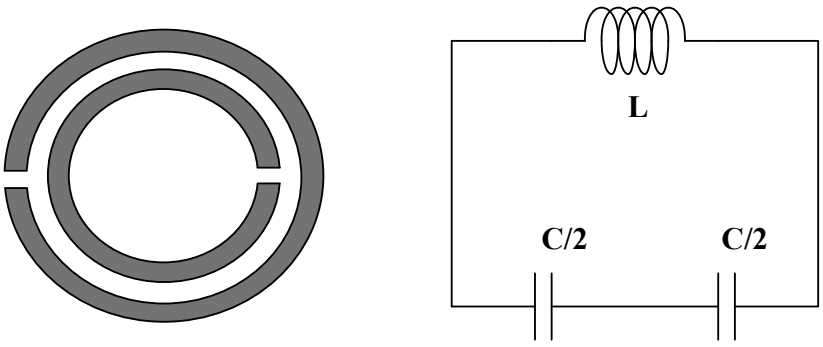

(a) (b)

Fig. 3. (a) Pendry's SRR and (b) its simplified equivalent circuit

can be expressed [39] as

$$\omega_O{}^2 \approx \frac{2}{\pi R_{ave} LC'} \tag{22}$$

where L is the average inductance of the two rings and C' is the inter-ring capacitance per unit length. R_{ave} is the average radius of the SRR. Equation (22) indicates the SRR can be considered a LC resonant circuit in Figure 3 (b).

More sophisticated and exact equivalent models to represent the properties of the SRR have been reported [40]-[48]. In [41], the sophisticated equivalent model of the SRR structure was described in Figure 4 (a). The entire structure can be considered a composition of the cascaded dφ elements shown in Figure 4 (b). By Kirchhoff's laws for the unit cell structure, the currents for the upper line can be expressed as

$$I_1(\varphi + d\varphi) = I_1(\varphi) - I_c(\varphi) \tag{23}$$

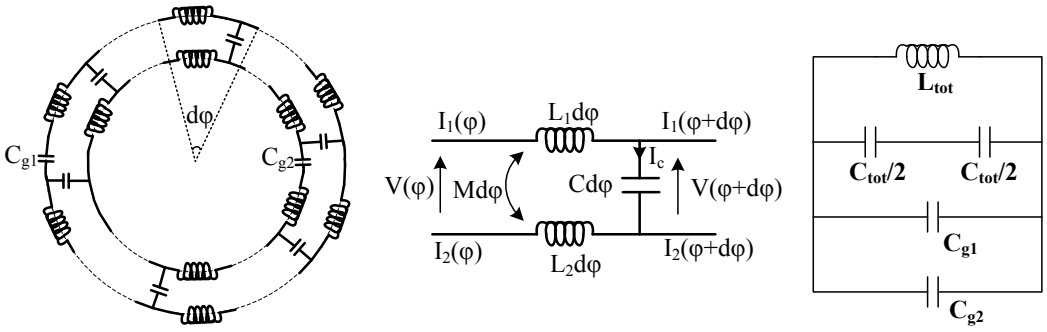

(a) (b) (c)

Fig. 4. (a) The sophisticated equivalent model of the SRR, (b) its unit cell model, and (c) solved equivalent circuit of the SRR

where $I_c(\varphi) = j\omega CV(\varphi)$, V(φ) is the voltage across the ring and C is the capacitance of the inter-ring per unit radian. The currents for the lower line can be expressed as

$$I_2(\varphi + d\varphi) = I_2(\varphi) + I_c(\varphi) \tag{24}$$

From the equation (23) and (24), the differential equations can be obtained as

$$\frac{dI_1}{d\varphi} = -j\omega CV \tag{25}$$

$$\frac{dI_2}{d\varphi} = j\omega CV \tag{26}$$

Similarly, voltage equation can be derived as

$$V(\varphi + d\varphi) = V(\varphi) + I_1 Z_1 - j\omega MI_1 - I_2 Z_2 + j\omega MI_2 + \frac{F_1 - F_2}{2\pi} \tag{27}$$

where $Z_1 = R_1 + jwL_1$, $Z_2 = R_2 + jwL_2$ and the induced voltages of the outer ring and inner ring are $F_1 = jw\mu_o H\pi r_1^2$ and $F_2 = jw\mu_o H\pi r_2^2$, respectively. The approximate solution from the equations (25) - (27) can be finally expressed as

$$\omega^2 = \frac{1}{L_{tot}(\frac{C_{tot}}{4} + C_{g1} + C_{g2})} \tag{28}$$

where $L_{tot} = 2\pi L$ and $C_{tot} = 2\pi C$. The final equation (28) indicates that the SRR resonant frequency can be expressed by the circuit model in Figure 4 (c). Equation (28) is a generalized and simplified form of equation (22). It is important to note that the SRR structures should have proper field orientation which enables currents to flow strongly on the structure. The SRR axis should be parallel to the electromagnetic wave H field.

Another resonator named complementary split ring resonator (CSRR) as shown

in Figure 5 (a) was introduced by Falcone [49] in 2004. The properties of the CSRRs show duals of those of the SRRs. The SRR behaves as a magnetic dipole and the CSRR works as an electric dipole. The equivalent circuit model shown in Figure 5 (b) has approximately the same configuration with the SRR's model. Due to the near elements coupling, additional capacitance C_M is added. CSRR is excited by the E-field, the axis of the CSRR should be parallel to the E-field. The CSRR resonant frequency can be obtained by

$$\omega_O{}^2 \approx \frac{2}{\pi LC'} \tag{29}$$

where L and C' are the inter slot ring capacitance and inductance per unit length, respectively. By tuning the CSRR geometry, the capacitance and inductance values can be controlled.

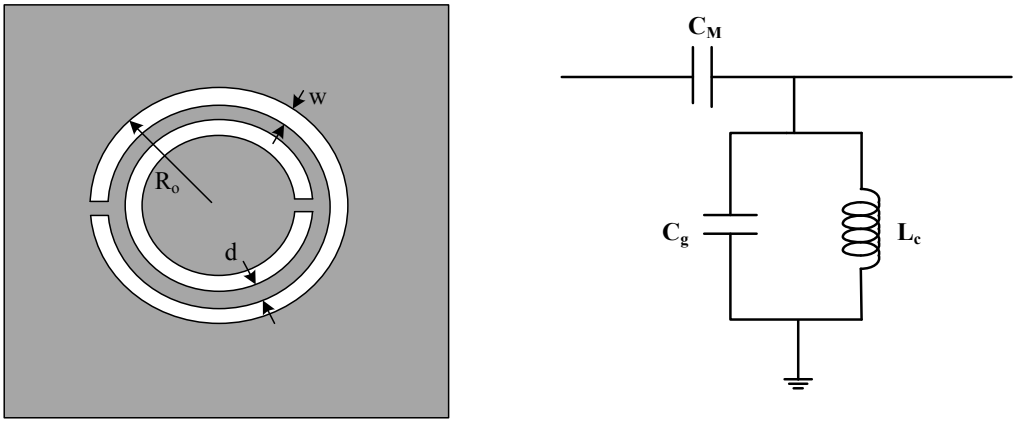

(a) (b)

Fig. 5. (a) CSRR structure and (b) its equivalent model

4. Summary

In this chapter, fundamentals of left-handed metamaterials are described. From Maxwell's equations, phase constant term is derived and it is clearly shown that its negative value is selected in a negative permittivity and negative permeability (DNG) medium while its positive value is selected in a DPS medium. The negative phase constant results in negative phase velocity and negative index of refraction in the medium.

Among many successful metamaterials, split ring resonator (SRR), which is one part of the first realized left-handed metamaterial in 2000, and complementary split ring resonator (CSRR) are described. The resonant frequencies of the SRR and CSRR are strongly related with the dimensions of their structures. For excitation of SRR structure, the H field of the electromagnetic wave has to be along (parallel) the axis of the SRR in order to induce the current through the rings. Due to the duality, CSRR is excited with the E field of the electromagnetic wave along with the axis of the CSRR. As a results, the CSRR exhibits negative permittivity while SRR have negative permeability in a certain frequency band.

CHAPTER III

COMPACT PARALLEL COUPLED LINE BAND-PASS FILTER AND DIPLEXER USING COMPLEMENTARY SPLIT RING RESONATORS

1. Introduction

Compact bandpass filters with low insertion loss (IL), sharp cutoff, and low cost are indispensible in modern wireless communication systems. Microstrip parallel coupled line resonators are commonly used for bandpass filter design due to their low cost, ease of fabrication, and simple design procedure [50]. However, most parallel coupled line bandpass filters are not of compact size because they are made up of sections of quarter or half wavelength resonators which results in a large size [51].

Recently, complementary split ring resonators (CSRRs) have been of great interest as key metamaterial components in microwave filter design [49], [52]. In the beginning, many low pass filters have been reported using CSRRs for compact size and harmonic suppressions [53]. In [54], a CSRR BPF with series gap on microstrip line was introduced but with at least 4 periodic series unit cells. Compact, low insertion loss BPFs were also reported; however they have complicated configurations with grounded via holes [55] or combinations of both low pass filter and high pass filter designs [56].

In this chapter, a compact CSRR BPF structure with simpler design procedures is proposed. Using a parallel coupled gap instead of conventional series gaps on

transmission line [54], [56] is suggested for simple and compact BPF design. A Double CSRR is proposed for better bandpass characteristics. This configuration can be applied for many other filter designs due to its simple and compact configuration.

2. Single CSRR Resonator and Its Equivalent Circuit

Figure 6 shows the single CSRR structures with series coupling feed lines (a) and parallel coupling feed lines (b). The equivalent circuit model for both series and parallel gap CSRR structures is shown in Figure 7. The LC tank consisting of inductance L_r and capacitance C_r models the CSRR etched in the ground plane. C_c is the coupling capacitance between the transmission line and CSRR. C_g is the gap capacitance between the two separated microstrip feed lines and L_t is the transmission line inductance. The return and transmission responses of the proposed configuration (Figure 6 (b)) are given by

$$S_{11} = \frac{2Z_p Z_s + Z_s^2 - Z_0^2}{(Z_s + Z_0 + 2Z_p)(Z_s + Z_0)} \tag{30}$$

$$S_{21} = \frac{2Z_p Z_0}{(Z_s + Z_0 + 2Z_p)(Z_s + Z_0)} \tag{31}$$

where $Z_s = (1-\omega^2 L_t C_g)/j\omega C_g$ and $Z_p = \{1-\omega^2 L_r(C_r+C_c)\}/j\omega C_c\,(1-\omega^2 L_t C_r)$ is the impedance of the series branch and the parallel branch, respectively, of the equivalent circuit in Figure 7. Z_0 is the characteristic impedance of the feed line. The lumped element values can be found using a full wave EM simulation, IE3D, of the structures in Figure 6 as in [49].

By comparing the CSRR equivalent circuit with the prototype circuit model of a BPF unit cell which has a combination of series LC and parallel LC components, one can see that the value of C_c should be large to ignore the impedance of C_c and the value of C_g should be small to retain its impedance. Figure 8 shows the trends in varying the values of C_c and C_g by using different microstrip line configurations. Extracted lumped

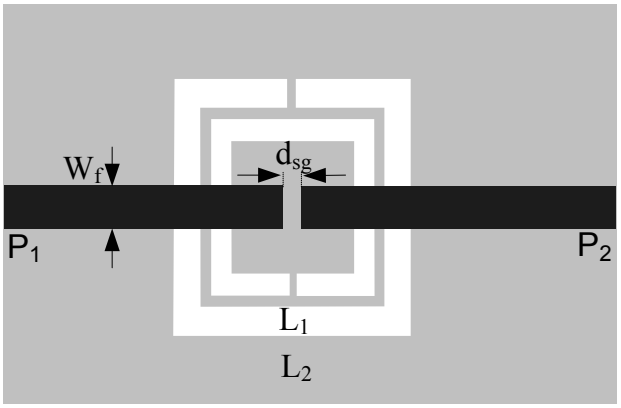

(a)

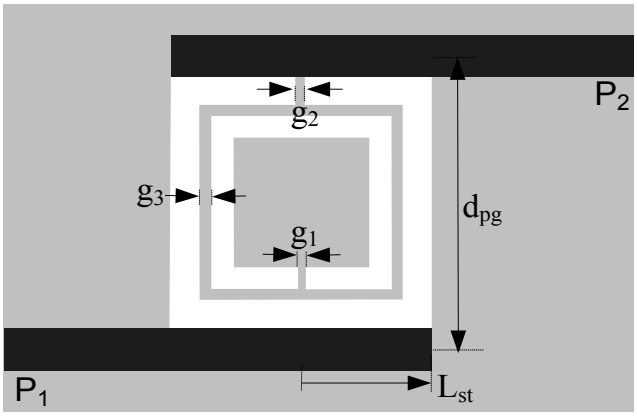

(b)

Fig. 6. (a) Unit cell of conventional CSRR BPFs with series coupling feed lines and (b) the proposed single CSRR structure with parallel coupling feed lines (Black and white part represents microstrip lines on top and etched CSRR on ground plane, respectively.)

element values are listed in Table 1. In Figure 8 (a), the gap distance, d_{sg}, of the series feed lines in Figure 6 (a) is changed to study the effect of series gap capacitance, C_g. As the gap distance, d_{sg}, increases, the decreased C_g value has better bandpass response. However, the value of C_c also becomes smaller at the same time, which prevents the unit cell of the series gap structure from having good BPF characteristics. Therefore, the conventional series gap structures have been replaced by parallel coupling feed lines shown in Figure 6 (b) to achieve good bandpass response. Figure 8 (b) shows the effects of C_c, the coupling capacitance between microstrip line and CSRRs, by varying the feed stub length, L_{st}, and the parallel coupling gap, d_{pg}, in Figure 6 (b). As L_{st} increases, the coupling area between transmission line and CSRRs increases. The increased coupling region results in the larger coupling capacitance, C_c, with better bandpass response

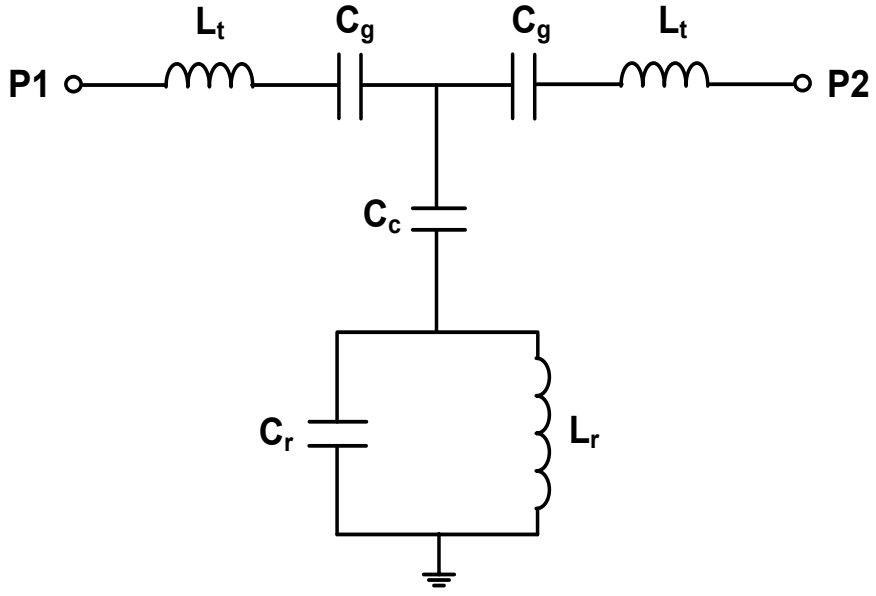

Fig. 7. Equivalent circuit model of the structures in Fig. 6

shown in Figure 8 (b). The values of C_g are also controlled by the coupling gap distance, d_{pg}. One can see that the gap capacitance, C_g, becomes smaller as C_c values are increased in Table I. As evident from Figure 8 and Table I, the proposed parallel coupled lines can offer small C_g and large C_c by increasing gap distance and feed stub length, respectively, to obtain good bandpass response.

TABLE 1

Extracted Lumped Elements (L_1 = 4.68 mm, L_2 = 7.2 mm, g_1 = 0.18 mm, g_2 = 0.36 mm, g_3 = 0.36 mm, W_f = 1.6 mm)

	Cg (pF)	Lr (nH)	Cr (pF)	Lt (nH)	Cc (pF)
Fig. 3 (a) d_{sg} = 0.5 mm	0.4	2	0.4	1.6	21
Fig. 3 (a) d_{sg} = 2.5 mm	0.25	2	0.38	1.3	18
Fig. 3 (a) d_{sg} = 4.5 mm	0.15	2	0.38	1.1	12
Fig. 3 (b) L_{st} = -2.5 mm, d_{pg}= 5.2 mm	0.22	2.2	0.39	1.2	12
Fig. 3 (b) L_{st} = 0.5 mm, d_{pg} = 6.2 mm	0.15	2.1	0.38	1.4	17
Fig. 3 (b) L_{st} = 3.5 mm, d_{pg} = 8.2 mm	0.07	2.1	0.38	1.6	21

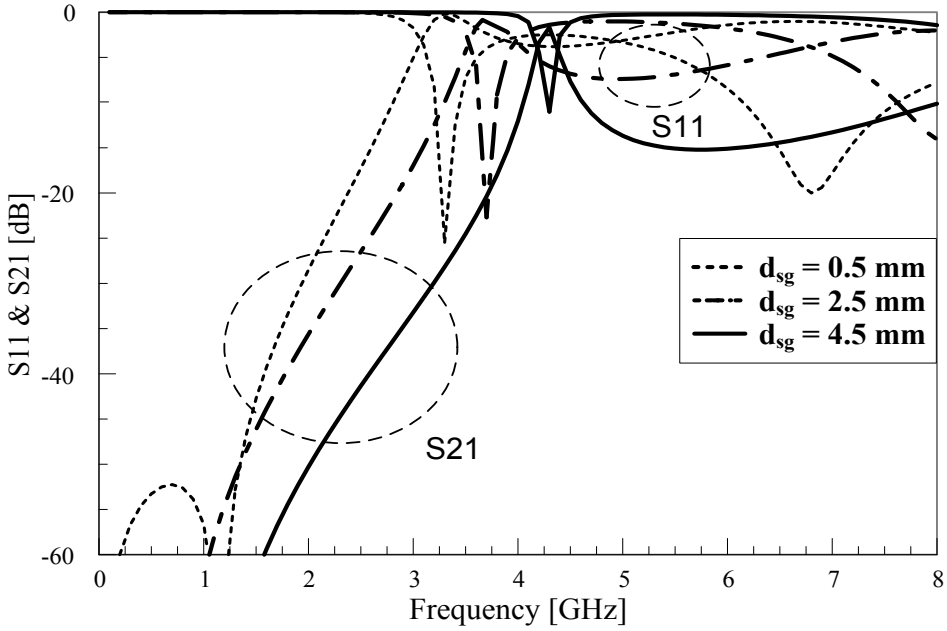

(a)

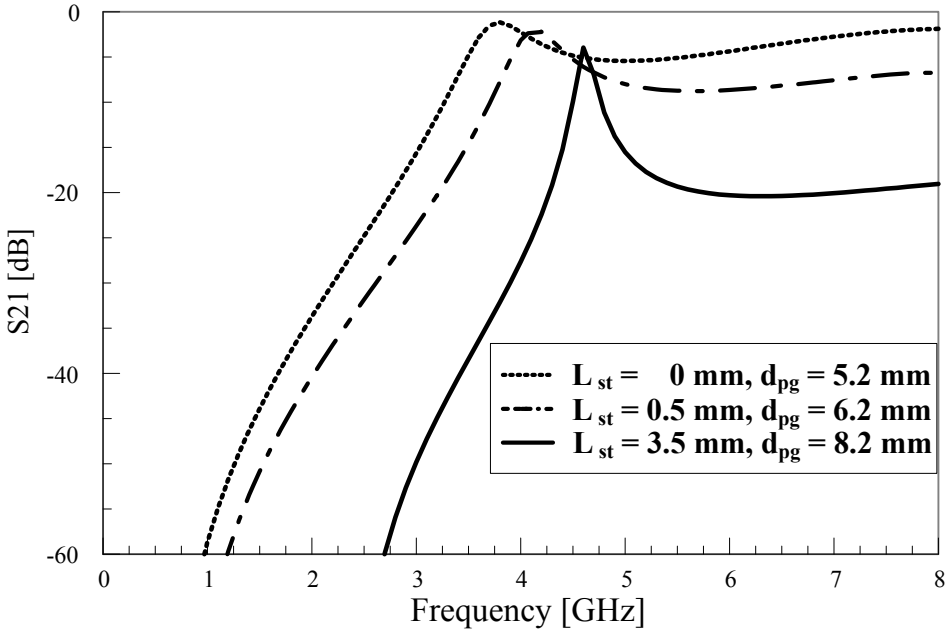

(b)

Fig. 8. Simulated results of different (a) series gap distances and (b) microstrip line stub lengths

3. Compact Band-Pass Filter Design

A good bandpass response with a slightly high insertion loss by a single CSRR structure with parallel microstrip feed lines has been shown in the last section. Now we propose a double CSRR bandpass filter for better insertion loss at around resonant frequency. Figure 9 shows the configuration of the proposed double CSRRs BPF which consists of the same two CSRRs located next to each other and parallel microstrip feed lines. To obtain better bandpass response, two design parameters on the configuration have been studied simply by EM simulation, IE3D. The effect of the feed stub length, L_{st}, is shown in Figure 10 (a). As L_{st} increases from the 0 to 8 mm, the characteristics of the S parameters of the bandpass filter become better. However, the longer feed stub length will prevent the filter minimization, so proper length should be investigated. The parallel coupled gap distance, d_{pg}, is also an important design parameter. Figure 10 (b) shows the effect of the gap distance by varying from 6.5 mm to 8.5 mm. As expected, it shows a tight coupling effect of the wide bandpass region when the d_{pg} becomes smaller and a loose coupling effect of narrow bandpass as the coupling gap distance increases. The gap distance between two CSRRs, g_4, is fixed at 0.2 mm because this parameter is not dominant for the filter responses.

From the design parameter study, a prototype double CSRRs BPF has been designedusing both equivalent circuit and EM simulation. The filter has been fabricated on substrate RT/Duroid 5880 with thickness and a dielectric constant of 20 mil (0.508mm) and 2.2, respectively. Measurements have been carried out using the HP8510C network analyzer. Figure 11 shows that the measured and simulated results of

the prototype BPF are matched well with each other. The measured insertion loss of 1.4 dB has been achieved at 3.6 GHz.

A novel technique using parallel coupled microstrip lines on the etched part of CSRRs is proposed to design a compact bandpass filter with simple structure. The proposed technique increases coupling capacitance between microstrip feed lines and CSRRs, and decreases the capacitance between two microstrip feed lines. These characteristics lead to a better bandpass response in a compact and simple structure. Compared with other conventional CSRRs BPFs, the proposed simple BPF does not need cascaded periodic unit cells [54], any grounded via holes[49], or another type of filter section combined together [56]. The measured insertion loss of the prototype BPF is 1.4dB with a compact size of 0.35 λg x 0.14 λg.

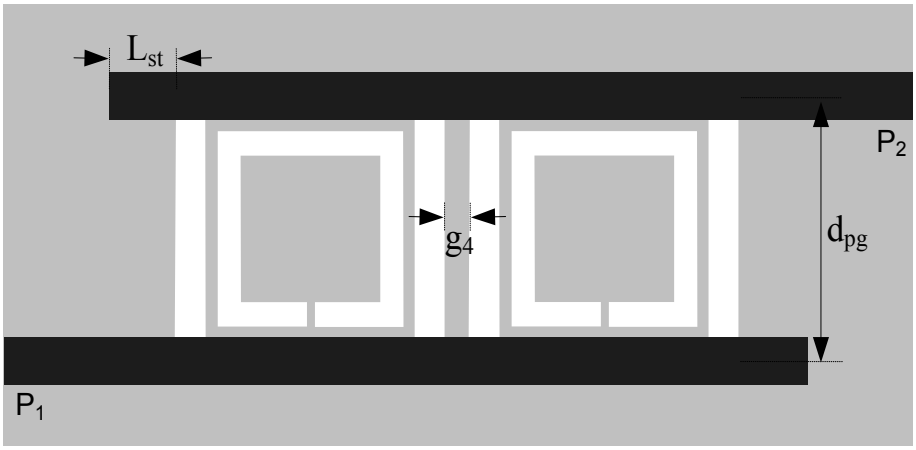

Fig. 9. The proposed double CSRR bandpass filter (L_1 = 5.4 mm, L_1 = 8 mm, g_1 = 0.2 mm, g_2 = 0.36 mm, g_3 = 0.5 mm, g_4 = 0.2 mm, W_f = 1.6 mm)

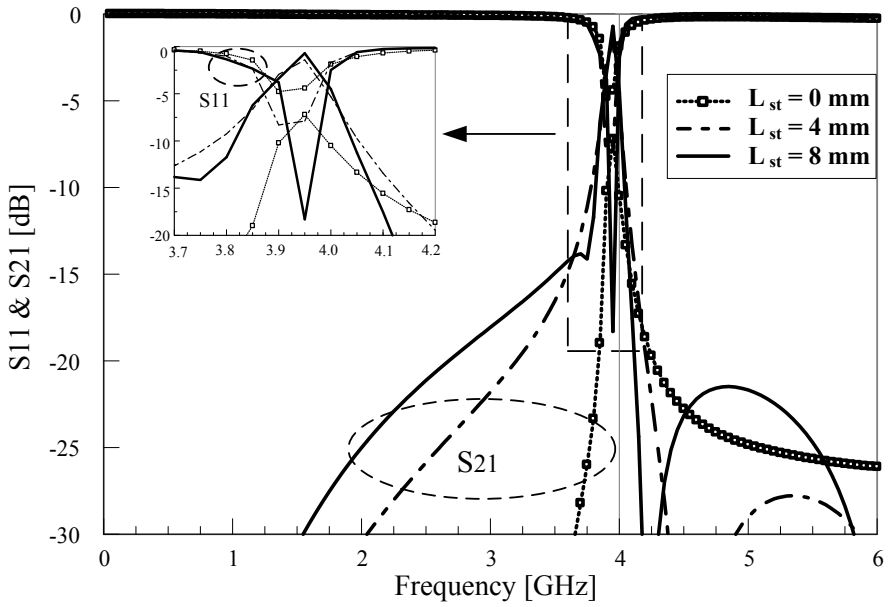

(a)

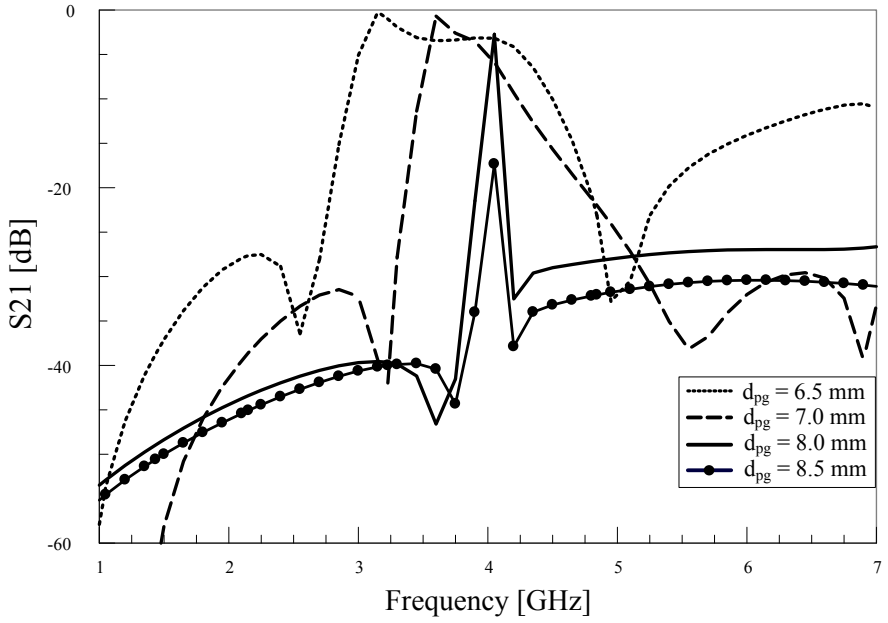

(b)

Fig. 10. Simulation results of (a) open stub length effect and (b) parallel coupled gap distance effect

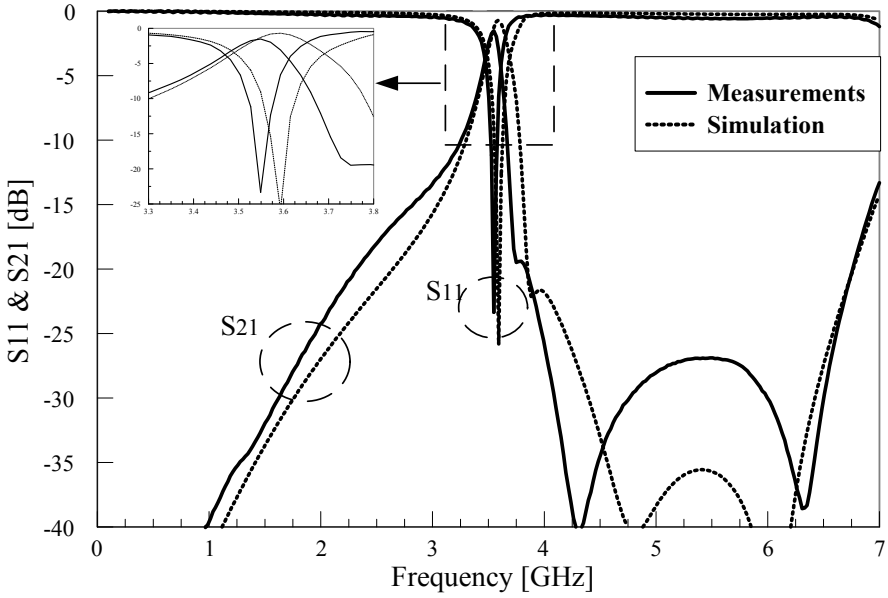

Fig. 11. Measured and simulated results of a prototype double CSRRs BPF

Figue 12 shows pictures of the proposed bandpass filter. The proposed technique using parallel coupled microstrip lines with CSRRS is verified by measurements. The methods should have potential applications for other types of microwave filter designs.

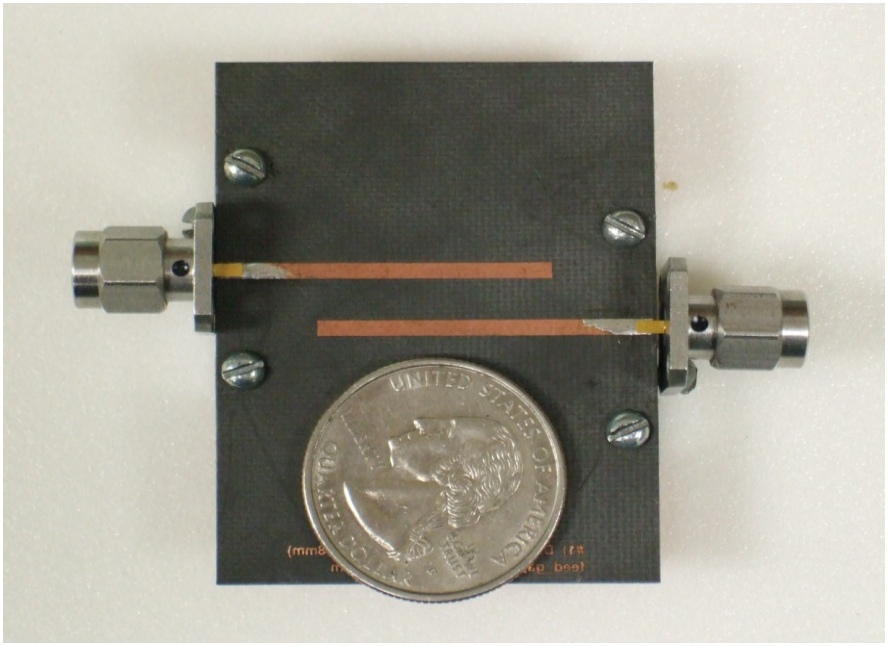

(a)

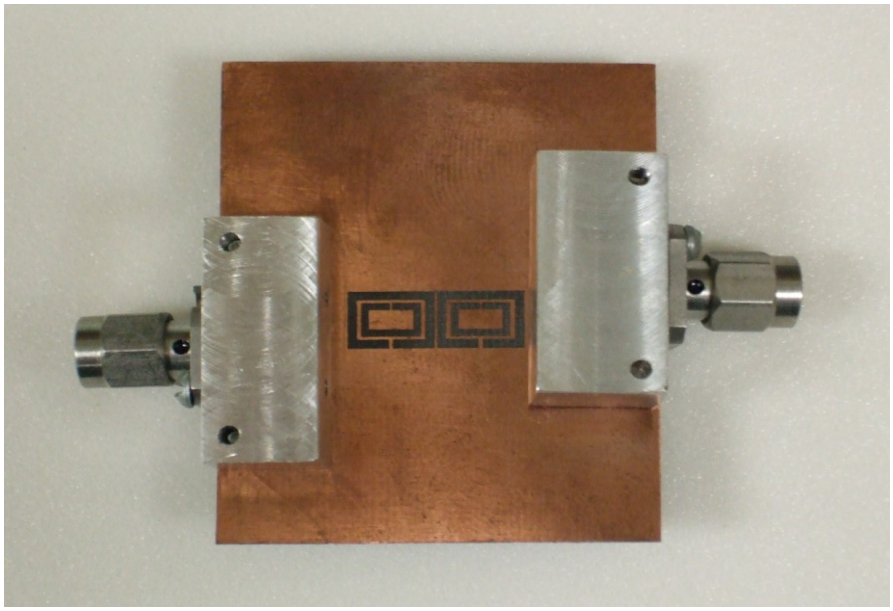

(b)

Fig. 12. Pictures of double CSRRs BPF: (a) front view and (b) backside view

4. Diplexer Design Based on CSRRs

In this chapter, the concept of the CSRR bandpass filter is applied to the design of a compact microwave diplexer. The diplexer is one of the important RF front end components in multiservice and multiband communication systems. Figure 12 shows general schematic of a diplexer, which consists of two bandpass filters with different passband regions [51]. The classic design procedure of diplexers is required to design two bandpass filters and a three-port junction, such as T or Y junctions, separately and combined them with impedance transformers. This design method leads to unavoidable increase in the total system size.

A novel compact microwave diplexer based on complemetary split ring resonators is proposed in this chapter. A prototype and its simulated results of a bandpass filter presented in the previous chapter is shown with four ports at each parallel coupled line ends in Figure 14 (a) and (b), respectively. The electromagnetic fields pass from port 1 to port 2 at only a specific band which is resonant frequency point.

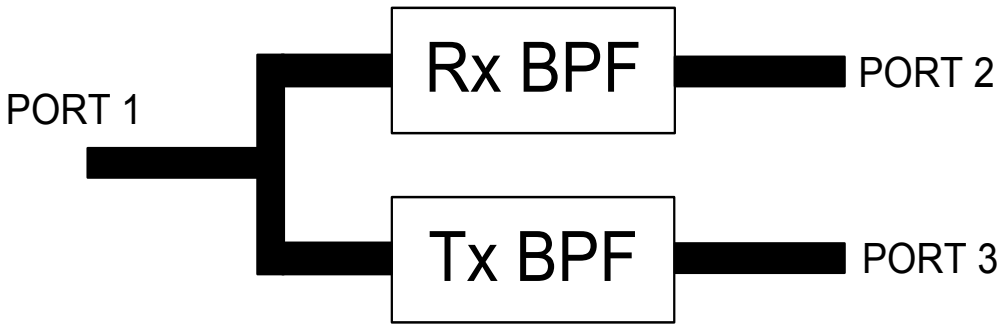

Fig. 13. Diplexer schematic

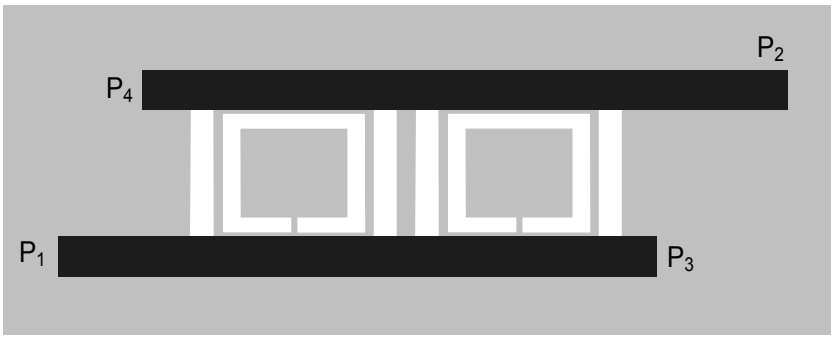

(a)

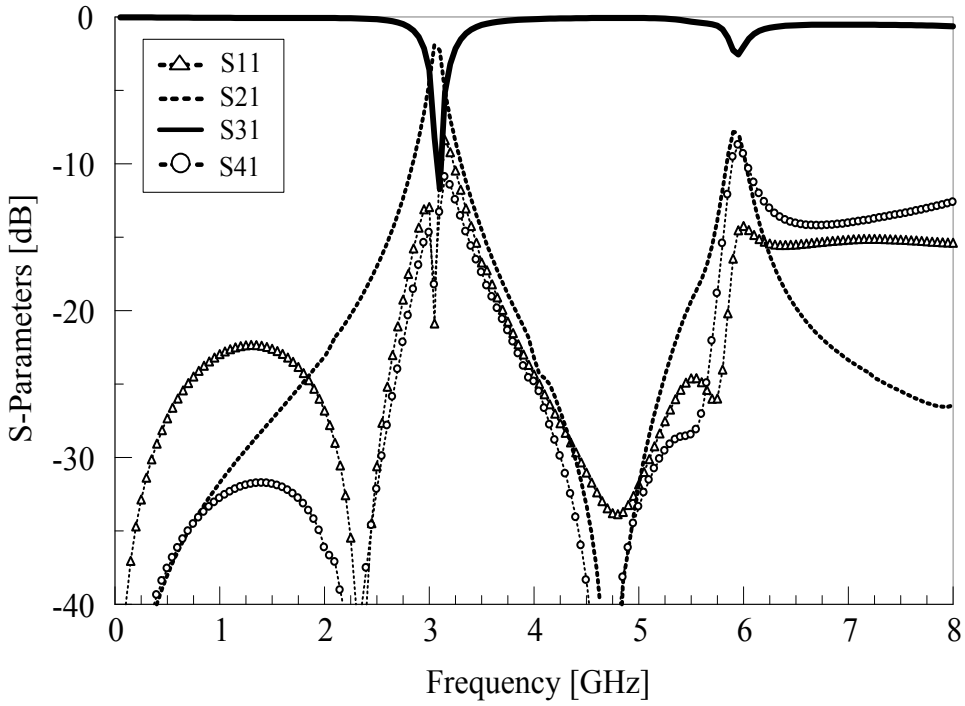

(b)

Fig. 14. (a) Structure of a CSRR BPF with four ports and (b) its simulated results

The result means that the component works as a bandpass filter for port 1 to port 2. It is also seen from the results of port 1 & port 3 that the electromagnetic waves pass all

frequency regions except a specfic band. From the interesting results, diplexer can be designed by combining two parallel coupled bandpass filters.

Two bandpass filters are designed for the center frequency of 3.1 GHz and 4.2 GHz, respectively. The filter centered at 3.1 GHz is denoeted as TX filter and the filter with center frequency of 4.2 GHz is denoted as RX filter. Every simulation and optimization was done using IE3D, a full-wave electromagnetic simulator. Figure 15 shows the simulated results of the bandpass filters. The TX filter has the insertion loss of about 0.7 dB and return loss of 16 dB at 3.1 GHz. The RX filter has the insertion loss of about 1.4 dB and return loss of 17 dB at 4.2 GHz. The rejection of the filters at each other's passband is more than 35 dB.

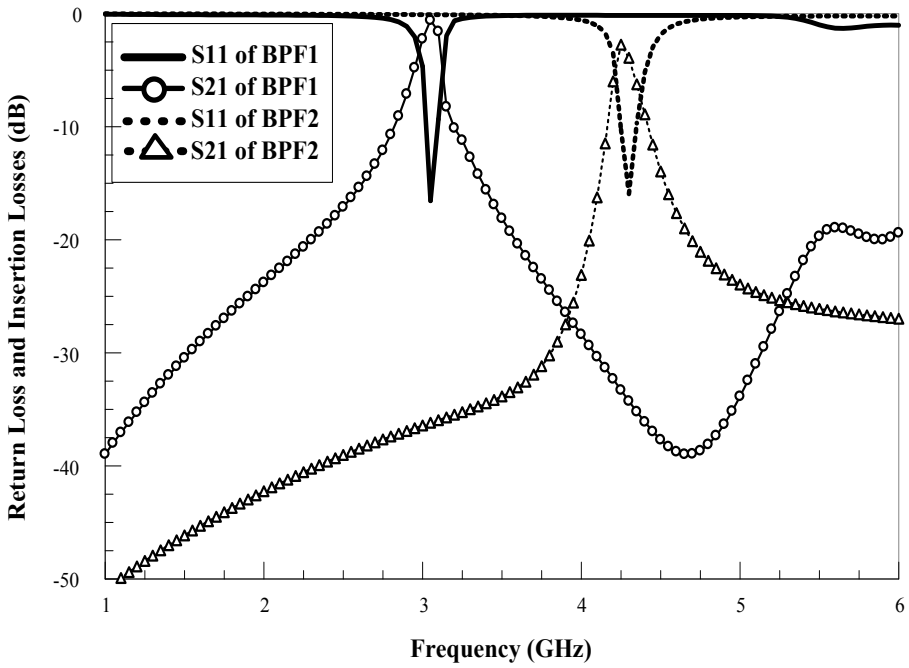

Fig. 15. Simulated results of two separated filters

The proposed diplexer is designed by combining two bandpass filters after having each bandpass filter design. Figure 16 shows configuration of the proposed diplexer. The input port of the 4.2 GHz bandpass filter is connected to the port 3 of the 3.1 GHz bandpass filter. The total dimensions of the diplexer is 32.6 mm X 16.4 mm, which is 0.47 λg X 0.23 λg at 3.1 GHz. Comparing with the single CSRR bandpass filter in previous chapter, the diplexer is considered very compact. Figure 17 shows simulated and measured results of the proposed diplexer. Measured and simulated results agree with each other well. The measured insertion losses of the diplexer are 1.8 dB and 2.3 dB at 3.1 GHz and 4.2 GHz, respectively. The measured return losses of the diplexer are 16.4 dB and 15.9 dB at 3.1 GHz and 4.2 GHz, respectively. Figure 18 shows pictures of the fabriated diplexer.

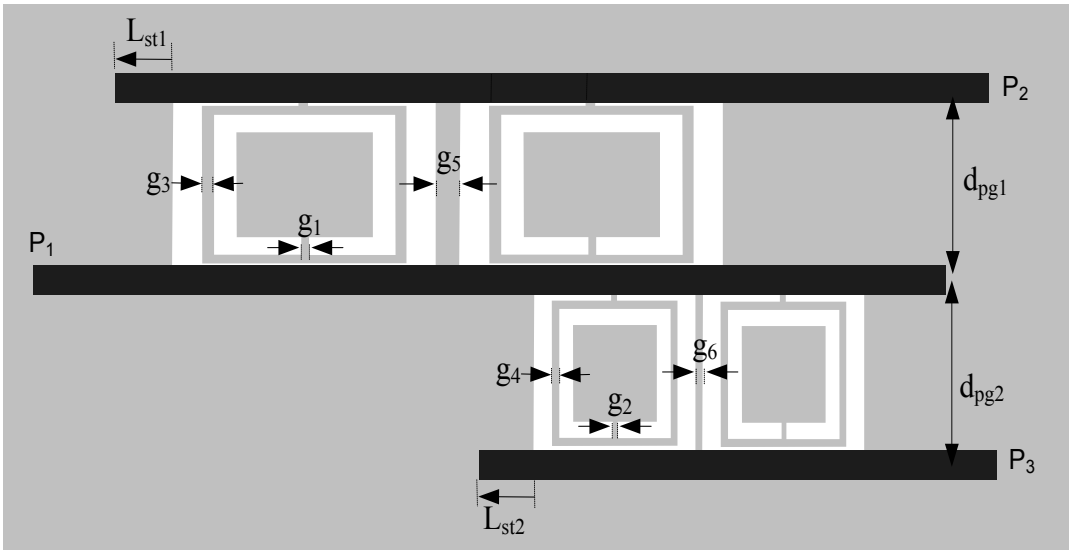

Fig. 16. Structure of the proposed diplexer (Lst_1 = 0.49 mm, g_1 = 0.36 mm, g_2 = 0.18 mm, g_3 = 0.46 mm, g_4 = 0.46 mm, Lst_2 = 0.98 mm, dpg_1 = 7.5mm, dpg_2 = 9.1 mm)

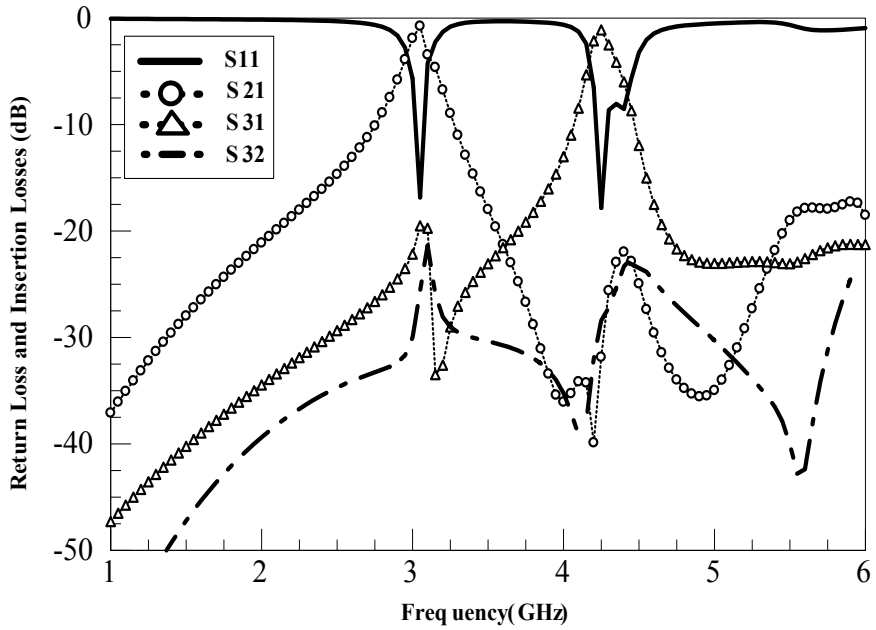

(a)

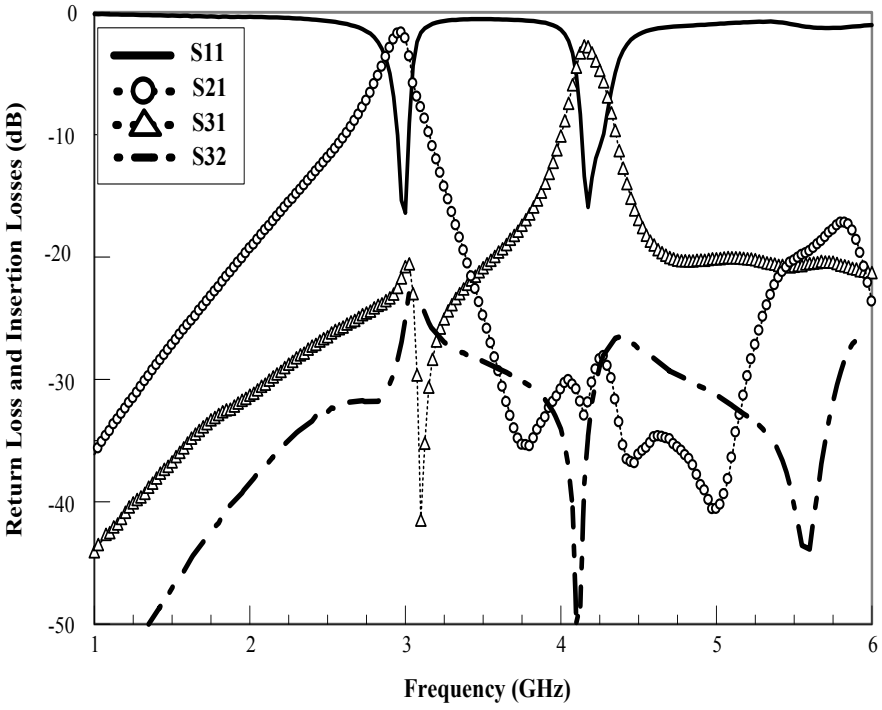

(b)

Fig. 17. (a) Simulated and (b) measured results of the proposed diplxer

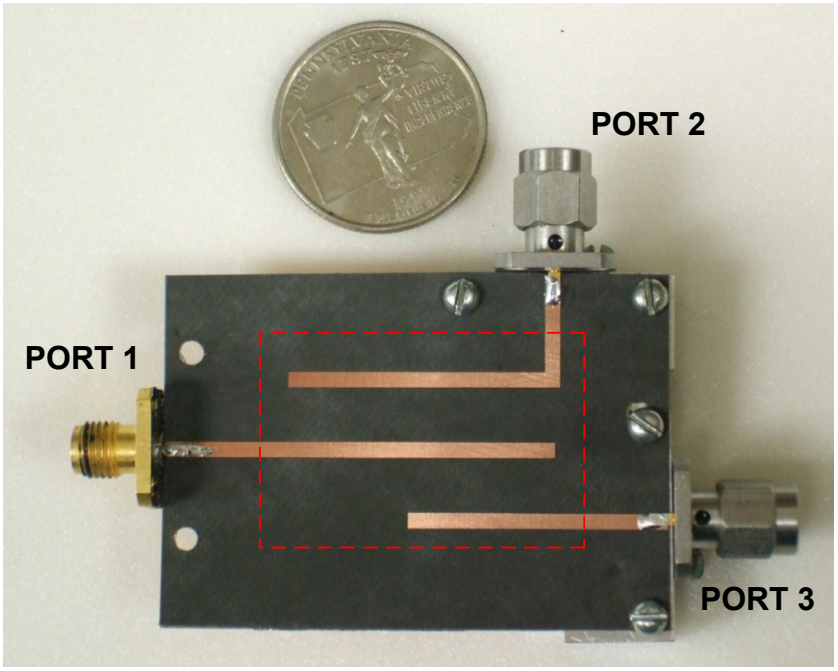

(a)

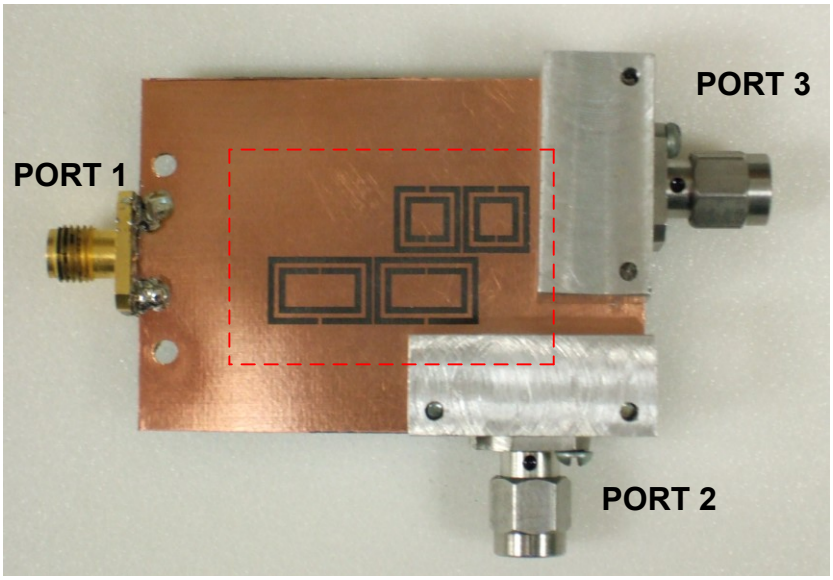

(b)

Fig. 18. Pictures of the proposed diplexer: (a) front view and (b) backside view

5. Summary

A parallel coupled line bandpass filter based on complementary split ring resonators has been introduced in this chapter. The parallel coupled transmission lines provide bigger value of coupling capacitance, resulting in better bandpass characteristics with two CSRRs only. The measured insertion loss of 1.4 dB with a compact size of 0.32 λg X 0.14 λg has been achieved at 3.6 GHz.

Two microstrip CSRR bandpass filters are designed and they are connected to design a compact microstrip diplexer. The diplexer takes an input signal from port 1 and transfers the signal of 3.1 GHz to port 2 and the signal of 4.2 GHz to port 3. The smulated and measured results match well with each other. The measured insertion losses of the compact diplexer are 1.8 dB for port 2 and 2.3 dB for port 3.

CHAPTER IV

DUAL BAND COMPLEMENTARY SPLIT RING ANTENNA FED BY COPLANAR WAVEGUIDE

1. Introduction

In the last several years, with the increasing demands of wireless technologies for simultaneously components minimization and multi-function performance, compact multi-band antennas are among most important components in modern wireless communication systems [57]-[59]. Multiple resonant modes can be excited by a tuning feed line at asymmetric locations of a slot ring [57] and by a tuning stub extended from the feed line [58]. However, the multiband designs are not compact and need special matching networks. In [59], by using narrow slotted meander lines, a compact dual-band is achieved. However, the compact antenna has a complicated structure and shows low gain at the lower resonant frequency.

Recently, complementary split ring resonator (CSRR) has caused much attention in microwave applications since Falcone introduced it in 2004 [49]. Due to its planar configuration and small size characteristics at resonant frequency, several antenna designs using CSRRs have been reported for antenna size reduction or other performance improvement [60]-[62]. In [60], CSRRs are in the ground plane of a microstrip patch antenna for the size miniaturization. A CSRR is etched on a UWB monopole patch and a microstrip patch antenna for dual band notched characteristics

[61] and for achieving circular polarization or dual-frequency linear polarization performances [62], respectively. In most antenna applications using CSRRs, however, the metamaterial components are combined to the conventional antennas to improve the antenna performance. Any antenna using a CSRR as the only radiator has not been reported.

In this chapter, a novel dual frequency CSRR antenna is developed. The CSRR antenna is excited by a CPW feed which has several merits, such as simple configuration, low radiation loss, and easy integration of solid-state components. Furthermore, no special matching network is required to obtain good impedance matching for the desired two resonant frequencies; therefore the proposed CSRR antenna configuration is simpler than the conventional dual band slot antennas. The effects of several design parameters of the rectangular shaped CSRR antenna are also presented and discussed.

2. CSRR Antenna Design

The proposed antenna simply consists of two squares of the slotted split rings based on CPW configuration. As shown in Figure 19, the outer and inner rectangular slot rings have side lengths L_1 and L_2, and have widths W_1 and W_2, respectively. Each slot ring has a split gap size of G_1 and G_2. The coupling distance between the inner and the outer split ring is d_r. For feeding, the width and spacing of CPW feed-line are given by W_f and S_f, respectively. The proposed CPW fed antenna is printed on a RT/Duroid 5870 substrate with a thickness h of 0.381mm and a relative dielectric constant ε_r of 2.33. No ground plane is printed on the other side of the dielectric substrate.

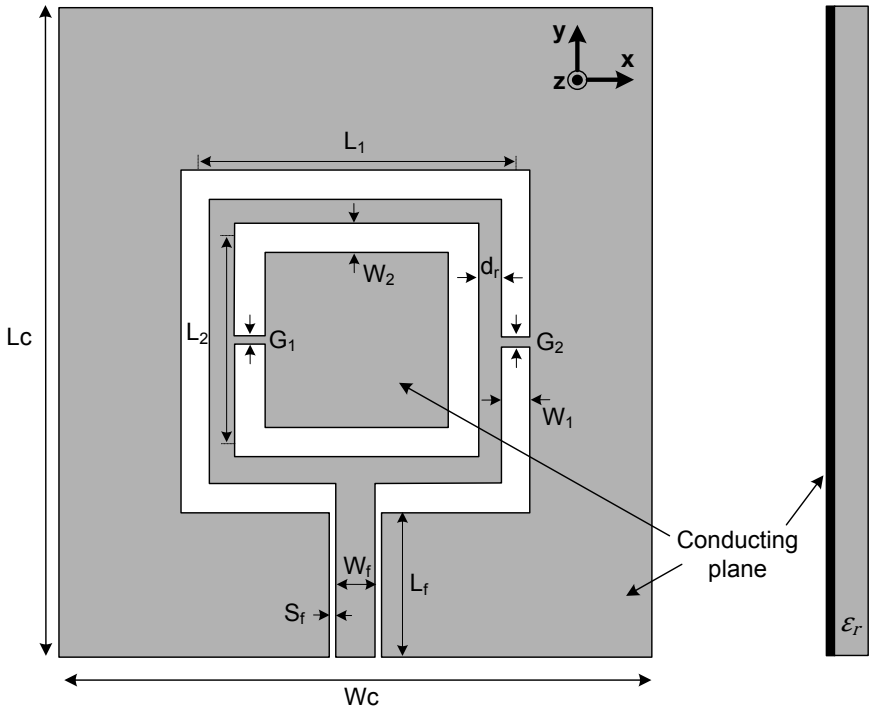

Fig. 19. Configuration of the proposed dual-frequency CSRR antenna

For compact dual-frequency CSRR antenna fed by CPW, several design parameters such as CSRR size, slot width, and coupling distance between two slot rings are investigated by calculated and measured results. For the calculated results, HFSS design software, a commercial 3D FEM based simulator, is used.

3. Measured Results

Figure 20 shows the measured return losses for four different prototypes of the proposed antenna (*Antenna A-D*). *Antenna C* has the same configuration with *Antenna A* except that the inner slot ring is removed. *Antenna D* is the case of *Antenna A* with no

split. The performances of the four prototypes with the measured results are summarized in Table 2 for comparison. It is obviously seen from the results that both two resonant frequencies decrease with increasing circumferences of the inner and outer split slot rings (*Antenna A, B*). Contrary to the conventional dual slot antennas, the outer slot ring of the CSRRs controls the higher operating frequency and the lower operating frequency is obtained by coupling between two split slot rings instead of inner slot ring size, which makes the CSRR antenna compact (*Antenna A, C*). It is also seen that the slot ring antenna without splits needs a special matching network (*Antenna D*). However, the proposed antenna shows good impedance matching at two resonant frequencies without any special matching network (*Antenna A*). The frequency ratio of the proposed antenna decreases from 1.3 to 1.1 when the circumferences of the two slot rings increase from Antenna A to B. Moreover, the lower resonant frequency generated by two CSRRs corresponds to the mean circumference of two CSRRs, which is approximately 0.65 λ_{gs}. Comparing with the conventional slot antennas resonating with about one slot guided wavelength (λ_{gs}) [63], the proposed CSRR antenna shows 35% size reduction.

The effect of different CSRR widths based on the prototype *Antenna A* is investigated in Figure 21. Both resonant frequencies (f_L, f_h) increase with increasing the width. It is also found that the lower resonant frequency (f_L) becomes dominant as the slot width increase, which might be due to more coupling between two wider CSRRs.

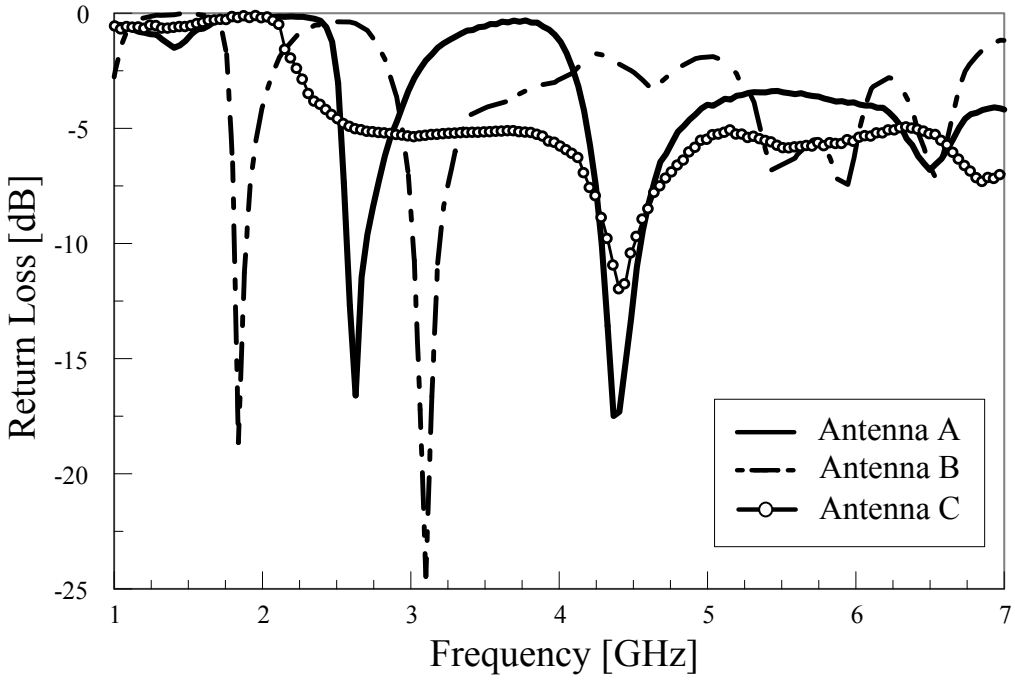

Fig. 20. Measured results of the different CSRR sizes

TABLE 2. Measured results of the four prototype antennas

	Antenna A	*Antenna B*	*Antenna C*	*Antenna D*
L_1 (mm, λ_{gs})	19.6	27.6	19.6	19.6
L_2 (mm, λ_{gs})	19.6	27.6	NA	19.6
W_1, W_2 (mm)	0.8, 0.8	0.8, 0.8	0.8, NA	0.8, 0.8
G_1, G_2 (mm)	0.2, 0.2	0.2, 0.2	0.2 , NA	0, 0
d_r (mm)	0.5	0.5	NA	0.5
f_L, BW(GHz, %)	2.62, 5.4	1.85, 4.9	NA	NA
f_H, BW(GHz, %)	4.4, 6.8	3.1, 6.5	4.42, 2.1	4.6, 0.8
f_H/f_L	1.68	1.67	NA	0, 0

In Figure 22 (a), the measured results of various distances (d_r) between two CSRRs are presented, which are also based on *Antenna A* model. The stronger resonances happen at lower resonant frequencies as the distance dr decreases since the capacitive coupling between two slotted split rings increases with narrow distances. Figure 22 (b) shows the simulated return losses of various distances d_r. The biggest distance (d_r = *4.4 mm*) shows similar return loss with *Antenna D*, which means that no coupling happens on CSRRs.

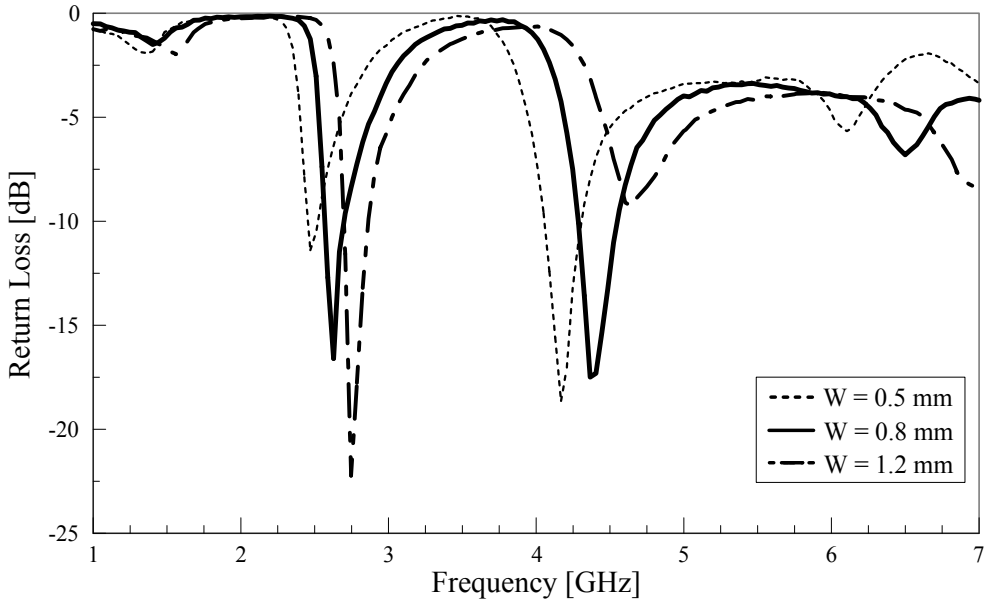

Fig. 21. Measured results of different CSRR widths

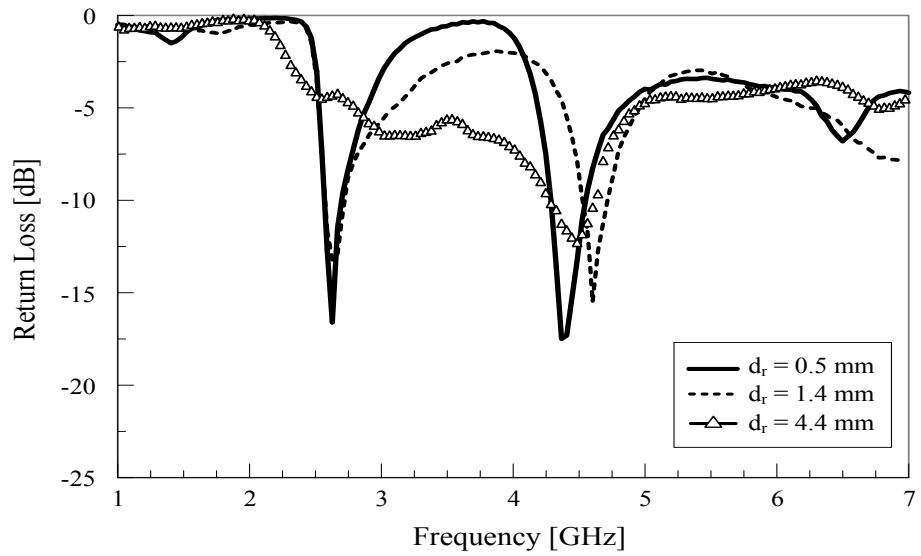

(a)

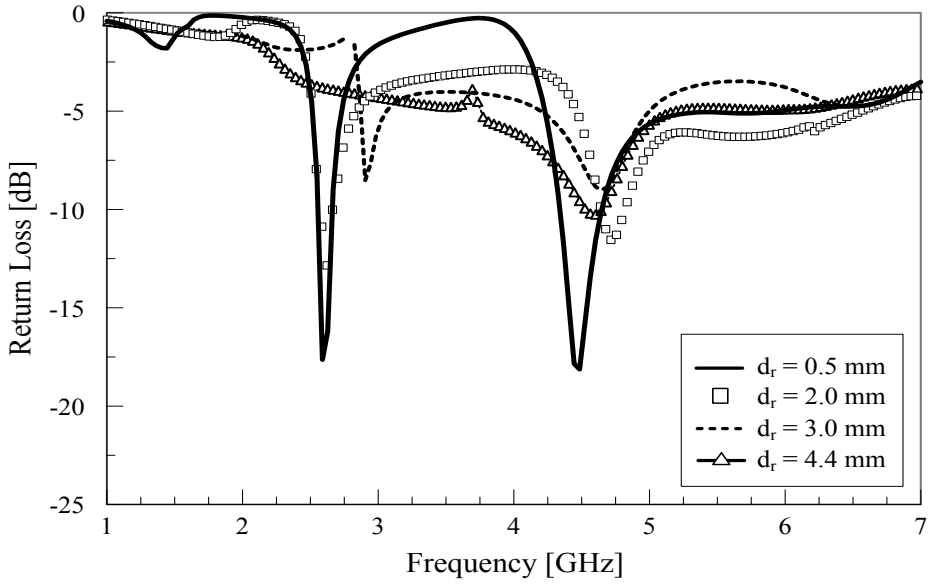

(b)

Fig. 22. (a) Measured and (b) simulated results of different distances of d_r

The normalized radiation patterns at the lower and higher operating frequencies for Antenna A are presented in Figure 23. Measured and simulated results are matched well with each other. The radiation patterns at 4.4 GHz in elevation plane are normal loop antenna pattern as expected as shown in Figure 23(a). The main beam of 2.6 GHz in elevation plane is tilted a little to the direction of -20^{o}. Possible reason could be that currents around CSRRs are not symmetric since two slits on the CSRRs are not located on symmetric positions. In azimuth plane shown in Figure 23 (b), the radiation patterns at two operating frequencies are similar with each other. The unsymmetrical patterns are due to slits on the CSRRs which leads unsymmetrical current flows on the patch. The antenna gains were also measured, and the results are presented in Figure 24. From the results, it is seen that the peak antenna gain at lower operating frequency is about 4.7 dBi. Also, the peak antenna gain at higher operating frequencies is about 2 dBi. The higher gain at the lower band is considered as the CSRR effects. The fabricated CSRR antenna is shown in Figure 25.

4. Summary

A compact dual-frequency antenna using complementary sprit ring resonators is presented and studied. The CSRR antenna is fed by coplanar waveguide. The dimensions of the rectangular CSRRs are tuned to achieve dual band frequency properties. The higher resonant frequency is dominantly determined by the outer slot

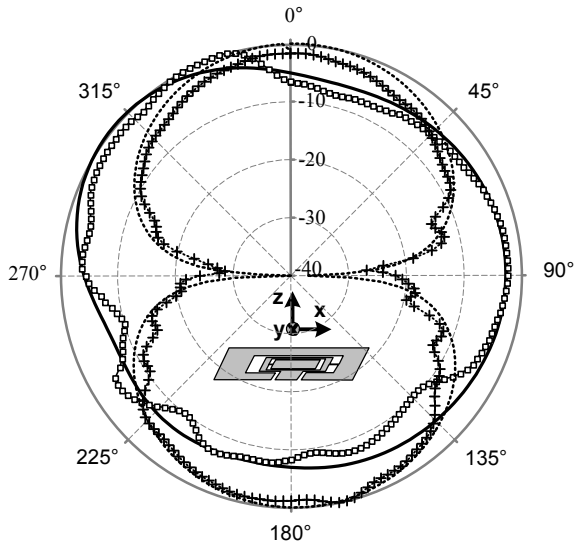

(a)

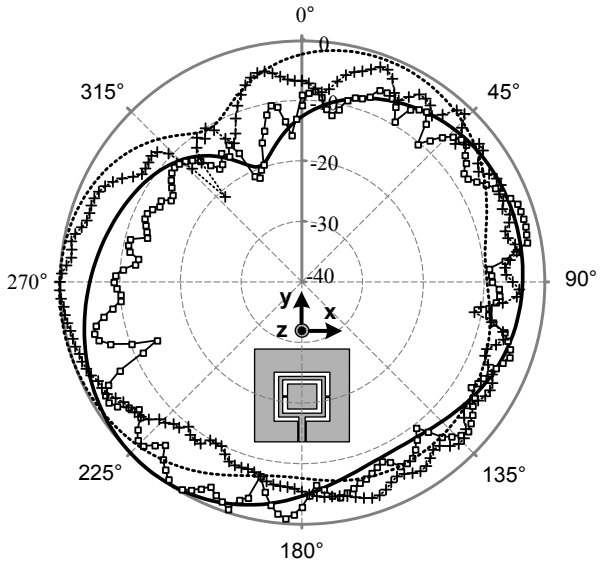

(b)

Fig. 23. Measured and simulated radiation patterns of *antenna A* in (a) elevation and (b) azimuth plane (—— : simulated result at 2.6 GHz, —□— : measured result at 2.6 GHz, - - - - : simulated result at 2.6 GHz, and -+- : measured result at 4.4 GHz)

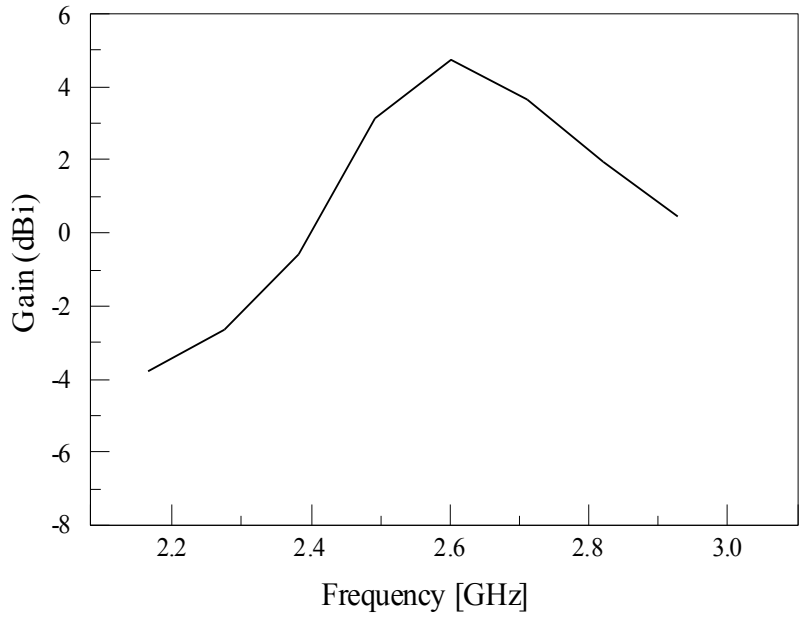

(a)

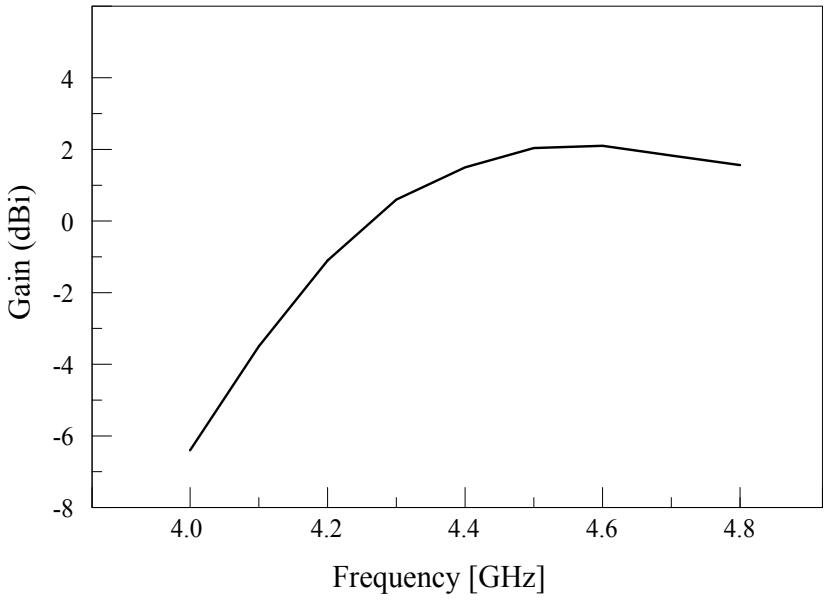

(b)

Fig. 24. Measured gains of the proposed antenna at (a) 2.6 GHz and (b) 4.5 GHz

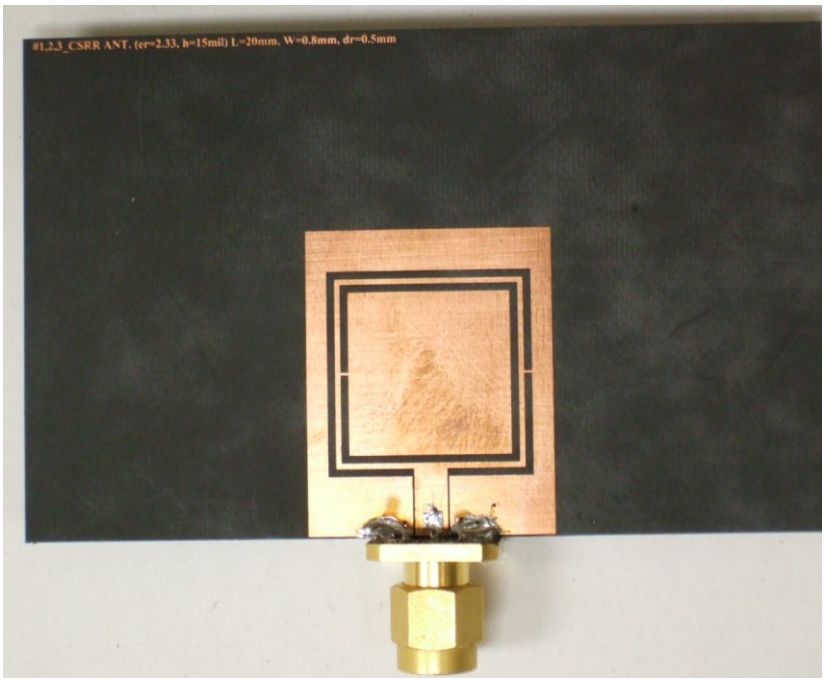

Fig. 25. The fabricated CSRR antenna

ring while the lower resonant frequency is generated by the coupling between two slots rings, which are CSRRs. The proposed antenna achieves about 35% size reduction effect at the low resonant frequency. The proposed inspired metamaterial antenna has measured gains of 4.7 dBi and 2 dBi at 2.6 GHz and 4.5 GHz, respectively.

CHAPTER V

HIGH GAIN RECTIFYING ANTENNA

1. Introduction

Space solar power transmission (SPT) and microwave wireless power transmission (WPT) have been attracted not only for an alternative solution to world energy problems in the future, but also for morden commercialized uses such as radio freqeuncy identification charger, or battery or power line free devices. The recteifying antenna called rectenna is one of the most key components in the SPT and WPT system. Among many technical developments in WPT history, the rectenna technologies have been dominantly improved for the system performance and efficiency improvement [18],[64], and[65].

Traditionally, dipoles or dipole-like antennas are used in rectenna design [66]. the coplanar stripline (CPS) is normally used to feed the antenna in a rectenna system due to easy fabrication and high characteristic impedance [28],[67],and[68]. In recent years, several different type of rectenna with differnet performances have been reported. A harmonic-rejecting circular sector rectenna for avoiding filter sections in rectenna circuits was reported [69]. A circularly polarized dual band rectenna was developed for portable wireless device applications [70]. Another circular polarized rectenna with two slot patch antennas was built for dual band performances: one resonant band is for data

communication and the other is for wireless power transmission [71]. To prevent the output voltage variations due to improper mainbeam alignment, a non-uniform rectenna array was proposed [72]. Another soultion to have constant output power is to use a retrodirective array [73]-[75]. The automatic beam steering features have been widely used in many wireless communication systems [76]-[78]. Retrodirective rectennas also have been developed using bow-tie antenna and microstrip ring elements [79]-[80].

To provide high DC output power, the rectenna system needs to receive a large amount of incoming RF power. To achieve this, high gain antenna element or a large antenna array for high gain performance are necessary. In this chapter, the WPT system and the rectenna operation theory are reviewed, and then a efficient high gain rectenna with pentagon rings is presented.

2. Wireless Power Transmission System

The main difference between the WPT system and communication systems is transferred power efficiency. Normally, the communication systems receive signals from all directions when the transmitters diffuses the signalsn while the WPT systems focus on a point reciever or pointed recievers for efficient wireless power transfer. So, even though the received signals have enough power for communications, the efficency of the communication system is very low comparing with the WPT system. Therefore, efficency is critical factor in the design of the WPT system.

A WPT system consists of three main functional blocks as shown in Figure 26. The first block is DC-to-RF transmitter. The original DC energy is converted to RF energy and the converted RF are radiated in the first block. The original DC source is

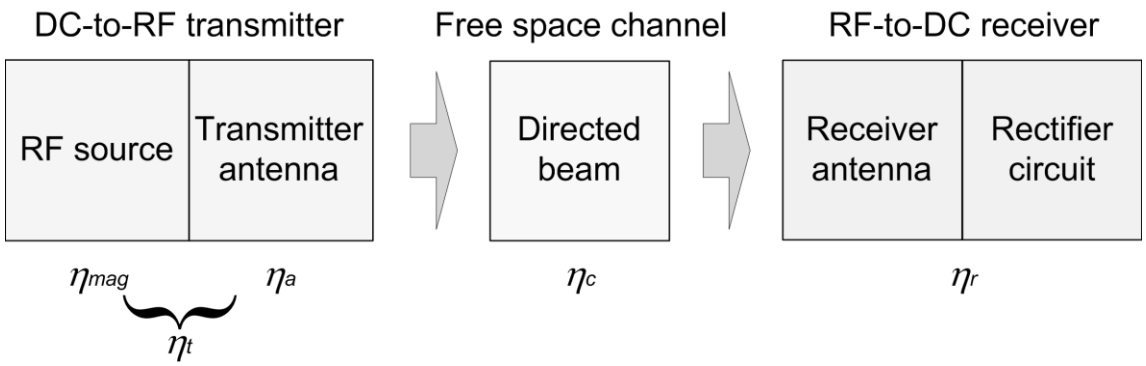

Fig. 26. Wireless power transmission system schematic

collected by either photovoltaic cells or solar thermal turbines. The DC to microwave convertor is either microwave tube (magnetron) system or simiconductor systems. The antenna element or array antennas are used to radiate the RF energy. The efficiency (η_t) of the first block, the electric to microwave conversion efficiency, is equal to the product of magnetron efficiency (η_{mag}) and the array antenna efficiency (η_a). The magnetron efficiency is used to express how efficient the RF source works. The antenna efficiency at the transmitter represents the ability of the antenna to radiate the distributed RF power fed from the RF source and radiated into free-space.

The second block is free space channel. The radiated RF power from the array antenna is transferred across free space within a specific focused beam towards a receiver. The efficiency (η_c) is this block, collection efficiency, is the ratio of the received power over the transmitted power. For maximum collection efficiency, an optimum power density distribution must be selected for the transmitting antenna aperture. A non-uniformly illuminated aperture increases the collection efficiency and it has been seen that the optimal taper is of Gaussian type. The collection efficiency is

proportional to a design parameter τ, which is expressed as Goubau's relation [81]-[82]

$$\tau = \frac{\sqrt{A_r A_t}}{\lambda_0 D} \tag{32}$$

where A_r and A_t are the aperture areas of the receiver and the transmitter antennas. As can be seen from this equation, Goubau's relation can be used to determine the size of the apertures involved. The collection efficiency is given by

$$\eta_c = (1 - e^{-\tau^2}) \times 100\% \tag{33}$$

which is proportional to the power density and the incremental area of the antenna. For example, as A_t becomes larger, the incident power density also increases leading to a higher collection efficiency as seen through τ. This translates into a tradeoff between the efficiency and the size.

The last block is RF-to-DC receiver, where rectennas rectify the incomming RF signals to generate DC output power. Figure 27 shows the basic components of the rectenna element. An antenna element attaches to a RF filter (bandpass or lowpass filter) that transforms the impedance of the antenna to the rectifier impedance and prevents the high-order harmonics resulted from the rectifier reradiating. The rectifying diode is the

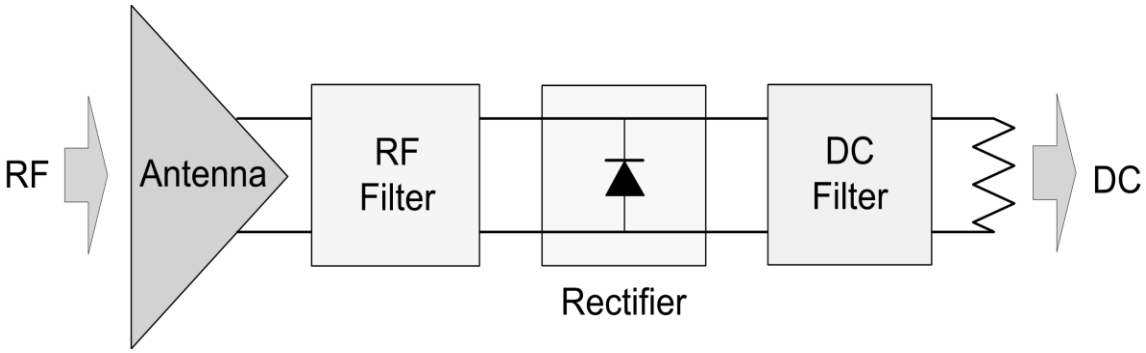

Fig. 27. Rectenna block diagram

core element of the rectifier. The output DC filter of a large capacitor effectively shorts the RF energy and passes the DC power. A load resistor is placed at the output terminal to measure the DC output voltage. The efficiency of this block is called rectenna efficiency.

The overall efficiency (η_{all}) of a WPT system is the ratio of the DC output power at the receiver end over the DC (or RF) input power at the transmitter end, which is given by

$$\eta_{all} = \eta_t \cdot \eta_c \cdot \eta_r \tag{34}$$

which means that the end-to-end efficiency includes all the sub-efficiencies starting from the DC supply feeding the RF source in the transmitter to the DC power interface at the receiver output.

3. Rectenna Operation Theory

It is important to understand how a half-wave rectifier with shunt capacitor works, which is the fundamental theory used for a microwave rectenna design. The basic theory of the half-wave rectifier can be found in [83]. The rectenna operation theory has been studied in [67]-[68]. In this chapter, several important concepts are reviewed.

A. Rectifying Circuit Theory

The rectenna circuit consists of the half-wave rectifier circuit and the DC-pass capacitor where the capacitor is in shunt with the diode as shown in Figure 28 (a). The voltage across the load as a function of time is

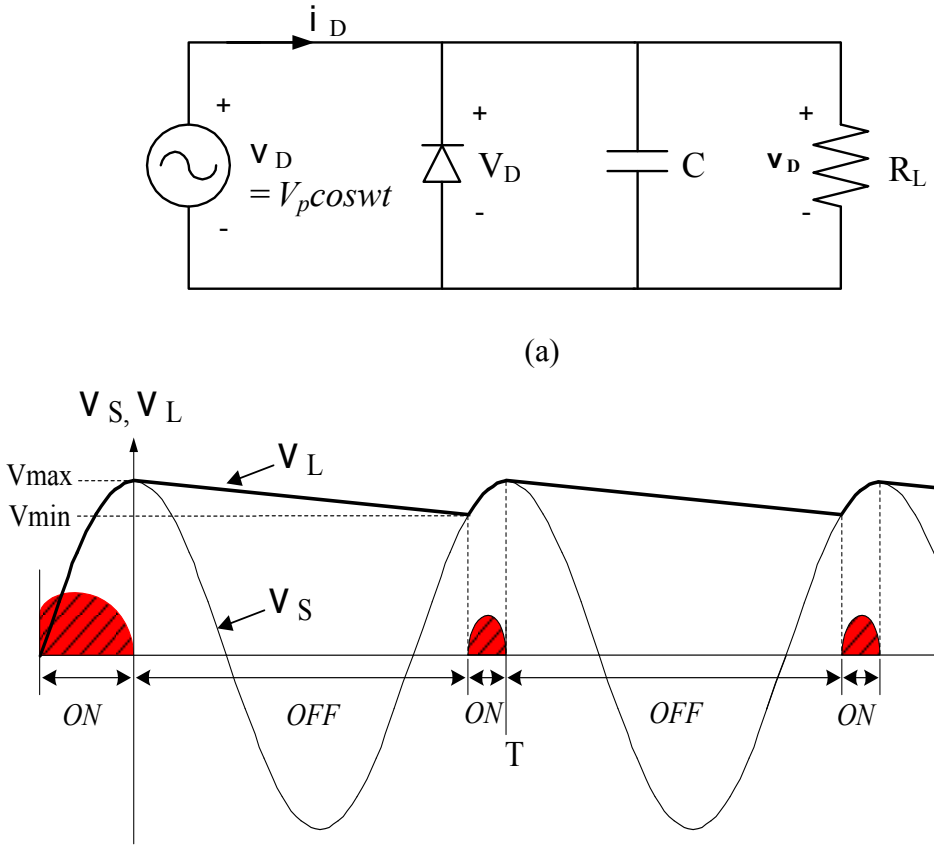

Fig. 28. (a) Half-wave rectifier with capacitor and (b) its waveforms

$$\upsilon_L(t) = 0 + (V_P - 0)e^{-\frac{t}{R_L C}} = V_P e^{-\frac{t}{R_L C}} \tag{35}$$

where $R_L C$ is the time constant, V_P is the initial value and 0 is the final voltage if the capacitor completely discharges. The time t is measured from the peak where the voltage is equal to V_P. When the rectenna's operating frequency has such a short period in comparison with the $R_L C$ time constant, the exponential decrease in the voltage can be approximated by a straight line as shown in Figure 28 (b).

By series expanding, equation (35) becomes

$$\upsilon_L(t) = V_P e^{-\frac{t}{R_L C}} = V_P \left(1 - \frac{t}{R_L C} + \frac{\left(\frac{t}{R_L C} \right)^2}{2} - \ldots \right) \tag{36}$$

Since the decreasing voltage has been approximated as a straight line, the linear terms of the equation (36) are kept and the minimum voltage at $t = T$ becomes

$$V_{\min} \approx V_P \left(1 - \frac{T}{R_L C} \right) = V_P \left(1 - \frac{1}{f R_L C} \right) \tag{37}$$

Once the diode voltage drops to V_{min}, the diode turns on and the voltage again approaches $V_{max} = V_P$. The peak-to-peak ripple of the voltage waveform is

$$V_r = V_{\max} - V_{\min} = \frac{V_P}{f R_L C} \tag{38}$$

and the average DC diode voltage present across the load resistor is

$$V_D = \frac{V_{\max} - V_{\min}}{2} = V_P \left(1 - \frac{1}{2 f R_L C} \right) \approx V_P \tag{39}$$

The period of the incoming 5.8 GHz energy is 172.4 ps. The capacitance of the DC-pass filter is approximately 2400 pF. This translates to $R_L C >> T$. Therefore, the ripple voltage V_r is very small, and the average diode DC voltage is $V_D \approx V_P$. This average DC diode voltage is also known as the self-bias voltage used in further analysis.

B. Diode Modeling

Figure 29 shows a RF voltage waveform operating across the diode and the diode junction voltage. This model assumes the harmonic impedances seen by the diode are either zero of infinite that avoids the power loss by the harmonics. The fundamental

voltage wave will not be corrupted by the higher order harmonic components. Then the rectenna conversion efficiency only depends on the diode electrical parameters and the circuit losses at DC and the fundamental frequency. The voltage waveform can be expressed as

$$V_I = -V_D + V_P \cos(\omega t) \tag{40}$$

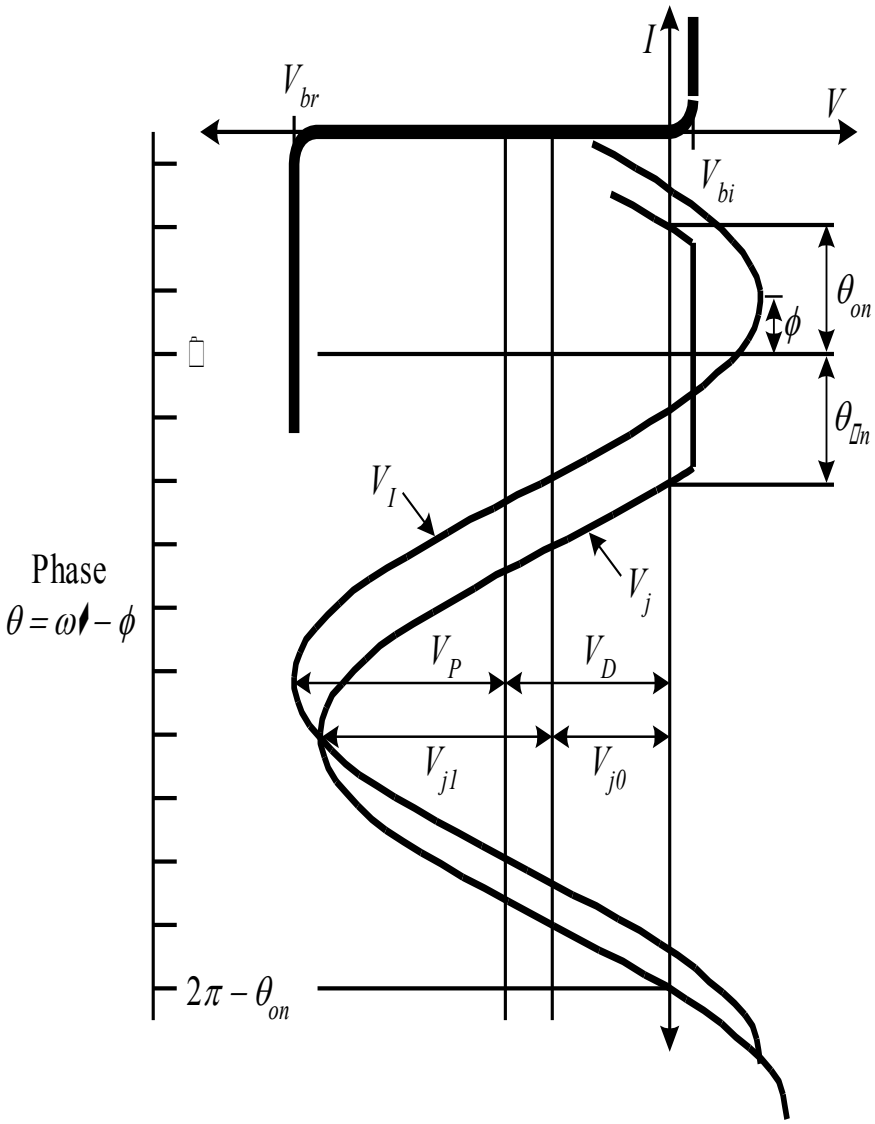

Fig. 29. Diode current-voltage characteristic curves with the incident fundamental and diode junction voltage waveforms

where V_D is the self-bias DC output voltage across the resistive load R_L, and V_P is the peak voltage amplitude of the incident RF power. The rectifying diode acts as a mixer that produces a self-bias voltage. As the incident power is increased, the rectified self-biasing will become more reversed biased. The diode junction voltage is

$$V_j = \begin{cases} -V_{j0} + V_{j1}\cos(\omega t - \phi), & V_j < V_{bi} \\ V_{bi}, & V_j \geq V_{bi} \end{cases} \tag{41}$$

where V_{j0} and V_{j1} are the DC and fundamental frequency components of the diode junction voltage, respectively; V_{bi} is the diode's built-in turn-on voltage; θ_{on} is the forward bias turn-on angle. When the junction voltage exceeds V_{bi}, the diode will operate in forward conduction. Figure 29 also shows that the diode's junction waveform slightly lags the incident power by a phase difference ϕ.

The equivalent circuit used to determine the diode's efficiency is shown in Figure 30. The diode parasitic reactive elements are excluded from the circuit. The diode model consists of a series resistance R_S, a nonlinear junction resistance R_j, a non-linear junction capacitance C_j, and a load resistor R_L. The junction rsistance R_j is assumed to be zero for forward bias and infinite for reverse bias. Applying Kirchoff's voltage law in the equivalent circuit, we have

$$V_D + I_D R_S + V_{j,dc} = 0 \tag{42}$$

With $V_D = I_D R_L$, the DC output voltage is given by

$$V_D = -V_{j,dc}\frac{R_L}{R_S + R_L} \tag{43}$$

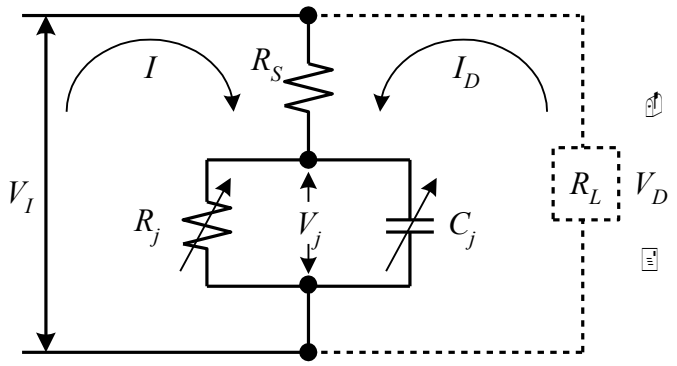

Fig. 30. Equivalent circuit model of the half-wave rectifier

The DC output voltage is determined from the rectified voltage across the diode junction V_j. In each cycle, the average value of V_j is

$$V_{j,dc} = \frac{1}{2\pi}\int_{-\theta_{on}}^{\theta_{on}} V_{bi}\ \mathrm{d}\theta + \frac{1}{2\pi}\int_{\theta_{on}}^{2\pi-\theta_{on}} \left(-V_{j0} + V_{j1}\cos\theta\right)\mathrm{d}\theta \tag{44}$$

The first term and the second term represent the forward-biased and the reverse-biased cases. Integrate the equation gives

$$V_{j,dc} = \frac{\theta_{on}}{\pi}V_{bi} - V_{j0}\left(1-\frac{\theta_{on}}{\pi}\right) - \frac{V_{j1}}{\pi}\sin\theta_{on} \tag{45}$$

When the diode switches from off to on, $V_j = V_{bi}$. Then we have

$$-V_{j0} + V_{j1}\cos\theta_{on} = V_{bi} \tag{46}$$

When the diode is off, R_j is infinite. Applying Kirchoff's voltage to the other loop gives

$$-V_I + IR_S + V_j = 0 \tag{47}$$

with

$$I = \frac{dC_j V_j}{dt} \tag{48}$$

These two equations can be rewritten by

$$\frac{d\left(C_j V_j\right)}{dt} = \frac{(V_I - V_j)}{R_S} \tag{49}$$

where C_j can be expressed as a harmonic function of V_D

$$C_j = C_0 + C_1 \cos\left(\omega t - \phi\right) + C_2 \cos\left(2\omega t - 2\phi\right) + \ldots \tag{50}$$

Using above two equations yields

$$\omega R_S \left(C_1 V_{j0} - C_0 V_{j1}\right)\sin\theta = V_{j0} - V_D + \left(V_P \cos\phi - V_{j1}\right)\cos\theta - V_P \sin\phi \sin\theta \tag{51}$$

where $\theta = \omega t - \phi$. Because this equation also holds for the off period, each sinusoidal term can be collected as

$$V_{j0} = V_D \tag{52}$$

$$V_{j1} = V_P \cos\phi \tag{53}$$

$$V_P \sin\phi = \omega R_S \left(C_1 V_{j0} - C_0 V_{j1}\right) \tag{54}$$

Substituting (52) to (45) and inserting (43) into (45) obtains

$$\frac{R_S}{R_L} = \frac{V_{j1}}{V_D}\frac{1}{\pi}\sin\theta_{on} - \frac{\theta_{on}}{\pi}\left(1 + \frac{V_{bi}}{V_D}\right) \tag{55}$$

It can be shown that the phase difference ϕ can be approximated to be zero, which results in $V_P = V_{j1}$. Inserting this and (52) into (46) and (55) to obtain

$$\tan\theta_{on} - \theta_{on} = \frac{\pi R_S}{R_L\left(1+\frac{V_{bi}}{V_D}\right)} \tag{56}$$

This transcendental expression allows obtaining θ_{on} iteratively, which is dependent on the diode input power that determines both V_{bi} and V_D.

The diode efficiency can be expressed as

$$\eta_D = \frac{P_{dc}}{P_L + P_{dc}} \tag{57}$$

where P_L is the power dissipated by the diode and P_{dc} is the DC output power across R_L. They are given by

$$P_L = L_{on,R_S} + L_{off,R_S} + L_{on,diode} \tag{58}$$

$$P_{dc} = \frac{V_o^{\,2}}{R_L} \tag{59}$$

The three terms of the diode loss P_L can be expressed by

$$L_{on,R_S} = \frac{1}{2\pi}\int_{-\theta_{on}}^{\theta_{on}} \frac{\left(V_I - V_{bi}\right)^2}{R_S}\,d\theta \tag{60}$$

$$L_{off,R_S} = \frac{1}{2\pi}\int_{\theta_{on}}^{2\pi-\theta_{on}} \frac{\left(V_I - V_d\right)^2}{R_S}\,d\theta \tag{61}$$

$$L_{on,diode} = \frac{1}{2\pi}\int_{-\theta_{on}}^{\theta_{on}} \frac{\left(V_I - V_{bi}\right)V_{bi}}{R_S}\,d\theta \tag{62}$$

Since it is assumed the junction resistance is infinite during the off cycle, the loss

through the diode junction has been neglected. These power losses are the time-average products of the current flowing through an element and the voltage across the element. The total power dissipated on the series resistance can be solve by integrating

$$L_{R_S} = \frac{1}{2\pi R_S}\left[\int_{-\theta_{on}}^{\theta_{on}} \left(-V_D - V_{bi} + V_P \cos\theta\right)^2 d\theta + \left(\omega R_S C_j V_P\right)^2 \int_{\theta_{on}}^{2\pi-\theta_{on}} \sin^2\theta d\theta\right] \quad (63)$$

Using the RF current instead of voltage in the second integral, (27) can be rewritten as

$$L_{off,R_S} = \frac{1}{2\pi}\int_{\theta_{on}}^{2\pi-\theta_{on}} \frac{\left(V_I - V_j\right)^2}{R_S} d\theta = \frac{1}{2\pi}\int_{\theta_{on}}^{2\pi-\theta_{on}} \frac{\left(IR_S\right)^2}{R_S} d\theta \quad (64)$$

where I is the RF current flowing through the diode in reverse bias. It is assumed that no current flows through R_j in reverse bias and all of the current flowing through R_S flows through C_j. Then (48) can be expressed as

$$I = C_j \frac{dV_j}{dt} \quad (65)$$

The voltage drop across R_S is so small in the off cycle that the phase difference ϕ is set zero. Apply this in (55) to obtain $V_{j1} = V_P$. Then

$$I = C_j \frac{d}{dt}\left[-V_{j0} + V_P \cos\left(\omega t\right)\right] = -\omega C_j V_P \sin\theta \quad (66)$$

The power dissipated by the diode junction is rewritten as

$$L_{diode} = \frac{1}{2\pi R_S}\int_{-\theta_{on}}^{\theta_{on}} V_{bi}\left(-V_D - V_{bi} + V_P \cos\theta\right) d\theta \quad (67)$$

where V_P is determined, while the diode is off, by

$$V_P = \frac{V_D + V_{bi}}{\cos\theta_{on}} \tag{68}$$

Use the results from (63) and (68) and insert them into (57), we have

$$\eta_D = \frac{1}{1+A+B+C} \tag{69}$$

where

$$A = \frac{R_L}{\pi R_S}\left(1+\frac{V_{bi}}{V_D}\right)^2\left[\theta_{on}\left(1+\frac{1}{2\cos^2\theta_{on}}\right)-\frac{3}{2}\tan\theta_{on}\right] \tag{70}$$

$$B = \frac{R_S R_L C_j{}^2\omega^2}{2\pi}\left(1+\frac{V_{bi}}{V_D}\right)\left(\frac{\pi-\theta_{on}}{\cos^2\theta_{on}}+\tan\theta_{on}\right) \tag{71}$$

$$C = \frac{R_L}{\pi R_S}\left(1+\frac{V_{bi}}{V_D}\right)\frac{V_{bi}}{V_D}\left(\tan\theta_{on}-\theta_{on}\right) \tag{72}$$

with $\omega = 2\pi f$. The diode junction capacitance is given by

$$C_j = C_{j0}\sqrt{\frac{V_{bi}}{V_{bi}+|V_D|}} \tag{73}$$

where C_{jo} is the zero bias junction capacitance of the diode

The input impedance of the diode can be decided from the current I flowing through R_S in one cycle, that is

$$I = I_0 + I_{1r}\cos(\omega t) + I_{1i}\sin(\omega t) \tag{74}$$

where I_0 is the DC component; I_{1r} and I_{1i} are the real and imaginary parts of the fundamental frequency component, respectively. These current components are

$$I_0 = \frac{1}{2\pi R_S}\left\{\int_{-\theta_{on}}^{\theta_{on}}\left(V_I - V_{bi}\right)d\theta + \int_{\theta_{on}}^{2\pi-\theta_{on}}\left(V_I - V_j\right)d\theta\right\} \tag{75}$$

$$I_{1r} = \frac{1}{\pi R_S}\left\{\int_{-\theta_{on}}^{\theta_{on}}\left(V_I - V_{bi}\right)\cos\left(\theta+\phi\right)d\theta + \int_{\theta_{on}}^{2\pi-\theta_{on}}\left(V_I - V_j\right)\cos\left(\theta+\phi\right)d\theta\right\} \tag{76}$$

$$I_{1i} = -\frac{1}{\pi R_S}\left\{\int_{-\theta_{on}}^{\theta_{on}}\left(V_I - V_{bi}\right)\sin\left(\theta+\phi\right)d\theta + \int_{\theta_{on}}^{2\pi-\theta_{on}}\left(V_I - V_j\right)\sin\left(\theta+\phi\right)d\theta\right\} \tag{77}$$

The diode input impedance at the fundamental frequency is

$$Z_D = \frac{V_P}{I_{1r} - jI_{1i}} \tag{78}$$

Assume that there is no current flow through C_j during forward bias and that all current flow through during reverse bias, the diode current in one cycle can be found by integrating

$$I_{1r} - jI_{1i} = \frac{1}{\pi R_S}\int_{-\theta_{on}}^{\theta_{on}}\left(-V_D - V_{bi} + V_P\cos\theta\right)\cos\theta d\theta + j\frac{\omega C_j V_P}{\pi}\int_{\theta_{on}}^{2\pi-\theta_{on}}\sin^2\theta d\theta \tag{79}$$

The second integral is solved similar to that in (63). Then the diode input impedance can be written as

$$Z_D = \frac{\pi R_S}{\cos\theta_{on}\left(\dfrac{\theta_{on}}{\cos\theta_{on}} - \sin\theta_{on}\right) + j\omega R_S C_j\left(\dfrac{\pi-\theta_{on}}{\cos\theta_{on}} + \sin\theta_{on}\right)} \tag{80}$$

If the reactance of the diode impedance is tuned out by using the impedance matching, the diode input impedance can be rewritten as

$$R_D = \frac{\pi R_S}{\cos\theta_{on}\left(\frac{\theta_{on}}{\cos\theta_{on}} - \sin\theta_{on}\right)} \tag{81}$$

The input resistance is a dynamic variable dependent on the input power, as the same as the diode efficiency.

4. High Gain Rectenna Element Design

The proposed high gain rectenna is shown in Figure 31. The rectenna is comprised of a pair of pentagonal loop antennas, a detector diode in shunt, a capacitor in shunt, and a load at the end of the rectenna system. The coplanar stripline fed pentagonal loop antennas are designed to achieve high gain and high radiation effciency. The main role of the antenna is to receive the RF signals effectively from free space. Unlike normal rectenna designs, this rectenna element does not include a band-reject filter which is for suppression of harmonics generated from a rectifying diode. The RF signals passed the diode are converted into DC power. The capacitor next loacted to the diode works as DC pass filter. It does not only block RF singals traveling toward the resistive load, but also tune out the reactance of the diode. Finally, the proper value of the resistive load is selected to maximize output DC power. To optimize the rectenna performance, proper placement of the diode and the DC pass filter should be carefully considered.

A. Pentagonal Loop Antenna

The proposed antenna has a linearly polarized high gain characteristic which is

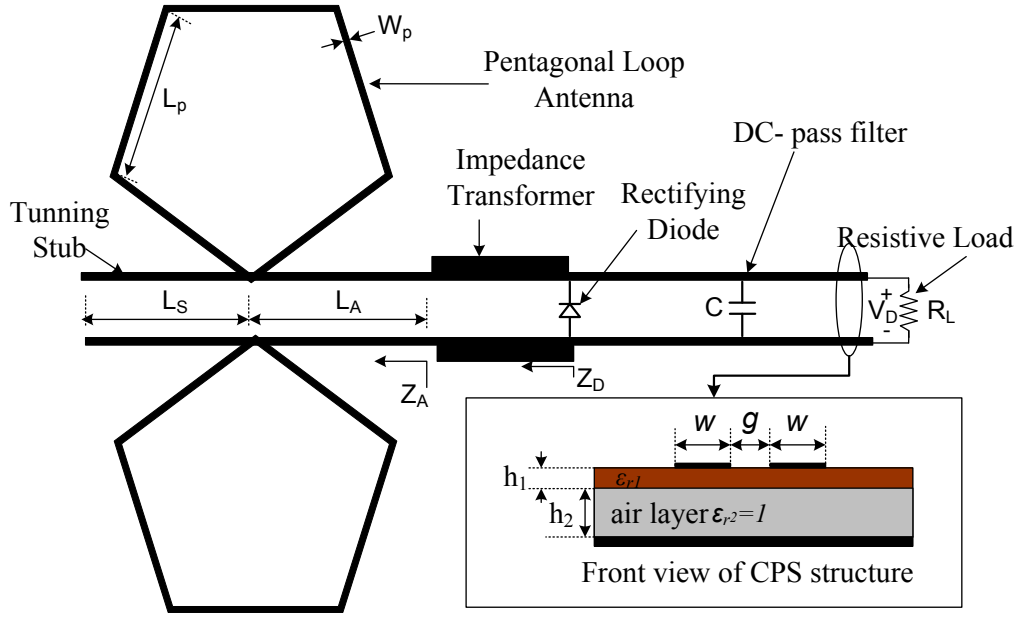

Fig. 31. Configuration of the proposed high gain rectenna with pentagonal loops.

demanded for rectenna systems. The two pentagonal loops with the same size are based on coplanar stripline feed. The antennas printed on the substrate RT/Duroid 5880 with 20 mils (h_1) thickness. A reflecting conducing plane is placed 11.2 mm (h_2) behind the substrate to achieve a higher gain by directing the beam broadside in one direction, and reduce the back-radiation. The antenna parameters are optimized for 5.8 GHz frequency operation by using the IE3D simulator, an electromagnetic full-wave analysis software based on Method of Moment. The optimized dimensions are L_p = 12.7 mm, L_S = 14.76 mm, L_A = 11. 41 mm, W_p = 0.85 mm. With these values, the antenna achieves high gain of 10.2 dBi at 5.8 GHz. Figure 32 and 33 show the simulated input impedance and gain of the antenna. The antenna input impedance Z_A is equal to 112 Ω. For antenna design in a rectenna system, the input impedance of the antenna should be matched with input

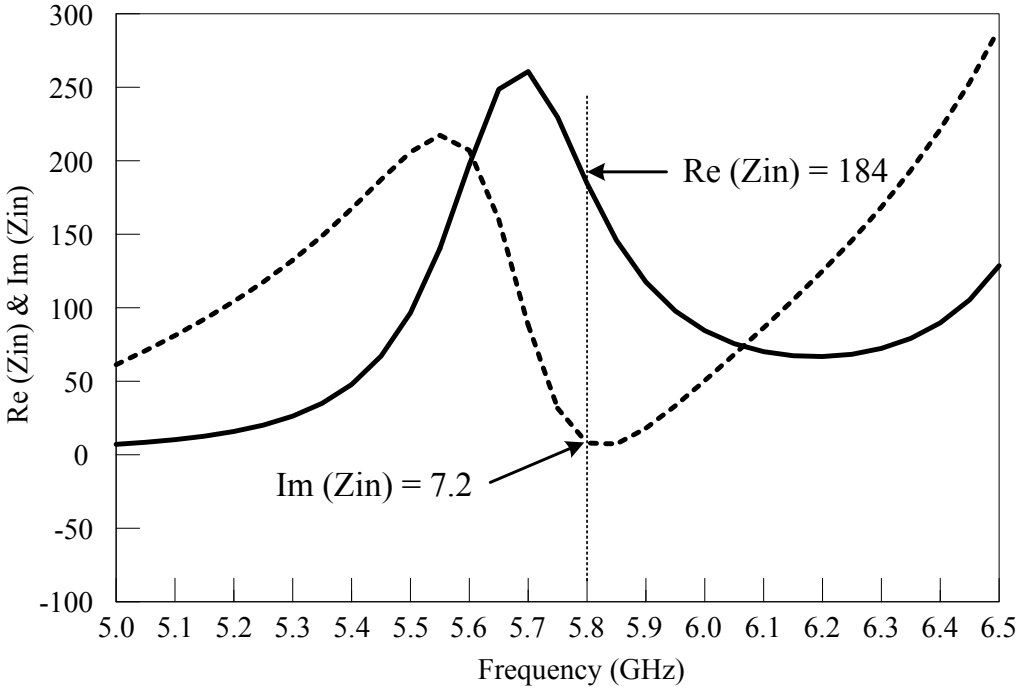

Fig. 32. Simulated input impedance of the antenna

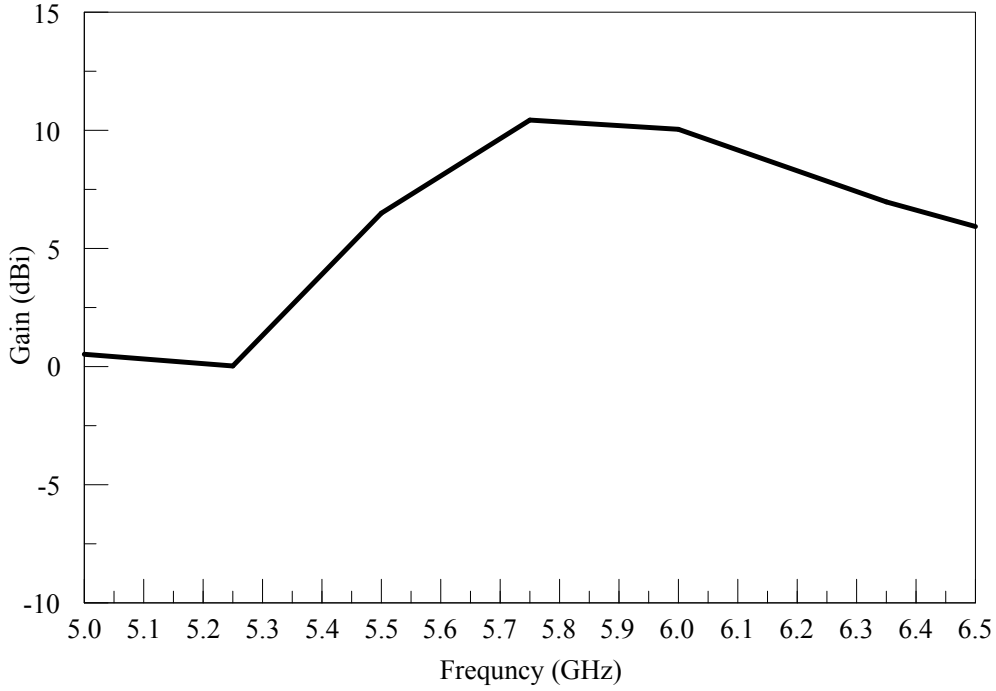

Fig. 33. Simulated antenna gain

impedance of rectifying diode circuit.

B. Coplanar Stripline Structure

The proposed rectenna is based on coplanar stripline structures as shown in Figure 31. The dimensions of the CPS in both antenna feed and the rectifying circuit are w = 0.9 mm and g = 0.4 mm. The characterisitic impedance of the CPS is 184 Ω. Another CPS structure is located between the antenna and the diode as an impedance tranformer. To obtain optimizing maching network, the CPS is designed with w = 1.92 mm and g = 0.4 mm for 143.5 Ω of characteristic impedance. Therefore, the input impedance Z_D before the diode becomes 184 Ω. In rectenna design, the characterisitic impedance of the based transmission line is chosen to match the impedances of the antenna with the diode to reduce the signal reflections between these components.

C. Detector Diode and DC Pass Filter

The diodes used in this dissertation are the GaAs flip chip Schottky barrier diodes (Model MA4E1317) from M/A COM. It has a series resistance R_S = 4 Ω, zero-bias junction capacitance C_{j0} = 0.02 pF, forward-bias turn-on voltage V_{bi} = 0.7 V, and breakdown voltage V_B = 7 V. The junction capacitance (C_j) of the diode, described in (69), significantly affects the diode efficiency, which is a function of the diode output voltage. Equation (69) is rewritten here for convenience

$$C_j = C_{j0}\sqrt{\frac{V_{bi}}{V_{bi}+|V_D|}} \tag{82}$$

V_D is the output self-bias voltage of the diode. Higher V_D results in a smaller junction

capacitance, which also gives better conversion efficiency. The maximum efficiency occurs when C_j approaches to zero. Furthermore, the diode should operate as close to its voltage limit as possible to minimize its reactance. This reduces the reflection of the RF power at the diode terminal and hence increases the rectenna efficiency.

A broadband DC-blocking chip capacitor by Dielectric Laboratories (Model C08BLBB1X5UX) is chosen as the DC pass filter. The DC pass filter not only tunes out the reactance of the diode but also blocks the unwanted RF signals from reaching the load resistance. The detector diode and the DC-blocking capacitor are mounted across the coplanar stripline by using silver epoxy.

D. Rectenna Measurements and Conversion Efficieny

The free space measurement of the rectenna has been studied in [28]. The equipment setup is shown in Figure 34. The RF-to-DC conversion efficiency of the rectenna (η) can be defined as

$$\eta = \frac{P_{DC}}{P_r} \tag{83}$$

P_{DC} is the DC output power. Friis transmission equation is used to calculate the power propagating to the CP antenna (P_r). A NARDA standard horn antenna with a 15 dB gain (G_t) is used to transmit the RF power (P_t), and the rectenna gain (G_r) is set equal to 10.1 dB. By changing the distance between the horn antenna and the rectenna, the efficiencies for different power densities are determined. The power density (P_d) is given by

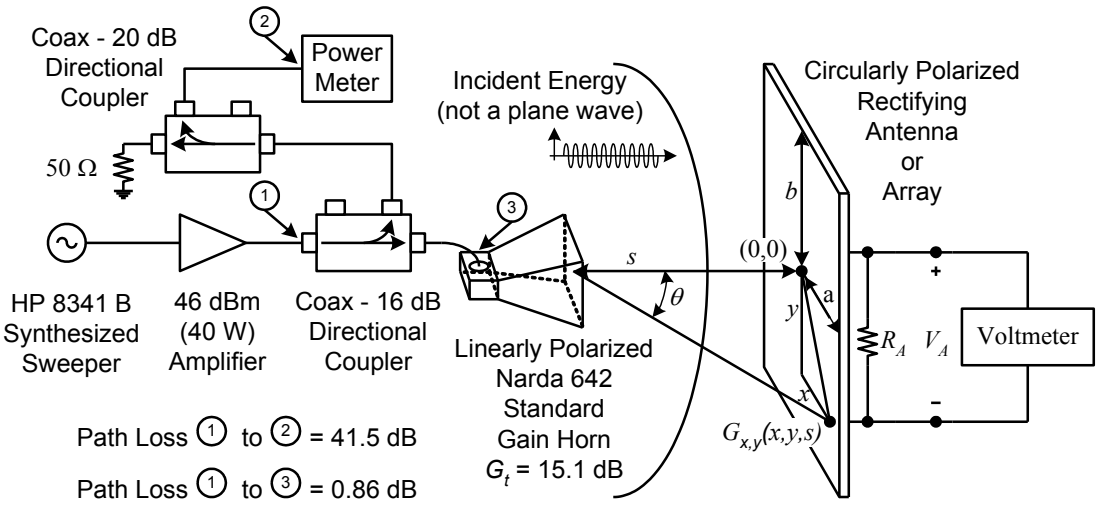

Fig. 34. Free space measurement setup of the rectenna

$$P_d = \frac{P_t G_t}{4\pi D^2} \tag{84}$$

where D is the distance between the horn antenna and the center of the rectenna.

The conversion efficiency curves of the single high gain rectenna at 5.8 GHz are shown in Figure 35. The best RF-to-DC conversion efficiency of the rectenna is 75 % when the load and the DC output voltage are 100 Ω and 5.4 V, respectivley. It is obviously seen that the efficiency gradually decreases as the load resistance increases.

5. Summary

In this chpater, WPT system and rectenna operation theory have been reviewed. A pentagonal loop antenna has been developed at 5.8 GHz. The pentagonal loop provides linear polarization and achieves high gain of 10.1 dBi. The CPS feed line is

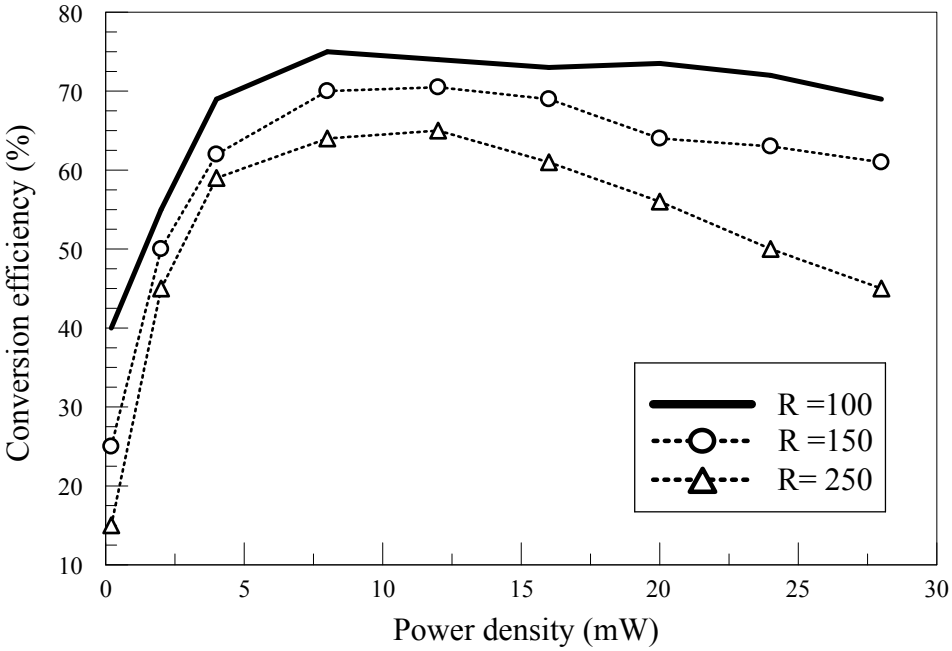

Fig. 35. Measured rectenna efficiency at 5.8 GHz

designed with characteristic impedance of 184 Ω. A impedance transfermer is used to match the antenna input impedance to the diode input impedance. The proposed rectenna achieves a maximum conversion efficiency of 75% with the resistivie load of 100 Ω.

CHAPTER VI

RECTIFYING ANTENNA ARRAY USING REFLECTARRAY

1. Introduction

In the past, several array types of rectennas have been studied with high gain property to achieve a long distance WPT, higher output DC power, and reduced receiving areas. However, in the array rectenna design, there might be several problems, such as: the relatively high loss of array feeding networks, difficulty in feeding network design, and antenna coupling between the nearest located radiators thus causing lower rectenna array performance. To overcome these downsides, a novel rectenna system using a reflectarray instead of array antenna elements is proposed in this chapter.

The reflectarray combines the advantages of both traditional reflector antennas (the most often used high gain antennas) and conventional phased array antennas, such as: being flat, having a low-profile, and being easier to manufacture. Moreover, the spatial feeding method eliminates the energy loss and design complexity of the conventional feed networks. The reflectarray features can be adapted to a rectenna for the WPT system. The reflectarray normally achieves high gain that a feed network is not necessary, nor is an antenna coupling. The proposed novel rectenna array suggests a new type of long distance WPT system.

2. Reflectarray Operation Theory

A. Basic Reflectarray Operation Theory

The basic operation theory of the reflectarray is reviewed from the reference [84]. Figure 36 shows the geometry of a microstrip reflectarray and the image of a parabolic reflector. A feed antenna is placed at the focal point to illuminate the reflectarray. When the wave from the feed antenna is incident on the reflectarray surface, the elements of the reflectarray will reradiate the incident energy into the space. However, as can be seen from Figure 36, the incident path lengths for the field propagating from the feed antenna to the elements are different. Therefore, the reradiated field will not be coherent.

The key to the reflectarray design is to adjust the reflection phases of the elements to compensate for the path length differences so that the reradiated fields from each element would be collimated towards one specific direction. The analysis is derived by comparing the configurations of a parabolic reflector and a flat microstrip reflectarray. Figure 37 shows the block diagram of a flat reflectarray with its virtual parabolic surface. An incident plane wave strikes the parabolic reflector's metal surface and bounces to a focal point a distance f above the center of the parabolic reflector. Each reflectarray elements are located at a position (x',y') from the center of the array (0,0). The distance between the focal point and any antenna element is denoted as r_{mn}. The angle θ' is the angle between the path connecting the focal point and the array center and the path connecting the focal point and the antenna element.

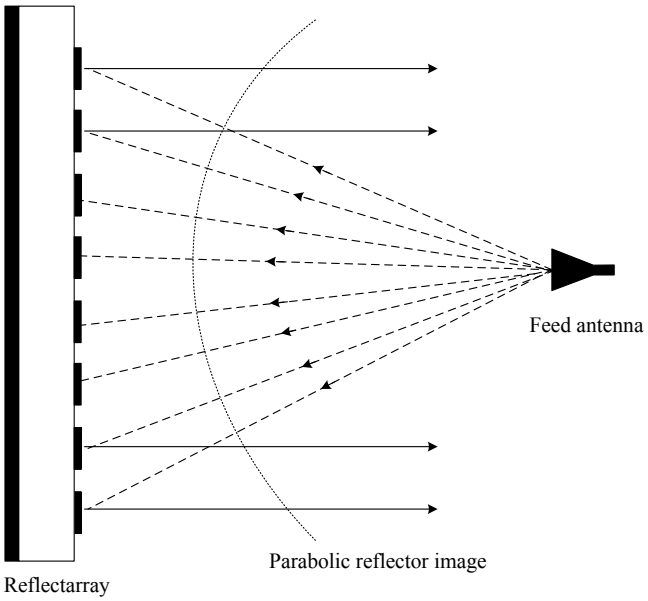

Fig. 36. Geometry of a microstrip reflectarray

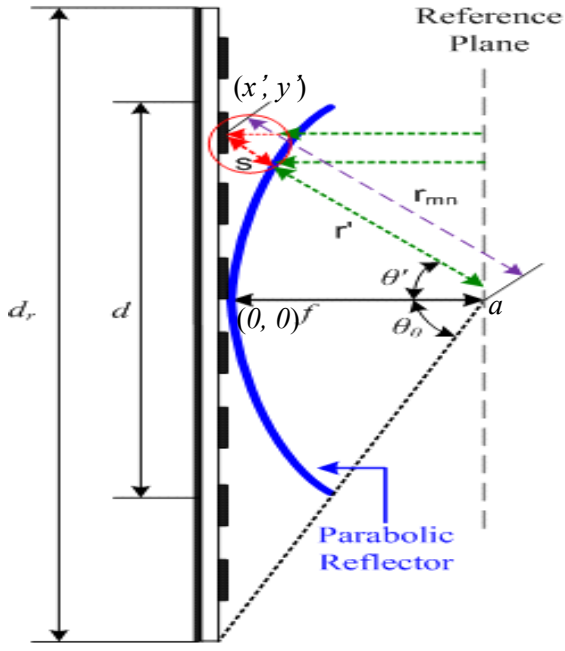

Fig. 37. Reflectarray block diagram

The dimension of the reflector (*d)* and the largest angle (θ_0) from the center of the parabolic reflector to its edge are related [86] as

$$\theta_0 = \tan^{-1}\left(\frac{\left|0.5\frac{f}{d}\right|}{\left(\frac{f}{d}\right)^2 - \frac{1}{16}} \right) \tag{85}$$

From equation (85), the diameter of the reflectarray can be determined by

$$d_r = 2f\tan(\theta_0) \tag{86}$$

The angle θ' can also expressed as

$$\theta' = \tan^{-1}\left(\frac{\sqrt{x'^2 + y'^2}}{f} \right) \tag{87}$$

The distance from the focal point to any point on the surface of the parabolicreflector is [85]

$$r' = \frac{2f}{1+\cos\theta'} \tag{88}$$

For any angle θ', the distance from the reference plane to the reflectarray to the focal point is ($s + s \cos \theta'$) longer than the corresponding ray trace from the reference plane to the parabolic dish to the focal point. This additional path length must be compensated in the design of the reflecting element array in order to provide the parabolic phase front across the surface of the array. The path length in radians is

$$\Delta\ell \quad \frac{2\pi f}{c} \quad s + s\cos\theta') \tag{89}$$

where f_0 is the resonant frequency of the array and c is the light speed. The distance s is equal to

$$s = \frac{f}{\cos\theta'} - r' \tag{90}$$

The antenna elements are designed properly to compensate for the additional path lengths Δl.

B. Aperture Efficiency of Reflectarray

In the design of a reflectarray system, the aperture efficiency is one of the most important factors to predict the reflectarray system performance. Similar to the normal parabolic reflector, the design of the reflectarray system usually begins with a specified gain. The gain of a reflectarray antenn can be obtained by the product of the aperture directivity and the aperture efficiency. The aperture directivity D_r is determined by the aperture area A as

$$D_r = \frac{4\pi A}{\lambda^2} \tag{91}$$

Then , the gain of the reflectarray antenna is defined as

$$G = \frac{4\pi A}{\lambda^2}\eta_a \tag{92}$$

If the aperture efficiency does not include the efficiency factors related with the feed loss, reflectarray element loss, polarization loss, and mismatch loss, the aperture loss is determined by two dominant efficiency terms in the reflectarray design: the spillover efficiency (η_s) and the illumination efficiency (η_i). So, the aperture efficiency can be defined as

$$\eta_a = \eta_s \eta_i \tag{93}$$

To calculate the efficiencies of the reflectarray, the radiation properties of the feed antenna should be modeled. Among various radiation models, $\cos^q$ pattern is used in this study due to its simplicity.

$$U_f = \cos^{2q}\theta (0 \le \theta \le \frac{\pi}{2}) \tag{94}$$

The parameter q determines the pattern shape and the directivity of the feed antenna. Figure 38 shows the directivity of the feed antenna versus the q value. The large q value, the higher directivity is. Once the feed antenna is designed with a specific directivity, the q value is obtained.To verify the $\cos^q$ pattern, Figure 39 shows the real antenn pattern with 10 dBi of directivity and $\cos^q$ pattern with 2 of q value. As seen from the result, two patterns are matched well with each other.

The term spillover is defined as the ratio of the power intercepted by the reflecting elements to the total power, which is usually considerd in transmit mode. Figure 40 shows the reflectarray configuration for spillover efficiency, which is the percentage of the radiated power from the feed that is intercepted by the reflecting aperture [86].

$$\eta_s = \frac{\int_\sigma \int \vec{P}(\vec{r})\vec{s}}{\int_{total} \int \vec{P}(\vec{r})\vec{s}} \tag{95}$$

where the denominator is the total power radiated by the feed, and the numerator is the portion σ of the power incident on the array apperture.

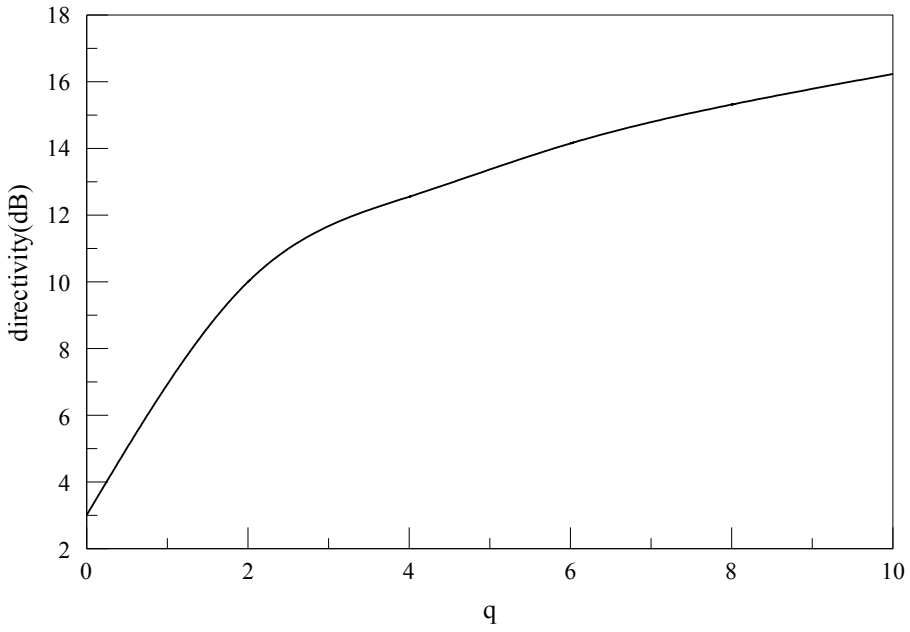

Fig. 38. Directivity vs. q factor of the feed

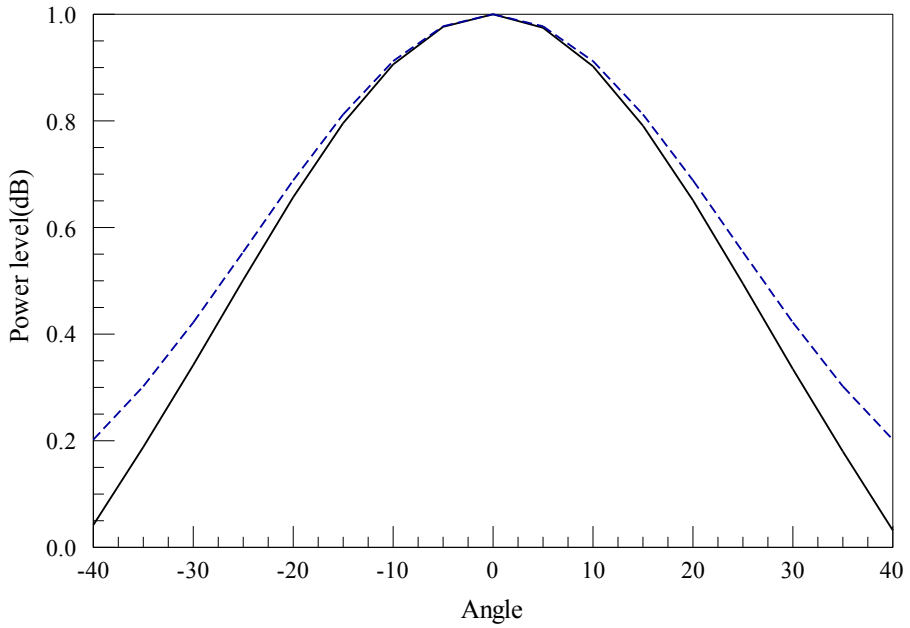

Fig. 39. The real antenna pattern vs. $\cos^q$ pattern

(——— : real antenna pattern, ····· : $\cos^q$ pattern)

The spillover efficency in equation (95) can be expressed in terms of the design parameters of the reflectarray system [86] as

$$\eta_s = \frac{2q+1}{2\pi}\int_0^{2\pi}\int_0^{D/2}\frac{H}{r^3}\left(\frac{r_0^{\,2}+r^2-s^2}{2r_0 r}\right)^{2q}\rho d\rho\varphi \tag{96}$$

Thus, η_s is a function of six design parmaters:

$$\eta_s = \eta_s(D,\theta_0,H,q,x_0,y_0) \tag{97}$$

From the result, the spillover efficiency is free from the reflectarray element pattern among all the configuration parameters.

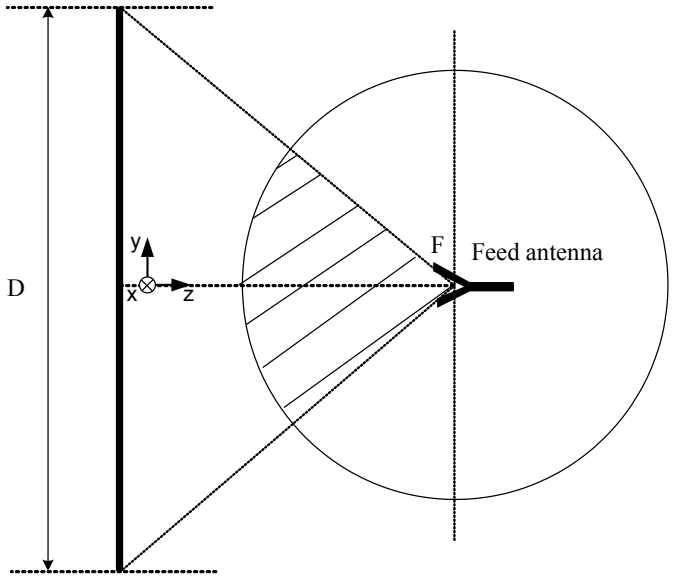

Fig. 40. Reflectarray configuration for spillover efficiency

The illumination efficiency is efficiency loss due to non-uniform amplitude and phase illumination of the aperture plane.

$$\eta_i = \frac{1}{A_a} \frac{\left| \iint_A I(x,y) dA \right|^2}{\iint_A |I(x,y)|^2 dA} \tag{98}$$

where *I(x,y)* is the amplitude distribution over the aperture. This can be also calculated [86] as

$$\eta_i = \frac{4}{\pi D^2} \frac{\left[\int_0^{2\pi} \int_0^{D/2} \frac{1}{r^1 + q_e} \left(\frac{r_0^2 + r^2 - s^2}{2 r_0 r} \right)^q \rho d\rho \varphi \right]^2}{\int_0^{2\pi} \int_0^{D/2} \frac{1}{r^1 + q_e} \left(\frac{r_0^2 + r^2 - s^2}{2 r_0 r} \right)^q \rho d\rho \varphi} \tag{99}$$

which means that η_i is a function of seven parameters:

$$\eta_i = \eta_i(D, \theta_0, F, q, x_0, y_0, q_e) \tag{100}$$

The aperture efficiency of the reflectarray can be calculated once the spillover efficency and illumination efficiency are determinded.

$$\eta_a = \eta_i \eta_s(D, \theta_0, F, q, x_0, y_0, q_e) \tag{101}$$

In the design of a reflectarray, it is desired to find the maximum aperture efficiency with the given design parameters. Especially, the feed location is an important parameter in practical design. The feed location is described by the offset angle θ_0 and the height *F*.

Figure 41 shows the aperture efficiency versus the ratio of the feed height *F* to reflectarray diameter *D*. In this study, the offset angle θ_0 is set at 25^o. As F/D grows, the maximum aperture efficiency appears at the higher q factor value. For example, if the

gain of the feed antenna is set 10 dBi, which means the q factor value is about 2, from the graph, the aperture efficiency of the reflectarray is expected as 60 % with F/D of 0.6. Figure 42 shows efficiencies versus q value with F/D of 0.6. It is seen from the results that as the value q increase, the spillover efficiency increases and the illumination efficiency decreases. The aperture efficiency reaches a maximum when q is equal to 0.66 in this study.

As a result, the aperture efficiency is affected by the following reflectarray parameters: the shape and dimensions of the aperture, the position of the feed, the direction of the feeding beam, the pattern of the feed, and the pattern of the reflectarray elements.

3. Reflectarray Component Design

In this chapter, a compact reflectarray element is desinged for a rectifying reflectarray system. The configuration of the proposed reflectarray is shown in Figure 43. This reflectarray elements are printed on the substrate Rogers RT/5880 with thickness of 0.508 mm. The air form layer (ε_r = 1.06) of 3.2 mm is inserted between the substrate and the ground plane. The unit cell element with its dimensions and the close-up picture of the reflectarray elements are shown in Figure 44. The proposed element is a combination of an inner circular patch and an outer ring with ring radius and width of R and W_r, respectively. In the element design, outer ring width W_r and gap width W_g is fixed as 1 mm and 0.5 mm, respectively. The important design parameter is radius of the outer ring R which is varied to obtain the element reflection phase variation curve.

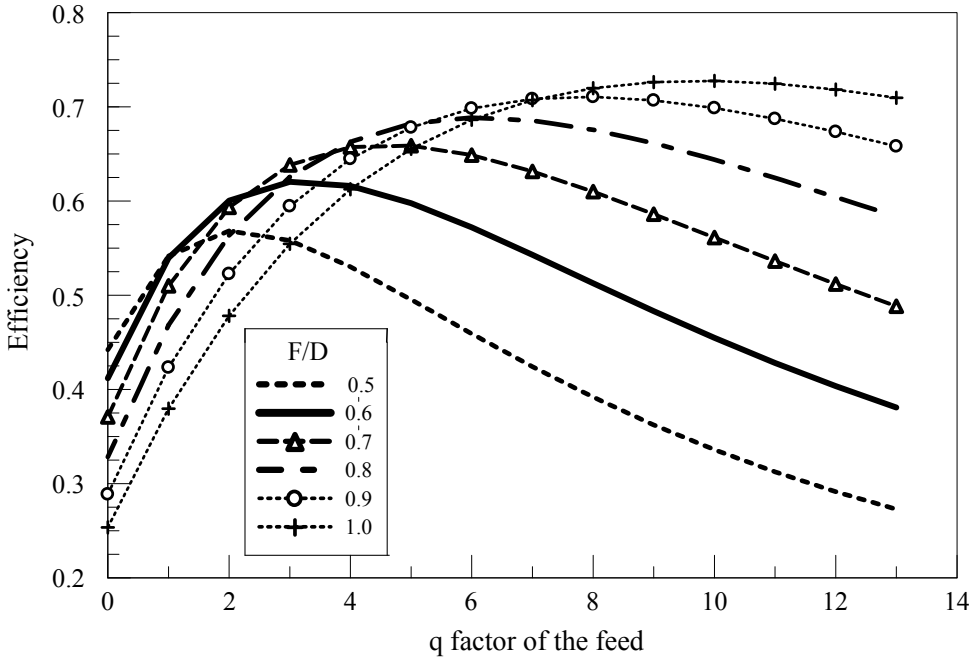

Fig. 41. Aperture efficiency vs. F/D

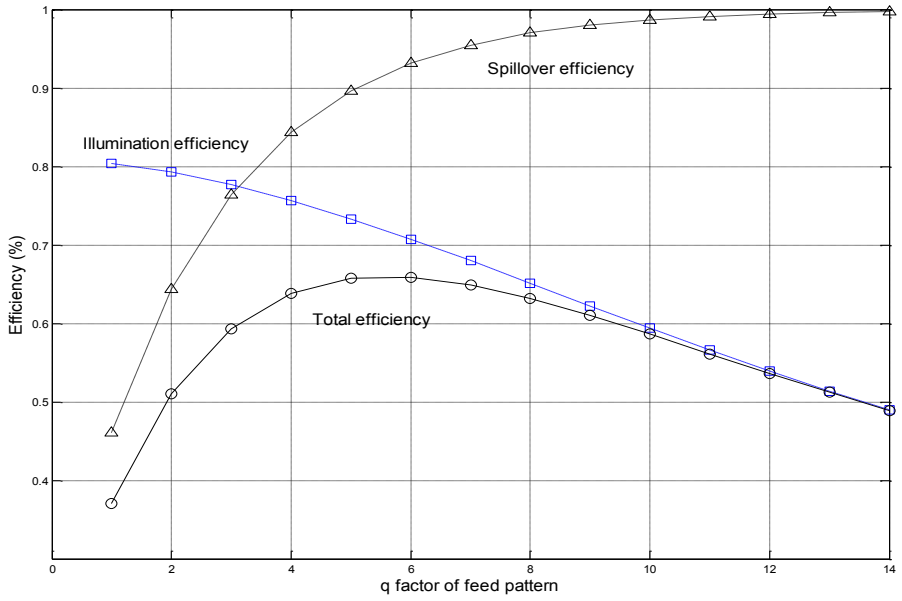

Fig. 42. Efficiency vs. F/D

The unit cell size is 18 mm X 18 mm, which is 0.35 λ_0 X 0.35 λ_0 at 5.8 GHz. The compact size unit cell allows more elements to be added in the limited area, which leads to have higher gain. Figure 45 shows the simulated reflection phases against the unit cell element by controlling the outer ring radius R at the operation frequency. Neither the ring nor the circular patch alone can provide a sufficient phase variation range for a practical reflectarray design. With the proposed ring-patch combination, it is found that the compact reflectarray element provides a sufficient phase range of 370^{o}.

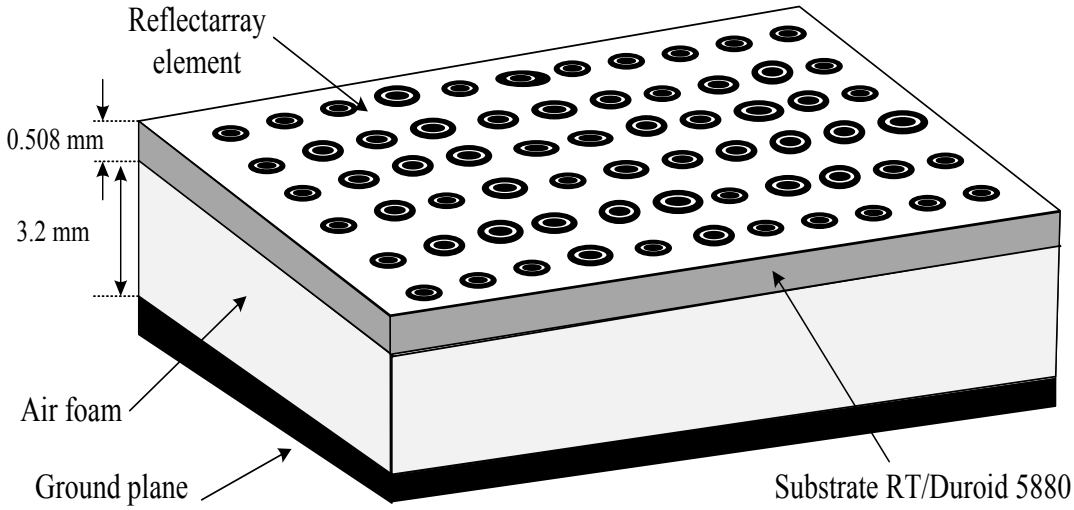

Fig. 43. 3D configuration of the reflectarray

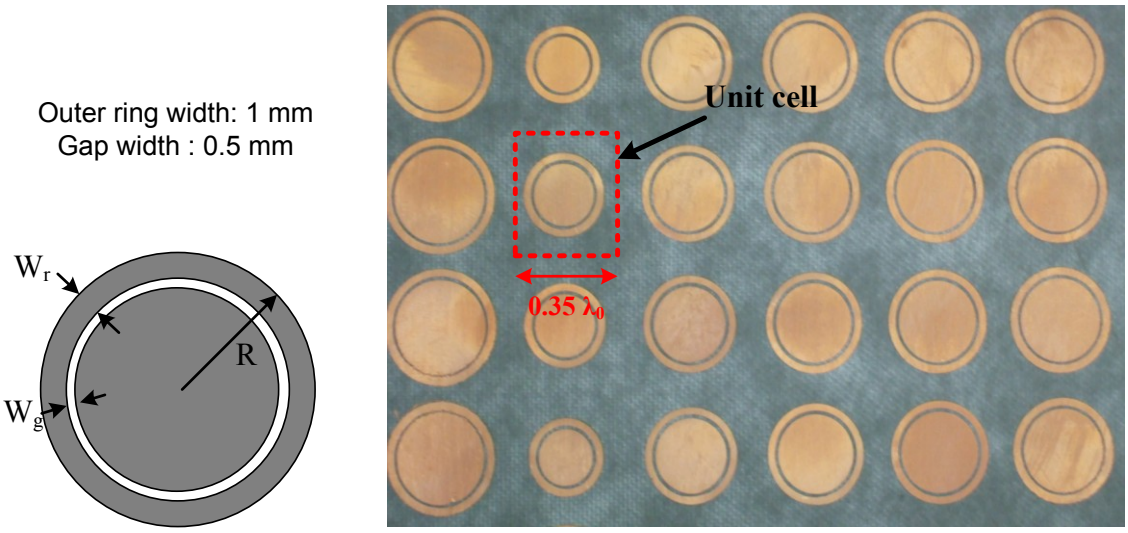

Fig. 44. Unit reflectarray element and its picture

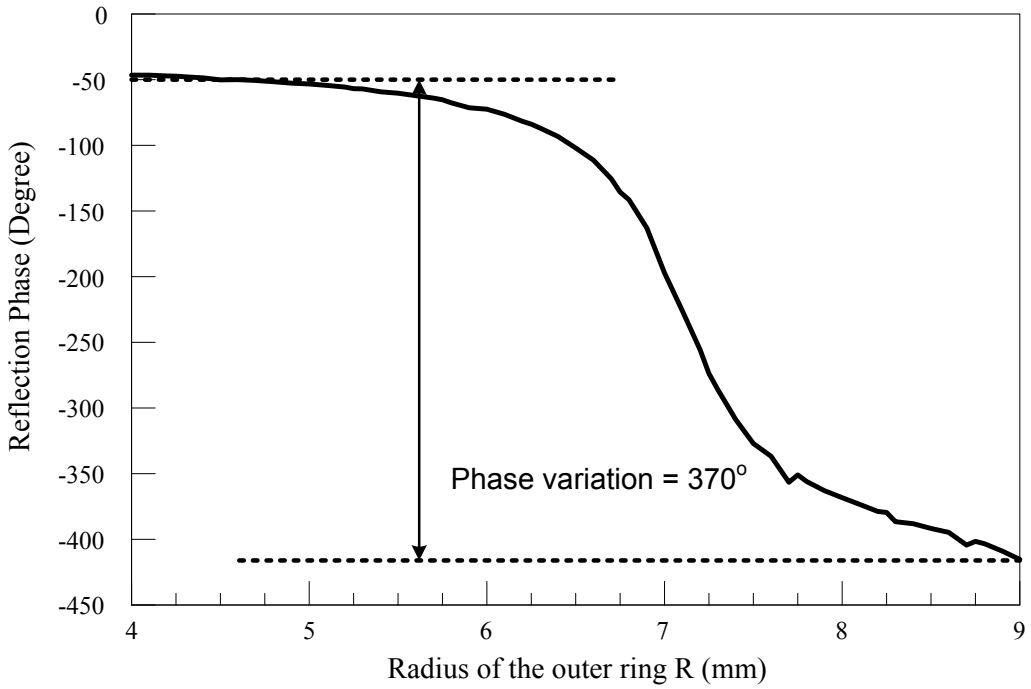

Fig. 45. Phase variation of the unit cell element

4. Rectifying Reflectarray

A novel rectenna array using a reflectarray which is called "rectifying reflectarray" here is presented in this chapter. The difference from the conventional reflectrarrays is that the feed antenna of a reflectarray is replaced with a rectifying antenna to generate DC energy. The rectenna with high gain property presented in the Chapter V and the reflectarray proposed with compact unit cell in this chapter are combined into a novel rectifying reflectarray.

Figure 46 shows the feed antenna designed to measure the gain of the reflectarray. The antenna component is the same with the antenna in the high gain rectenna circuits except the connected balun, instead of a rectifying circuit. The foam layer inserted between substrate and ground plane is not filled by a foam, but is supported by four plastic screws, which make thickness of the layer controllable. The measured radiation patterns of the feed antenna are shown in Figure 47. The maximum gain point is shifted slightly to -7^{o}. The shift could be due to that the balun makes current flow on the antenna unsymmetric. Maximum gain of the antenna in elevation plane is 10.2 dBi.

The reflectarray is measured with the pentagonal loop antenna located at focal point as shown in Figure 48. In the reflectarray design, q factor is 2 for the feed gain of 10 dBi and F/D is set by 0.6. So, almost 60 % maximum aperture efficiency is expected from the reflectarray theory. To avoid incident field blockage, the reflectarray has the offset feed with $\theta_0 = 20^{o}$.

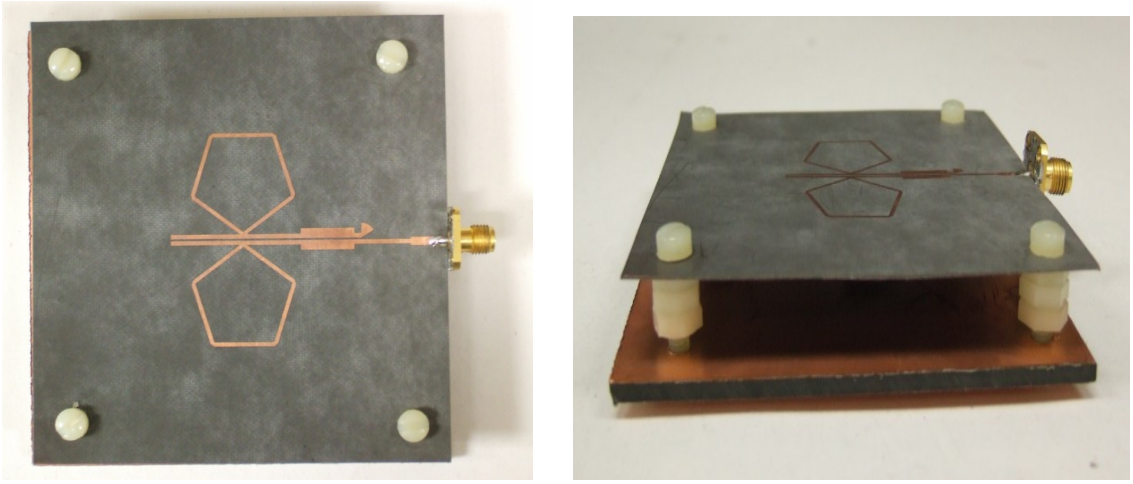

(a) (b)

Fig. 46. Feed antenna: (a) top view and (b) side view

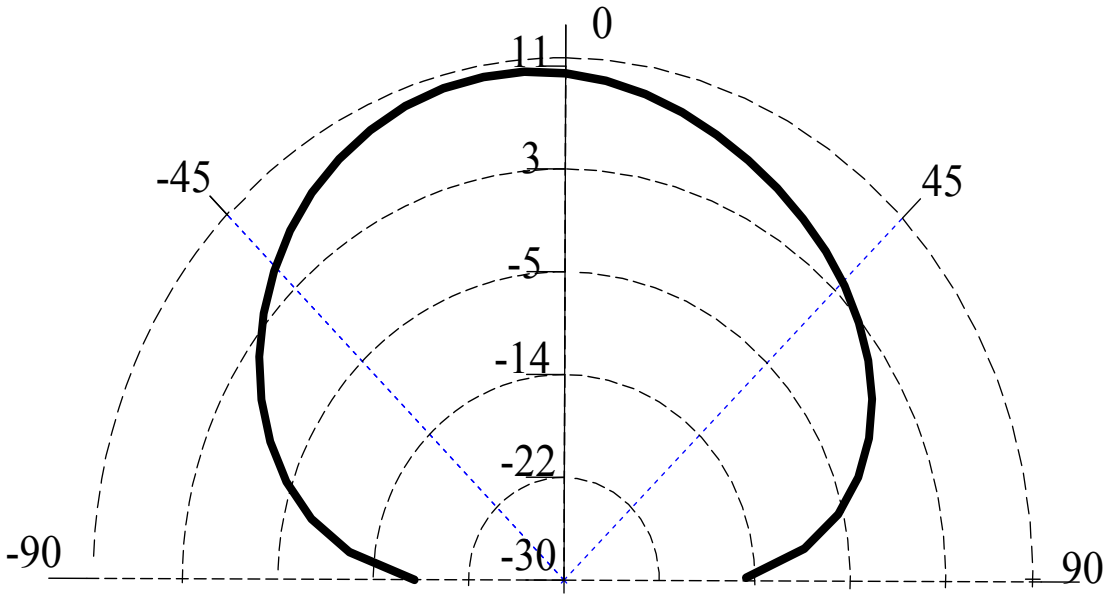

Fig. 47. Measured radiation patterns of the feed antenna in elevation plane

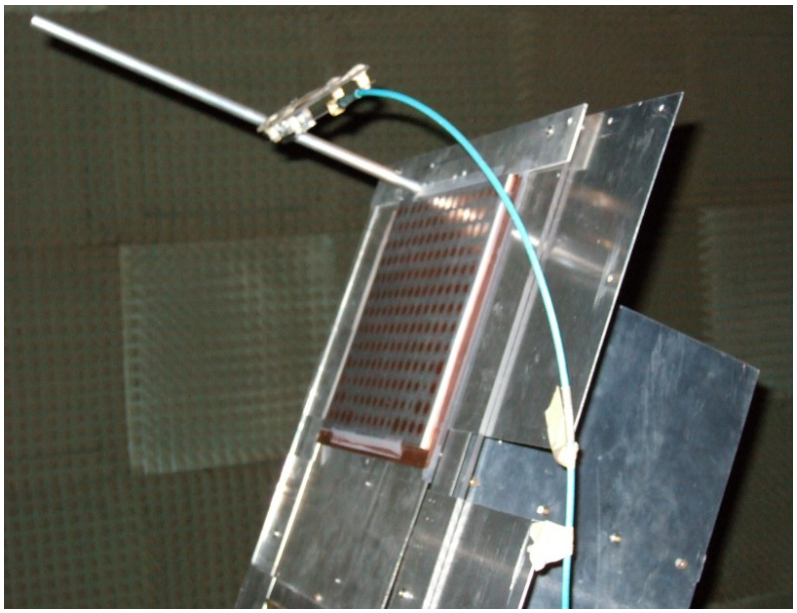

Fig. 48. Reflectarray with the feed antenna

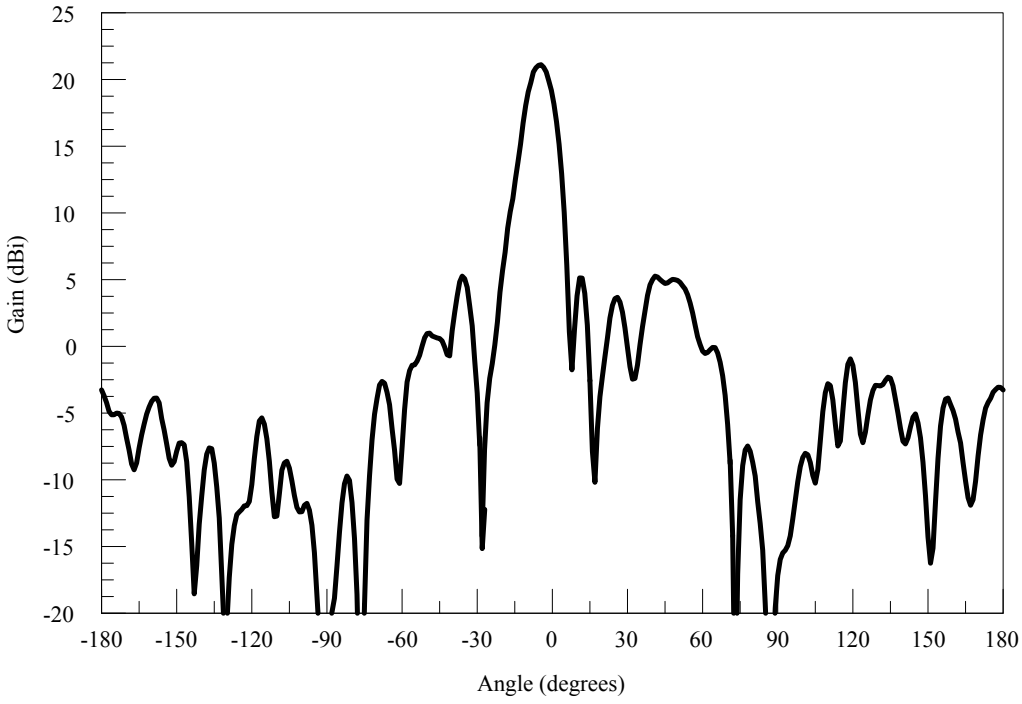

Fig. 49. Measured radiation pattern of the reflectarray at 5.8 GHz

The measured radiation pattern of the reflectarray at 5.8 GHz is shown in Figure 49. The main beam is at broadside and the 3 dB beam width is about 11^{o} . The peak sidelobe level relative to the main beam is 16.2 dB. The maximum gain of the reflectarray is 21.5 dBi, which is expected value from the reflectarray space configuration information.

Figure 50 shows the rectenna for the proposed rectifying reflectarray design. The rectenna is described in the Chapter V. The measured conversion efficiency curves of the rectifying reflectarray are shown in Figure 51. Like the single antenna case, the reflectarray rectenna achieves the maximume conversion efficiency of 71^{o} when the resistive load is 100 Ω. The conversion efficiency of 150 Ω load shows similar efficency results with the 100 Ω case. As the load resistance value increase, the efficiency gradually decreases.

5. Summary

Basic operation theory of the reflectarray is reviewed. Several efficiency terms are proposed, analyzed and derived to obtain the aperture efficiency of the reflectarray. Based on the design theory, a reflectarray with compact unit cell elements has been developed. The antenna component is measured with a balun and acheives 10.2 dB maximum gain. The reflectarray is measured with the feed antenna to check the gain of the reflectarray. The maximum gain is 21. 4 dBi. The proposed rectifying reflectarray with the rectenna located at the focal point is measured with several load resisters and achieved 71 % maximum conversion efficiency.

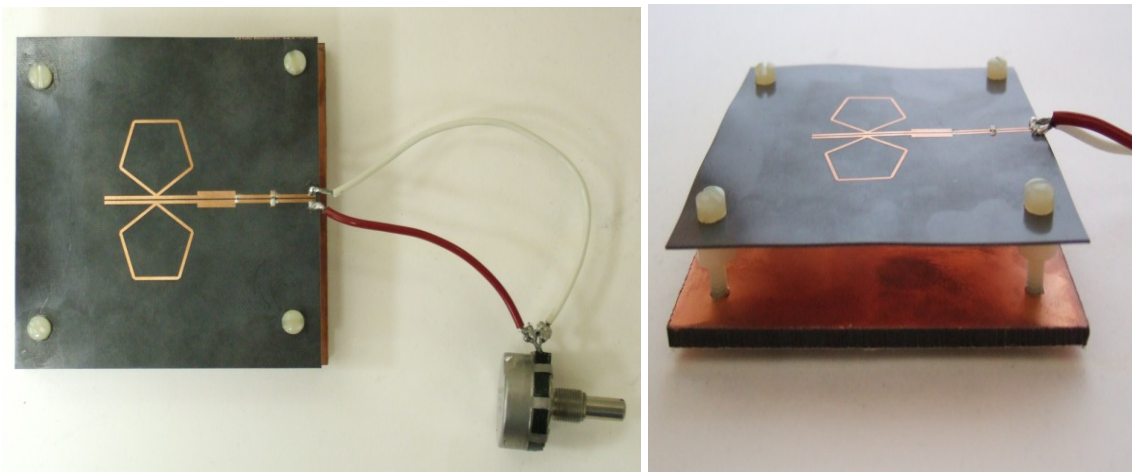

(a) (b)

Fig. 50. Rectifying antenna: (a) top view and (b) side view

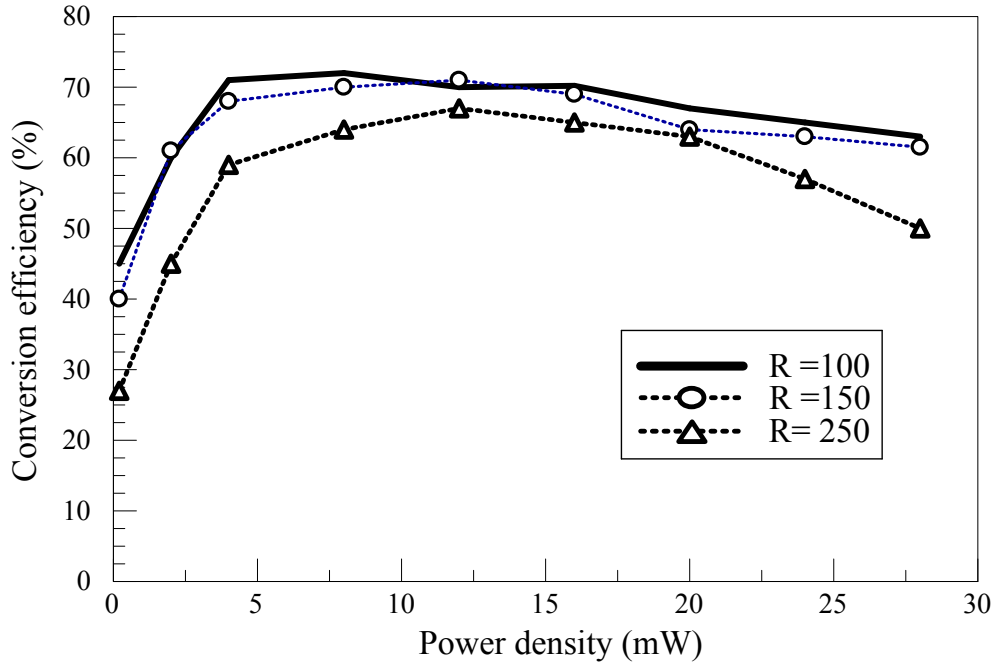

Fig. 51. Measured conversion efficiency of the rectifying reflectarray

As the first prototype of the reflectarray rectenna, the results are reasonable.

CHAPTER VII

MICROWAVE APPLICATIONS: WIDEBAND COPLANAR STRIPLINE TO DOUBLE-SIDED PARALLEL-STRIP LINE TRANSITION AND DUAL BAND OMNI-DIRECTIONAL ANTENNA FOR POLARIZATION DIVERSITY*

1. Introduction

A. Wideband Coplanar Stripline to Double-Sided Parallel-Strip Line Transition

The transition is a component to transfer electromagnetic energy from one type to another type of transmission line structure. As modern microwave systems have been demanded to be more complex and integrated with other types of components, the transition is considered a key element for optimal performance of the system. The transitions can be divided into two categories for the type of two transmission lines: balanced to balanced line transitions and balanced to unbalanced line transitions. The latter is especially called baluns. These transitions are used to feed CPS printed antennas and build baluns for balanced mixers, balanced amplifiers and antennas in many microwave applications.

---

*Parts of this chapter are reprinted with permission from C.-H. Ahn and K. Chang, "Wideband coplanar stripline to double-sided parallel-strip line transition," *IET Electronics Letters,* vol. 45, pp. 748-749, Jul. 2009. Copyright 2009 IET. The original version of this work is available at IET Digital Library; C.-H. Ahn, S.-W. Oh, and K. Chang, "A dual-frequency omnidirectional antenna for polarization diversity of MIMO and wireless communication applications," *IEEE Antennas and Wireless Propagation Letters*, vol. 8, pp. 966-969, Aug. 2009. Copyright 2009 IEEE. For more information go to http://thesis.tamu.edu/forms/IEEE%20permission%20note.pdf/view.

Double-sided parallel-strip line (DSPSL) is a new balanced transmission line with the advantage of good balanced performance, simple structure for wide-band transitions, and ability to realize various characteristic impedances and large capacitances due to its thin space between two conductors [87]. Recently, DSPSL has been actively studied for many microwave applications such as transitions [87], filters [88] and power dividers [89]. The coplanar stripline (CPS) is another attractive balanced line structure. The characteristics of the CPS are low loss, small discontinuity parasitics, and small dispersion, and simple implementation of open/short ended strips [90]. CPS can be used to mount the solid-state components in series or shunt without via holes. The uniplanar transmission line has been used in a number of applications such as antenna feedings, rectennas, filters, and optoelectronic devices. Many microstrip line to Coplanar waveguide (CPW) have been reported [91]. Wideband microstrip line to CPS transitions have been studied [92]. Broadband DSPSL to CPW transition has been also investigated [93]. However, no transition between CPS and DSPSL has been reported yet for two attractive balanced lines, the CPS and DSPSL. In this chapter, a wideband CPS to DSPSL transition is proposed for the first time. The characteristic impedance of CPS and DSPSL is 148 Ω and 50 Ω, respectively. The proposed back-to-back transition operates from 2.4 GHz to 10.7 GHz with the return loss of better than 10 dB and an insertion loss of better than 2.5 dB. It has simple structure and can be easily fabricated. The transition can be applied for many microwave applications.

B. Dual Frequency Omni-directional Antenna for Polarization Diversity

Wireless communication systems have been increasing rapidly for the last several years. Multiple-Input Multiple-Output (MIMO) technology has been used to improve wireless system performance because of its significant channel capacity and capability to offer multiple functions. For achieving better communication performance in specific areas, it has been considered important to determine a suitable diversity technique for MIMO system. Polarization diversity has been studied as an optimized MIMO technique for especially high multipath communication areas in substitute for space diversity, which needs at least ten wavelength spacing between two receiving antennas [94]. Polarization diversity system normally consists of two polarized antennas, which should have orthogonal polarization with the same radiation patterns of each other and high polarization purity for maximizing its capacity. A typical pair of the orthogonally polarized antennas is vertically polarized dipole and horizontally polarized magnetic dipole antenna. For lower frequency ranges, horizontally polarized small loop antennas may be the proper choice as a magnetic dipole. Its short total length, less than tenth of lamda, causes uniform current distribution on the surface, which leads to omnidirectional radiation pattern [95]. However, due to its difficult impedance matching condition, high reactance and small radiation resistance, the small loop antenna is not suitable at higher frequencies. After the first Alford loop antenna in the wire type at a high frequency was reported [96], several studies have been conducted using Alford loop structure to generate magnetic dipole radiation patterns [97]-[100] instead of small loop antennas. However, only single frequency horizontally polarization antennas have been

used so far. In this chapter, a novel printed dual-frequency Alford structure loop antenna is proposed. The dual frequency operation is achieved without any extra matching circuits or parasitic components. The horizontally polarized antenna consists of two wing sections with different diameters, which are resonating at 2.45 and 3.9 GHz. The effects of several design parameters of the proposed antenna are presented. The measured return loss and radiation patterns are compared with simulation results using HFSS design software, a 3D FEM based EM simulation. The proposed antenna could be used as a good candidate of one polarized antenna of a pair of orthogonally polarized MIMO system antennas.

2. Double-Sided Parallel-Strip Line

DSPSL has been analyzed first by Wheeler using conformal transformation mapping method. The analyses show the closed-form equations derived for symmetrical DSPSL separated by an air [101] and a dielectric layer [102]. However, by comparing with conventional microstrip lines, the characteristics of the symmetrical DSPSL can be found with less complexity using the symmetry. Figure 52 shows the configurations and their electric field distribution of the double-sided parallel-strip line (a) and the conventional microstrip line (b). The horizontal electric fields of symmetry in Figure 52 (a) generates zero potential plane located at Z = h/2 since the two conductors on top and bottom are identical in magnitude and opposite in phase by image theory. The zero potential plane can be considered as a virtual ground plane, which relates the

symmetrical DSPSL to the conventional microstrip lines. In Figure 52, the conductor width of the DSPSL and the microstrip is the same as W. The substrate height of the

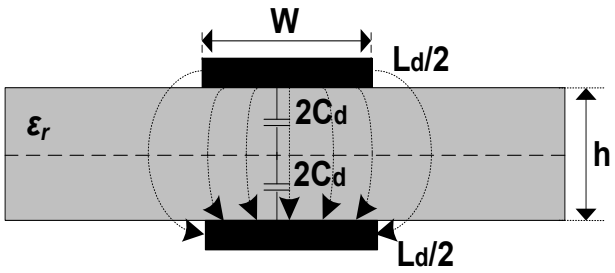

(a)

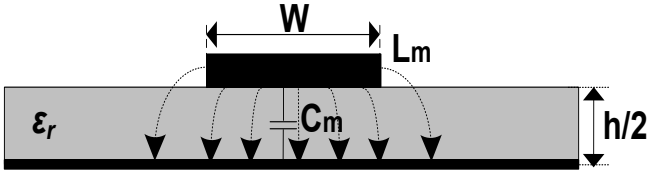

(b)

Fig. 52. Configurations of (a) symmetrical double-sided parallel-strip line and (b) conventional microstrip line

DSPSL, and the micristrip line is 2h and h, respectively. According to the image theory, it can be seen that the inductance per unit length of the DSPSL L_d is twice of that of the microstrip line L_m, and the capacitance per unit length of the DSPSL C_d is one half of that of the microstrip line C_m. Therefore, the characteristic impedance of the two cases can be given by

$$Z_{cd} = \sqrt{\frac{L_d}{C_d}} = \sqrt{\frac{2L_m}{C_m / 2}} = 2\sqrt{\frac{L_m}{C_m}} = 2Z_{cm} \tag{102}$$

where Z_{cd} and Z_{cm} is the characteristic impedance of the DSPSL and micristrip line, respectively. The equation (102) shows that characteristic impedance of the symmetrical DSPSL in Figure 52 (a) is twice of that of the microstrip line in Figure 52 (b). The characteristic impedance of the symmetrical DSPSL with the substrate height of h can also be expressed by the microstrip line's equations as

$$Z_c = 120(\varepsilon_{eff1})^{-1/2} \ln\left(\frac{4h}{w} + \frac{0.5w}{h}\right)[\Omega] \qquad for\ \frac{w}{h} \le 2 \tag{103}$$

$$Z_c = \frac{240\pi\left(\varepsilon_{eff2}\right)^{-1/2}}{\left(2w/h\right) + 1.393 + 0.667\ln(1.444 + 2w/h)}[\Omega] \quad for\ \frac{w}{h} \ge 2 \tag{104}$$

where $\varepsilon_{eff1} = (\varepsilon_r+1)/2+(\varepsilon_r-1)\{(1+6h/w)^{-1/2}+(1-2w/h)^2\}/2$ and $\varepsilon_{eff2} =(\varepsilon_r+1)/2+(\varepsilon_r-1)(1+6h/w)^{-1/2}/2$ are the effective permittivity for each cases and ε_r is the relative permittivity of the substrate height h/2. The equations (103), (104) may be useful for the DSPSL design due to the lack of calculating commercial tools for characteristic impedance of the symmetrical DSPSL. In comparison with the microstrip line of the same height, the DSPSL has wider stripline with the same characteristic impedance and shorter wavelength with the same stripline width.

3. Wideband CPS to DSPSL Transition

The electric fields of both CPS and DSPSL have similar characteristics. They are identical in magnitude and opposite in phase on two conductors as balanced lines. However, their field distributions are rotated 90° from each other. Figure 53 (a)-(c) show

the configurations of the proposed double-sided parallel-strip line transition. The CPS has electric fields formed across two conductor strips on top layer shown in Figure 53 (a). On the other hand, DSPSL produces vertical electric fields from conductor strips located on top and bottom layer as shown separately in Figure 53 (b) and (c). The proposed transition is designed to gradually change the electric fields of CPS mode to those of DSPSL mode. The transition on top side is directly connected to both CPS and DSPSL. That is, the width of one conductor of the transition on the top side is tapered from the width of the CPS to the width of the DSPSL as shown in Figure 52 (b). The conductor of the transition on the bottom side is electromagnetically coupled with one of conductor of the CPS located on the top side. This bottom conductor of the transition is tapered from the same location of the end part of the CPS in the z direction to the conductor of the DSPSL as shown in Figure 53 (c). A radial stub at the end of the CPS is designed for broadband coupling between the top and bottom conductors. Figure 54 shows the electric field distributions and cross sectional views at three different locations. Figure 54 (a) shows CPS mode at A-A' location which has electric fields in the y-axis. The horizontally distributed electric fields of the CPS mode are converted to the vertical distribution in the DSPSL mode at C-C' location of Figure 54 (c), through the proposed transition mode in the x and y – axis at B-B' location shown in Figure 54 (b). The structures are all printed on substrate RT/Duroid 5870 with thickness (h) of 31 mil (0.7874 mm) and a dielectric constant (εr) of 2.31. The 148 Ω characteristic impedance of the CPS is determined by IE3D simulation with the strip width (W1) of the CPS of 3.5 mm, and the gap between two strips (g) of 0.8mm. The DSPSL width of the 50 Ω

characteristic impedance (W2) is 3.07 mm. The transition length (Lt) is 25 mm. The angle (Θ) of the radial stub is optimized as 80° for good performance.

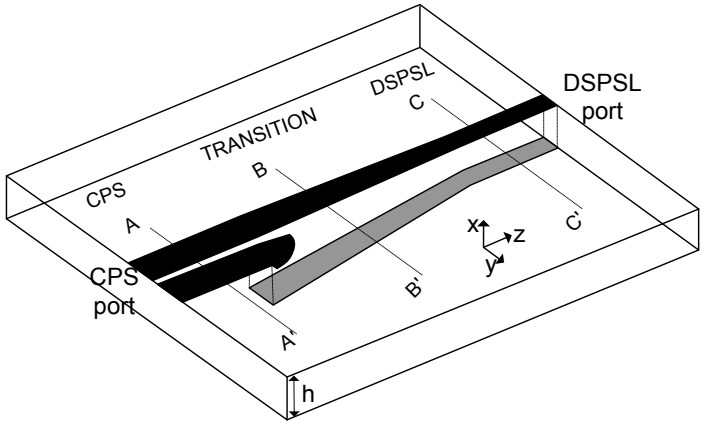

(a)

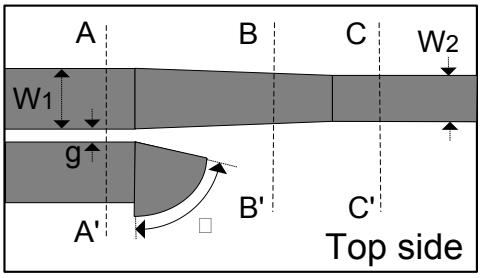

(b)

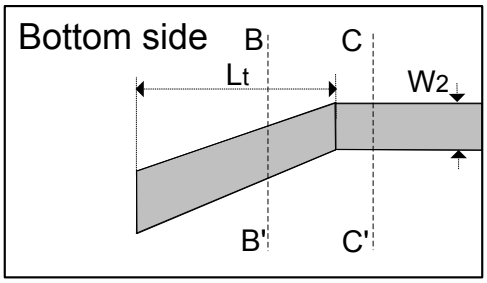

(c)

Fig. 53. Configurations of the proposed CPS to DSPSL transition: (a) 3D view, (b) top side, and (c) bottom side

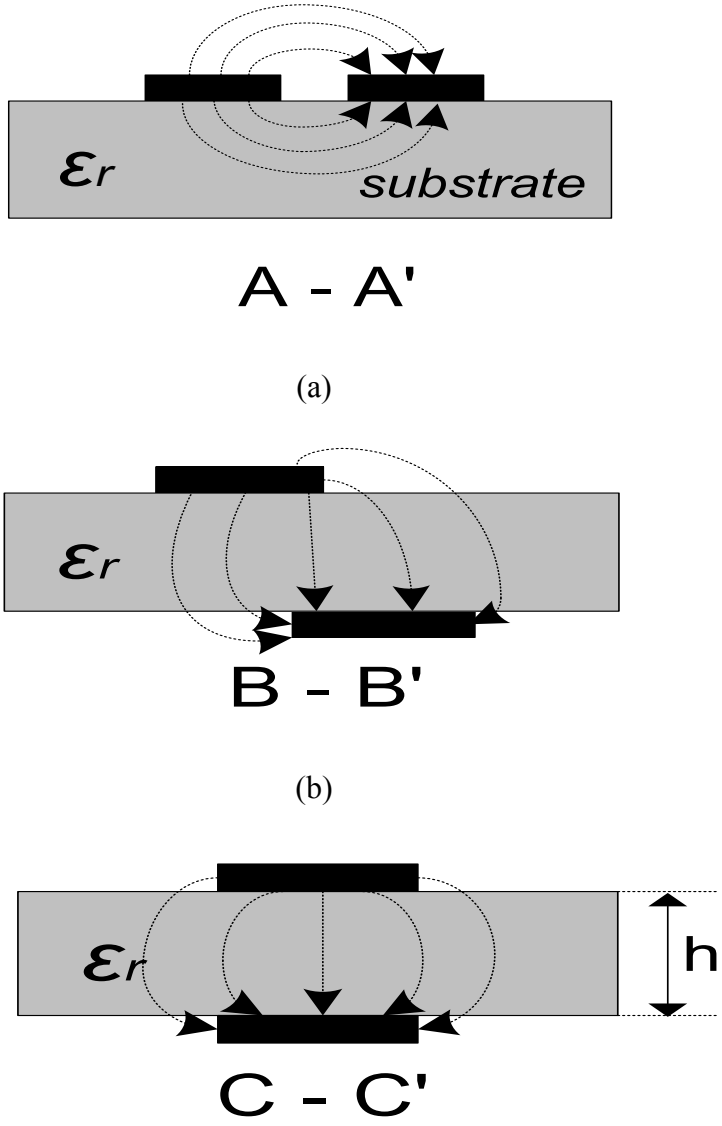

Fig. 54. Cross-sectional views of the proposed transition and electric field distributions: (a) CPS mode, (b) Transition mode, and (c) DSPSL mode

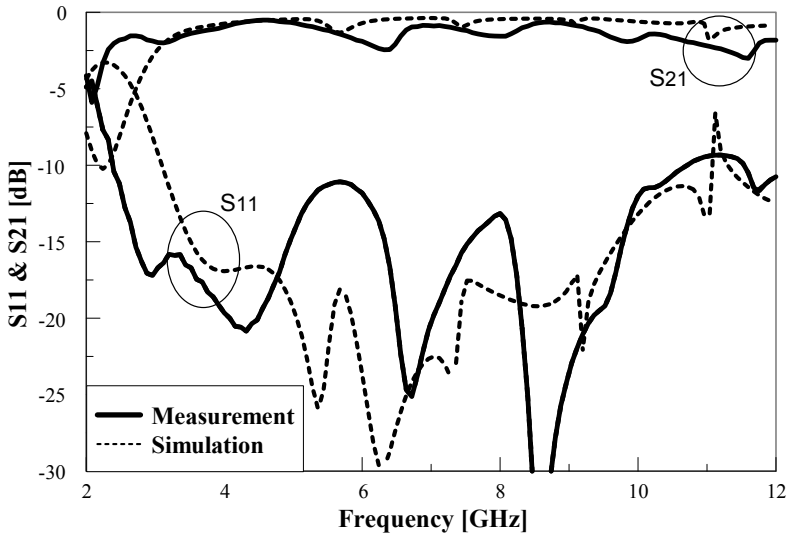

Fig. 55. Simulated and measured results of a CPS to DSPSL back to back transition

The return loss and insertion loss of a back-to back transition were simulated and measured using IE3D (a method of moment based EM simulator) and HP 8510 network analyzer, respectively. Figure 55 shows the simulated and measured results of a CPS to DSPSL back-to-back transition. The measured return loss of better than 10 dB and insertion loss of better than 2.5 dB of the back-to-back transition are achieved from 2.4 GHz to 10.7 GHz. The 1.5 dB insertion loss bandwidth is obtained from 3.44 GHz to 5.74 GHz and from 6.64 GHz to 9.52 GHz. The insertion losses also include line sections and discontinuities between the limited widths of the DSPSL and two coaxial connectors for measurement purpose. The actual insertion losses for the transition are lower.

4. Dual Frequency Omni-directional Antenna

The configuration of a dual frequency omnidirectional loop antenna (DOLA) is shown in Figure 56. The current distributions on both the top plane and the bottom plane are shown in Figure 56 (a) and Figure 56 (b). The waves on the cross-shaped double sided strip lines are guided due to the opposite current directions on both sides. The eight outer wing structures generate radiation fields caused by a uniform one direction current distribution which causes omnidirectional radiation characteristics. Figure 56 (c) shows a combined structure with the total current distributions. The two current distributions on the wings generate two different omnidirectional radiation fields. The side view of the proposed antenna is shown in Figure 54 (d). The proposed antenna is printed on substrate RT/Duroid 5880 with thickness and a dielectric constant of 62 mil (1.57 mm)

TABLE 3. The design parameters of the dual band Omni-directional loop antenna [unit:mm]

L1	L2	r1	r2	w	t1	t2
19.0	8.4	23.7	10.8	1.9	0.4	0.0

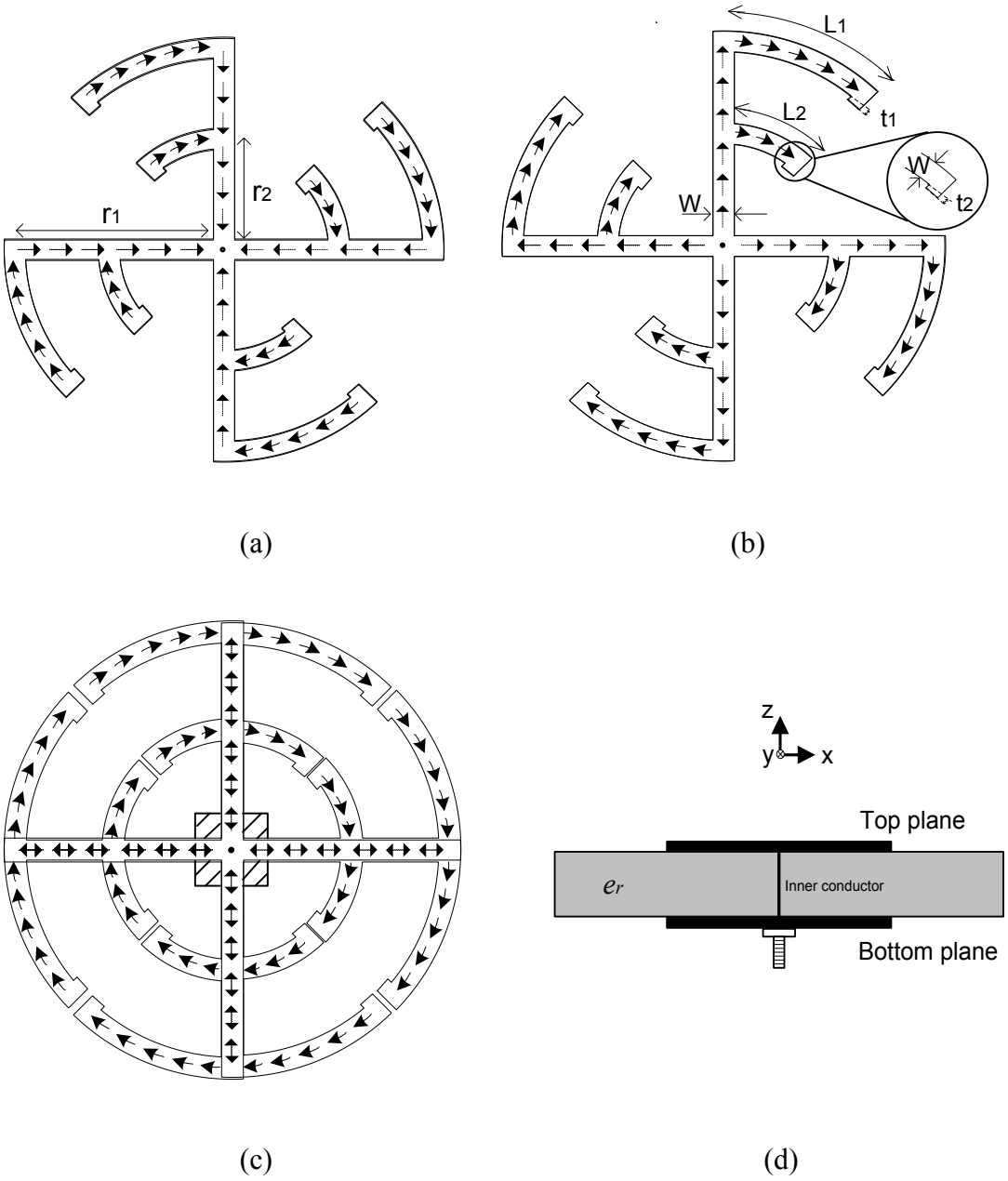

(a) (b)

(c) (d)

Fig. 56. (a) Top plane conductor and its current distributions, (b) bottom plane conductor and its current distributions, (c) top view of the combined antenna and current distributions, and (d) side view of the proposed antenna

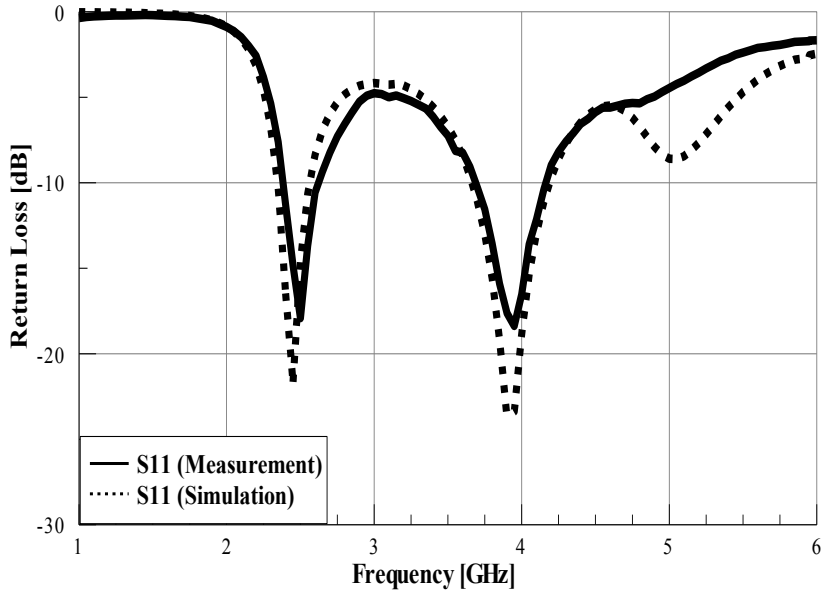

Fig. 57. Simulation and measurement results of return loss

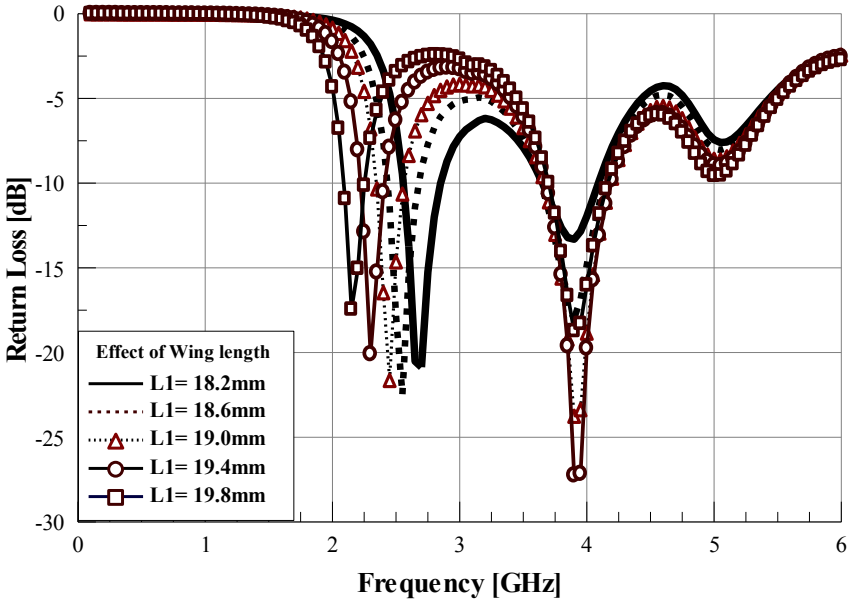

Fig. 58. Simulation results of wing length's effect

and 2.2, respectively. The specific values of the proposed antenna dimensions are shown in Table I.

Figure 57 shows the return loss of the proposed DOLA. The measured return losses at 2.45 GHz and 3.9 GHz are 18 dB and 19dB, respectively. The simulation results are matched well with the measured results. From the results, it can be seen that the proposed antenna does not require any matching circuits to generate the dual band performance. The design for the dual band omnidirectional antenna was optimized from a tradeoff among several design parameters. The important tuning parameters are wing lengths (L), width (w), and stub lengths (t) of the wing end-part. Figure 58, 59, and 60 show the simulation results regarding the effects of these parameters. To investigate the effects of wing length in Figure 58, L2 is fixed as 8.4 mm and L_1 is varied from 11 mm to 12 mm by 0.2 mm increments. As L_1, the length of wing, is increased, the resonant frequency is decreased at lower frequency band as expected. Similarly, when L_2 is varied, the change of resonant frequency happens at higher frequency band. Even with slight change of the wing length, the resonant frequency is changed significantly. From the fact of Figure 58, one can see that the wing length is a dominant design parameter for resonant frequency.

Figure 59 shows the effects of wing width, which does not show a strong relationship with resonant frequency. Resonant points are not varied by changing the wing width. However, better return loss can be achieved by optimizing the wing width. Thus, wing width can be used to optimize the impedance matching at specific resonant point. In this case, W=1.9 mm provides the best matching at both two resonant

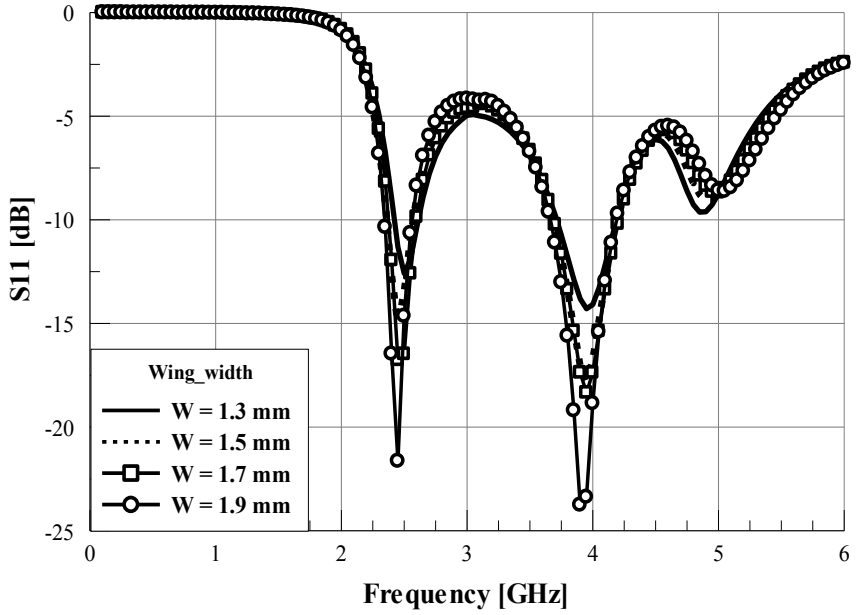

Fig. 59. Simulation results of wing width's effect

frequencies, 2.45 GHz and 3.9 GHz. The effects of the stub length at lower frequency band are shown in Figure 60. The resonant frequencies are shifted slightly by using different stub lengths of t_1 from 0 mm to 3.0 mm. From the results of Figure 60 (a), the stub length affects the first resonant frequency, but not strongly. One can see another effect of the wing stub length in Figures 60 (b) and (c), which show radiation patterns in the azimuth plane with two different stub lengths, t_1=0 mm and 0.4 mm. Figure 60 (b) shows less perfect omnidirectional radiation patterns with t_1=0 mm. Figure 60 (c) shows almost perfect omnidirectional patterns with t_1=0.4 mm. Only 0.4 mm difference of stub length causes a quite significant change in radiation patterns. The same effect happens at higher frequency band when t_2 is changed. It can be seen that a small amount of coupling between two adjacent wings with proper stub lengths can cause the current distributions

on the entire wing to be more constant. The constant current distribution will make almost perfect omnidirectional radiation patterns similar to a small loop antenna. Thus, the stub dimensions should be considered as parameters for better radiation patterns as well as resonant frequency.

The radiation patterns of the proposed antenna are measured and simulated at resonant frequencies. Figure 61 (a) and (b) show measured and simulated radiation patterns of the proposed antenna in the azimuth and elevation plane, respectively, at 2.45 GHz. Excellent omnidirectional radiation patterns in both simulation and measurement results have been achieved. The measured polarization purities in the azimuth and the elevation plane are around 20dB and 15dB, respectively. The lower value of the polarization purity in elevation might be due to measurement errors. Figure 62 (a) and

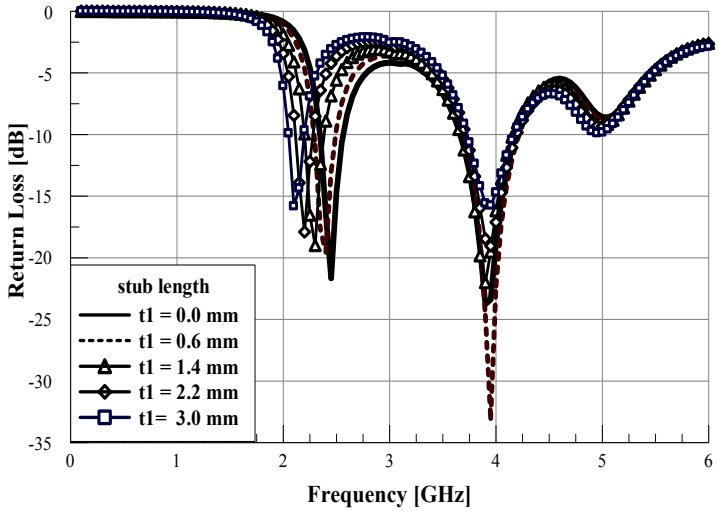

(a)

Fig. 60. (a) Simulated result of return loss of stub length, (b) Radiation pattern in azimuth plane at 3.9 GHz with t_1 = 0.0 mm and t_2 = 0.0 mm, and (c) Radiation pattern in azimuth plane at 3.9 GHz with t_1 = 0.4 mm and t_2 = 0.0 mm

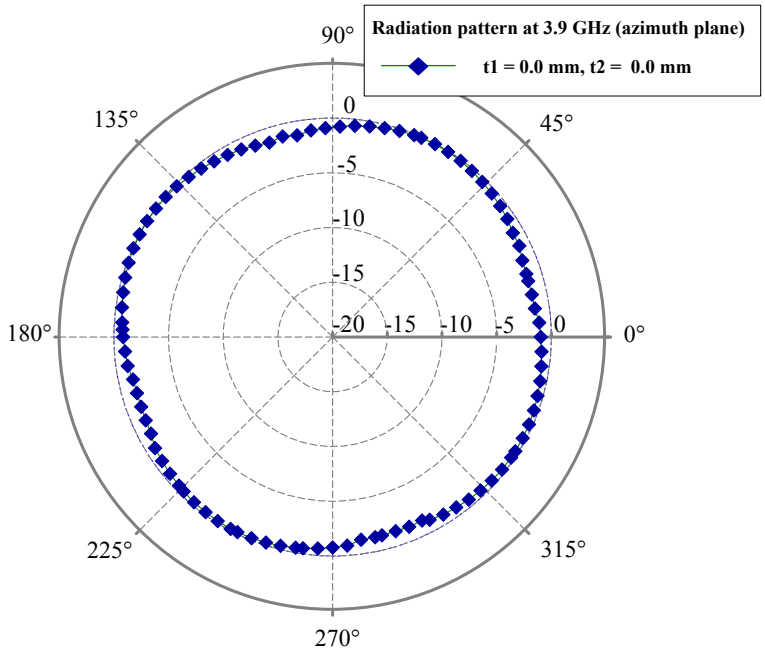

(b)

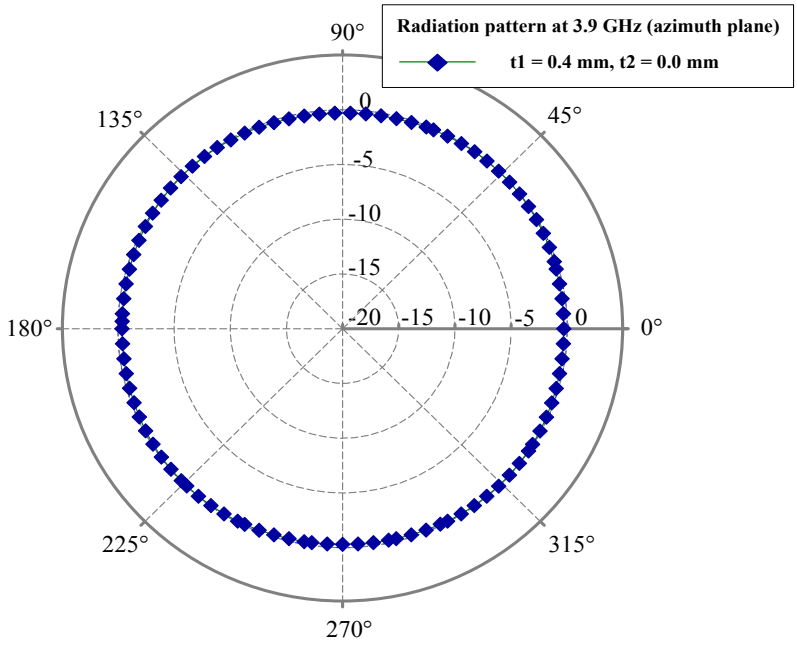

(c)

Fig. 60. Continued

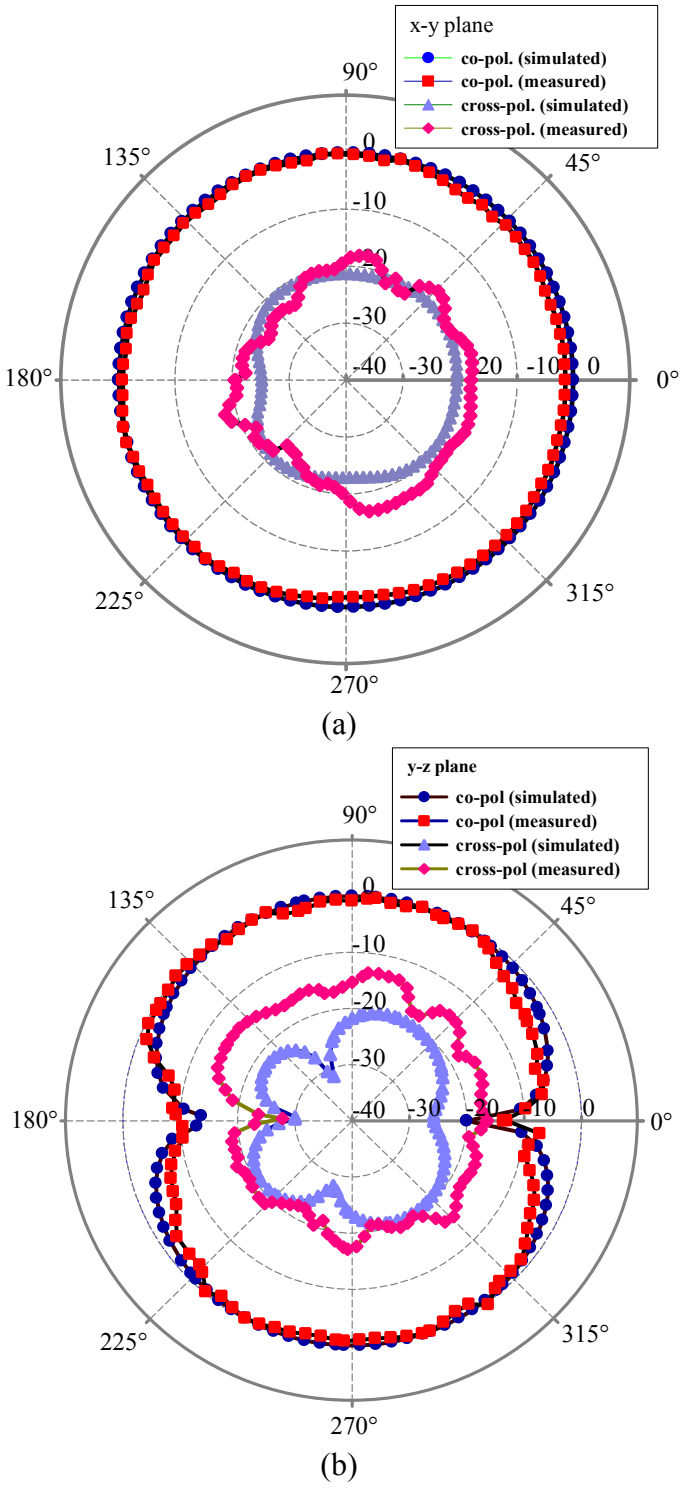

Fig. 61. Simulated and measured radiation patterns at 2.45 GHz:
(a) x-y plane and (b) y-z plane

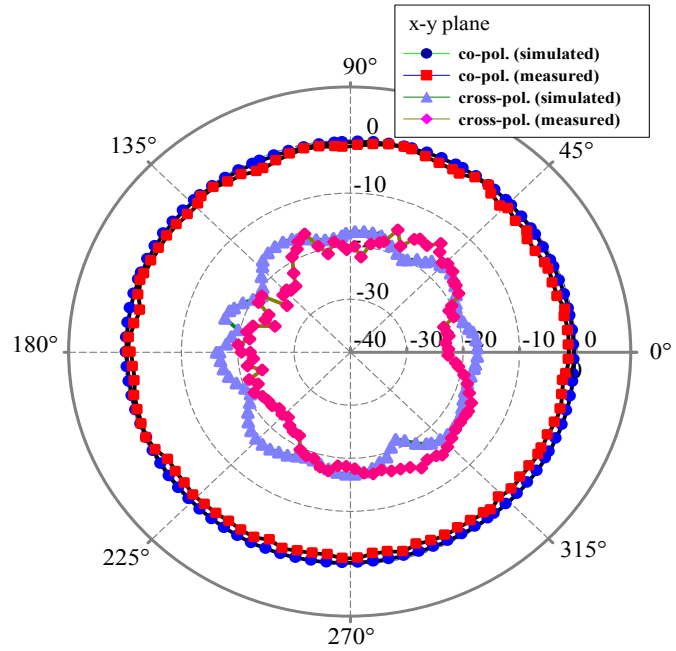

(a)

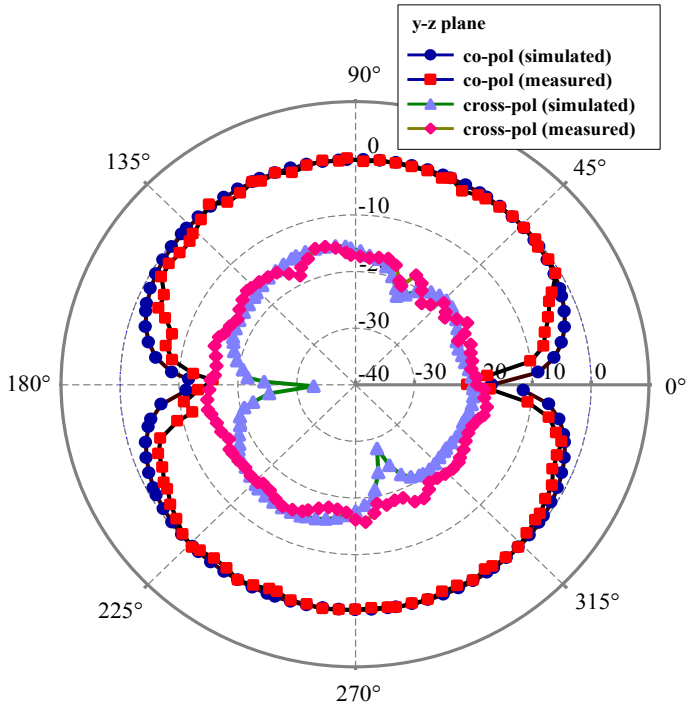

(b)

Fig. 62. Simulated and measured radiation patterns at 3.9 GHz:

(a) x-y plane and (b) y-z plane

(b) show measured and simulated radiation in the azimuth and elevation plane, respectively, at 3.9 GHz. The radiation patterns are good enough to be a vertically polarized antenna of polarization diversity. Polarization purity is around 18 dB for both cases. The maximum measured antenna gains are 1.7 dBi and 1.2 dBi at 2.45 GHz and 3.9 GHz, respectively. Figure 63 shows the fabricated dual band omnidirectional antenna used for measurements.

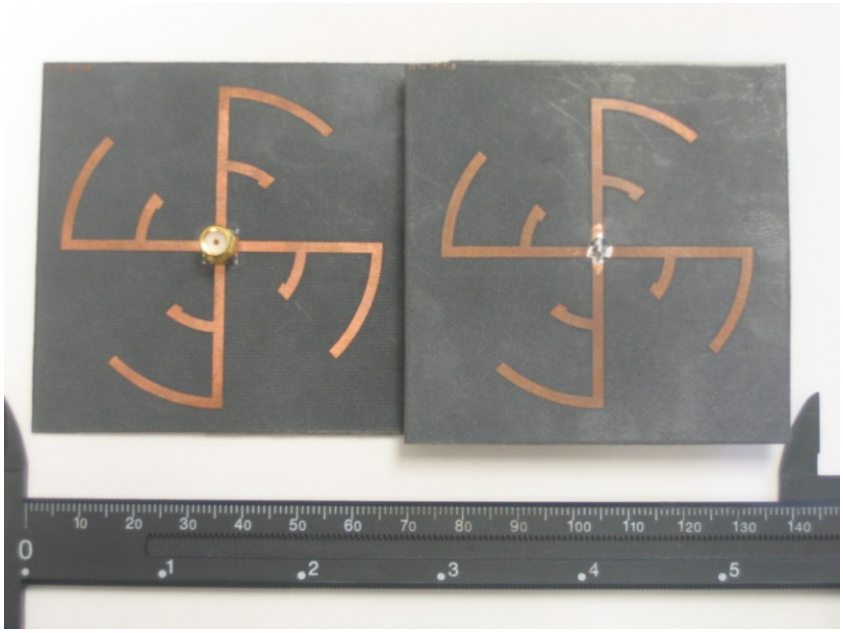

Fig. 63. The fabricated antenna (left: top view, right: bottom view)

5. Summary

The first CPS to DSPSL wideband transition has been designed and measured. The proposed transition has very simple and low cost structure. The simulated results show a good agreement with the measured results up to 12 GHz. With the return loss of better than 10 dB, the 2.5 dB and the 1.5 dB insertion loss have been obtained from 2.4 GHz to 10.7 GHz and 3.44 GHz to 5.74 GHz & 6.64 GHz to 9.52 GHz, respectively. This transition can be useful in many applications, especially, for feeding antennas and easy integration with microwave passive and active components.

A dual band omni-directional loop antenna has been proposed for polarization diversity of the MIMO system and other applications. The antenna configuration is based on Alford loop antenna type. Several design parameters are optimized for both dual frequency resonance and omni-directional radiation without using additional matching circuits. By adjusting wing length and width, dual band resonance can be achieved. The better omni-directional radiation pattern could be achieved by adjusting length of wing stub. The proposed dual band loop antenna has the performance enough to be a counterpart of a vertically oriented dual band dipole antenna for polarization diversity and other communication systems. The antenna might be a multi-band horizontally polarized antenna with different sizes of wings for other wireless communication applications.

CHAPTER VIII

SUMMARY AND RECOMMENDATIONS

1. Summary

In this dissertation, developments of various microwave applications using a metamaterial component called complementary split ring resonators and a high gain rectifying array using a reflectarray for wireless power transmission has been focused mainly. A compact microstrip bandpass filter and a diplexer based on CSRRs have been developed. It has been shown that in the microstrip filter designs, using CSRRs is useful for especially size reduction. As the first antenna design using CSRR as the only radiator, a CSRR dual band antenna fed by CPW has been developed. The antenna also shows compactness of its size, comparing with the conventional slot ring antennas. As the wireless power transmission applications, several array rectennas have been studied to obtain a long distance range and higher output DC power. But, in the array rectenna design, several problems exist: the relatively high loss of the array feed networks, difficulty in feeding network design, and antenna coupling causing lower rectenna array performance. To overcome these downsides, a novel rectifying antenna using a reflectarray has been developed. It has been shown that using the reflectarray is the preferred method for high power rectenna design due to its design simplicity, low loss, and good performance. The research topics and accomplishments covered in this dissertation are summarized chapter by chapter in the followings.

In Chapter II, fundamentals of left-handed metamaterials have been described. From Maxwell's equations, phase constant term is derived and it is clearly shown that its negative value is selected in a negative permittivity and negative permeability (DNG) medium while its positive value is selected in a DPS medium. The negative phase constant results in negative phase velocity and negative index of refraction in the medium. Complementary split ring resonator (CSRR) as a useful metamaterial component has been described. The resonant frequencies of the CSRR are strongly related with the dimensions of their structures. CSRR is excited with the E field of the electromagnetic wave along with the axis of the CSRR. As a result, the CSRR exhibits negative permittivity in a certain frequency band.

In Chapter III, a parallel coupled line bandpass filter based on CSRR has been proposed. The parallel coupled transmission lines provide bigger value of coupling capacitance, resulting in better bandpass characteristics with two CSRRs only. The measured insertion loss of 1.4 dB with a compact size of 0.32 λg X 0.14 λg has been achieved at 3.6 GHz. Two microstrip CSRR bandpass filters are designed and they are connected to design a compact microstrip diplexer. The diplexer takes an input signal from port 1 and transfers the signal of 3.1 GHz to port 2 and the signal of 4.2 GHz to port 3. The smulated and measured results matches well with each other. The measured insertion loss is 1.8 dB for port 2 and 2.3 dB for port 3.

In Chapter IV, a compact dual-frequency antenna using complementary sprit ring resonators has been developed. The CSRR antenna is fed by coplanar waveguide. The

dimensions of the rectangular CSRRs are tuned to achieve dual band frequency properties. The higher resonant frequency is dominantly determined by the outer slot ring while the lower resonant frequency is generated by the coupling between two slots rings, which are CSRRs. The proposed antenna achieves about 35% size reduction effect at the low resonant frequency. The proposed metamaterial inspired antenna obtains 4.7 dBi and 2 dBi of measured gains at 2.6GHz and 4.5GHz, respectively.

In Chapter V, WPT system and rectenna operation theory have been reviewed. A pentagonal loop antenna has been developed at 5.8 GHz. The pentagonal loop provides linear polarization and achieves high gain of 10.1 dBi. The CPS feed line is designed with characteristic impedance of 184 Ω. A impedance transfermer is used to match the antenna input impedance to the diode input impedance. The proposed rectenna achieves a maximum conversion efficiency of 75% with the resistivie load of 100 Ω.

In Chapter VI, basic operation theory of the reflectarray has been reviewed. Several efficiency terms are analyzed and derived to obtain the aperture efficiency of the reflectarray. Based on the design theory, a reflectarray with compact unit cell elements has been developed. The reflectarray is measured with the feed antenna to achieve the maximum gain of 21.4 dBi. The proposed rectifying reflectarray with one element rectenna located at the focal point is measured with several load resisters and achieved 71 % maximum conversion efficiency.

In Chapter VII, two microwave applications has been developed. The wideband transition between CPS and DSPSL has been first developed. The proposed transition has very simple and low cost structure. The simulated results show a good agreement

with the measured results up to 12 GHz. With the return loss of better than 10 dB, the 2.5 dB and the 1.5 dB insertion loss have been obtained from 2.4 GHz to 10.7 GHz and 3.44 GHz to 5.74 GHz & 6.64 GHz to 9.52 GHz, respectively. As another microwave application, a dual band omni-directional loop antenna has been developed for polarization diversity of the MIMO system and other communication applications. Several design parameters are optimized for both dual frequency resonance and omni-directional radiation without using additional matching circuits. By adjusting wing length and width, dual band resonance can be achieved. The proposed dual band loop antenna has achieved the performance enough to be a counterpart of a vertically oriented dual band dipole antenna for polarization diversity and other communication systems.

2. Recommendations for Future Research

Several applications using CSRRs have been developed so far. Although the performances of the circuits using metamaterial components are better than those of the conventional circuits, it is difficult to verify that the circuits are fully metamaterialized at certain frequency. A reasonable verification method is needed as a next metamaterial research topic.

A compact diplexer and a dual band antenna based on CSRRs have been developed. With similar concept or by adding good ideas, design of a compact multiplexer and a compat (C)SRR antenna with a good performance will be the next research topics.

REFERENCES

[1] V. Veselago, “The electrodynamics of substances with simultaneously negative values of ε and μ,” *Soviet Physics Uspekhi*, vol. 10, no. 4, pp. 509-514, Jan., Feb. 1968.

[2] J. B. Pendry, A. J. Holden, D. J. Robbins, and W. J. Stewart, “Low frequency plasmons in thin-wire structure,” *J. Phs. Condens. Matter*, vol. 10, pp. 4785-4809, 1998.

[3] J. B. Pendry, A. J. Holden, D. J. Robbins, and W. J. Stewart, “Magnetism from conductors and enhanced nonlinear phenomena,” *IEEE Transactions Microwave Theory and Techniques*, vol. 47, no. 11, pp. 2075-2084, Nov. 1999.

[4] J. B. Pendry, “Negative refraction makes a perfect lens,” *Physical Review Letters,* vol. 85, no. 18, pp. 3966-3969, Oct. 2000.

[5] D. R. Smith, W. J. Padillia, D. C. Vier, S. C. Nemat-Nasser, and S. Schultz, “Composite medium with simultaneously negative permeability and permittivity,” *Physical Review Letters* vol. 84, no. 18, pp. 4184-4187, May 2000.

[6] R. A. Shelby, D. R. Smith, S. Schultz, “Experimental verification of a negative index of refraction,” *Science,* vol. 292. no. 5514, pp. 77 – 79, April 2001.

[7] C. Caloz and T. Itoh, "A novel mixed conventional microstrip and composite right/left-handed backward-wave directional coupler with broadband and tight coupling characteristics," *IEEE Microwave and Wireless Components Letters,* vol. 14, pp. 31-3, Jan. 2004.

[8] N. Engheta, "An idea for thin subwavelength cavity resonators using metamaterials with negative permittivity and permeability," *IEEE Antennas and Wireless Propagation Letters,* vol. 1 no. 1, pp. 10-13, 2002.

[9] A. Alu and N. Engheta, "Guided modes in a waveguide filled with a pair of Single-Negative (SNG), Double-Negative (DNG), and/or Double-Positive (DPS) layers,"

IEEE Trans. Microwave Theory Tech., vol. 52, pp. 199-210, Jan. 2004.

[10] B. Wu, T. M. Grzegorczyk, Y. Zhang and J. A. Kong, "Guided modes with imaginary transverse wave number in a slab waveguide with negative permittivity and permeability," *Journal of Applied Physics,* vol. 93, pp. 9386-9388, June 2003.

[11] N. Engheta, "Ideas for potential applications of metamaterials with negative permittivity and permeability," *Advances in Electromagnetics of Complex Media and Metamaterials*, *Physical Review Letters,* vol. 93, pp. 10841-1, Mar. 2002.

[12] A. Grbic and G. V. Eleftheriades, "Overcoming the diffraction limit with a planar left-handed transmission-line lens," *Physical Review Letters,* vol. 92, pp. 117403-1, Mar. 2004.

[13] J. Lu, T. M. Grzegorczyk, Y. Zhang, J. Pacheco Jr., B. Wu, J. A. Kong and M. Chen, "Cerenkov radiation in materials with negative permittivity and permeability," *Optics Express,* vol. 11, pp. 723-734, Apr. 2003.

[14] A. Grbic and G. V. Eleftheriades, "Experimental verification of backward-wave radiation from a negative refractive index metamaterial," *Journal of Applied Physics,* vol. 92, pp. 5930-5935, Nov. 2002.

[15] M. Cheney, *Tesla Man out of Time*, Englewood Cliffs, NJ: Prentice-Hall, 1981.

[16] H. Yagi and S. Uda, "On the feasibility of power transmission by electric waves," in *Proc. of the Third Pan-Pacific Science Congress*, Tokyo, Vol. 2,1926, pp. 1305-1313.

[17] "Electric light without current," *Literary Digest*, vol. 112, no. 3, pp. 30, Jan.16, 1932.

[18] W. C. Brown, .The history of power transmission by radio waves,. *IEEE Transactions Microwave Theory and Techniques*, vol. MTT-32, no. 9, pp.1230-1242, Sep. 1984.

[19] W.C. Brown, R. H. George, N. I. Heenan, and R. C. Wonson, "Microwave to dc converter, " United States Patent. No. 3434678, Mar. 1969.

[20] W.C. Brown, "Electronic and mechanical improvement of the receiving terminal of a free-space microwave power transmission system," Raytheon Company, Wayland,

MA, Tech. Rep. PT-4964, NASA Rep. CR-135194, Aug. 1977.

[21] P. E. Glaser, "Method and apparatus for converting solar radiation to electrical power," United States Patent, no. 3781647, Dec. 1973.

[22] P. E. Glaser, O. E. Mayard, J. Mockovciak, Jr. and E. L. Ralph, *Feasibility Study of a Satellite Solar Power Station*, NASA Lewis Research Center, Cleveland, OH, NASA Report CR-2357, 1974.

[23] Rockwell International, *Satellite Power System (SPS) Concept Definition Study*, NASA Marshall Space Flight Center, Huntsville, AL, NASA Contract no. NAS-8-32475, 1980.

[24] R. M. Dickinson and W. C. Brown, "Radiated microwave power transmission system efficency measurements," *Jet Propulsion Laboratory, Cal. Tech., Tech. Memo*, pp. 33-727, March 15, 1975.

[25] N.shinohara and H. Matsumoto, "Experimental study of large rectenna array for microwave energy transmission," *IEEE Transactions Microwave Theory and Techniques*, vol. 46, no. 3, pp. 261-268, March 1998.

[26] L. W. Epp, A. R. Khan, H. K. Smith, and R. P. Smith, " A compact dual-polarized 8.51 GHz rectenna for high-voltage (50 V) actuator applications," *IEEE Transactions Microwave Theory and Techniques*, vol. 48, no. 1, pp. 111-120, January 2000.

[27] B. Strassner, K. Chang, "5.8-GHz circularly polarized dual-rhombic-loop traveling-wave rectifying antenna for low power-density wireless power transmission applications," *IEEE Transactions Microwave Theory and Techniques*, vol. 51, no. 5, pp. 1548-1553, January 2000.

[28] B. Strassner, K. Chang, "Highly efficient C-band circularly polarized rectifying antenna array for wireless microwave power transmission," *IEEE Transactions on Antennas and Propagation*, vol. 51, no. 6, pp. 1347-1356, June 2003.

[29] Marco A. B. Terada, "Reflector antennas," in *Encyclopedia of RF and Microwave*

Engineering, K. Chang Ed., vol. 5, pp 4450-4474, New York, John Wiley & Sons, 2005.

[30] J. Huang, "Reflectarray antenna," in *Encyclopedia of RF and Microwave Engineering*, K. Chang Ed., vol. 5, pp 4428-4436, New York, John Wiley & Sons, 2005.

[31] A. Erentok, P. Luljak, and R.W. Ziolkowski, "Characterization of a volumetric metamaterial realization of an artificial magnetic conductor for antenna applications," *IEEE Transactions on Antennas and Propagation*, vol. 53, no. 1, pp. 160–172, Jan. 2005.

[32] K. Buell, H. Mosallaei, and H. K. Sarabandi, "Embedded circuit magnetic metamaterial substrate performance for patch antennas," in *Proc. IEEE AP-S Int. Symp.*, vol. 2, Jun. 2004, pp. 1415–1418.

[33] C. Caloz, C.-J. Lee, D. R. Smith, J. B. Pendry, and T. Itoh, "Existence and properties of microwave surface plasmons at the interface between a right-handed and a left-handed media," in *Proc. IEEE AP-S Int. Symp.*, vol. 3, Jun. 2004, pp. 3151–3154.

[34] A. Saib and I. Huynen, "Transmission lines on periodic bandgap metamaterials: from microwaves to optics applications," *J. Opt. A: Pure andAppl. Opt.*, vol. 7, pp. S124–S132, Jul. 2004.

[35] R. W. Ziolkowski and A. D. Kipple, "Application of double negative materials to increase the power radiated by electrically small antennas," in *IEEE AP-S Int. Symp.*, vol. 51, Oct. 2003, pp. 2626–2640.

[36] W. H. Hardy and L. A. Whitehead, "Split-ring resonator for use in magnetic resonance from 20-2000 MH," *Review of Scientific Instruments*, vol. 52, pp. 213-216, Feb. 1981.

[37] F. Momo, A. Sotgin, and R. Zonta, " On the design of a split ring resonator for ESR spectroscopy between 1 and 4 GHz," *Journal of Physics E: Scientific Instruments*, vol. 16, pp. 43-46, Jan. 1983.

[38] M.V. Kostin, V.V. Shevchenko, “Theory of artificial magnetic substances based on ring currents”, *Journal of Communications Technology and Electronics*, vol.38, no.5, pp. 78-83, 1993.

[39] R. Marqués, F. Medina, and R. Rafii-El-Idrissi, “Role of bianisotropy in negative permeability and left-handed metamaterials,” *Physical Review B*, vol. 65, pp. 144440-1-6, Apr. 2002.

[40] M. Shamonin, E. Shamonina, V. Kalinin, and L. Solymar, “Properties of a metamaterial element: Analytical solutions and numerical simulations for a singly split double ring,” *Journal of Applied Physics*, vol. 95, pp. 3778-3784, Apr. 2004.

[41] M. Shamonin, E. Shamonina, V. Kalinin, and L. Solymar, “Resonant frequencies of a split-ring resonator: Analytical solutions and numerical simulations,” *Microwave and Optical Technology Letters*, vol.44, pp.133-136, Dec. 2004.

[42] C. L. Holloway, E. F. Kuester, J. Baker-Jarvis and P. Kabos, "A double negative (DNG) composite medium composed of magneto dielectric spherical particles embedded in a matrix," *IEEE Transactions on Antennas and Propagation,* vol. 51, pp. 2596-2603, Oct. 2003.

[43] J. Pacheco Jr., T. M. Grzegorczyk, B. -. Wu, Y. Zhang and J. A. Kong, "Power propagation in homogeneous isotropic frequency-dispersive left-handed media," *Physical Review Letter,* vol. 89, pp. 257401-1, Dec. 2002.

[44] M. K. Karkkainen, "Numerical study of wave propagation in uniaxially anisotropic Lorentzian backward-wave slabs," *Physical Review E,* vol. 68, pp. 026602-1, Aug. 2003.

[45] D. C. Wittwer and R. W. Ziolkowski, "Maxwellian material-based absorbing boundary conditions for lossy media in 3-D," *IEEE Transactions on Antennas and Propagation,* vol. 48, pp. 200-213, Feb. 2000.

[46] R. W. Ziolkowski, "Propagation in and scattering from a matched metamaterial having a zero index of refraction," *Physical Review E,* vol. 70, pp. 046608-1, Oct.

2004.

[47] C. R. Simovski, P. A. Belov and S. He, "Backward wave region and negative material parameters of a structure formed by lattices of wires and split-ring resonators," *IEEE Transactions on Antennas and Propagation,* vol. 51, pp. 2582-2591, Oct. 2003.

[48] J. D. Baena, J. Bonache, F. Martin, R. M. Sillero, F. Falcone, T. Lopetegi, M. A. G. Laso, J. Garcia-Garcia, I. Gil, M. F. Portillo and M. Sorolla, "Equivalent-circuit models for split-ring resonators and complementary split-ring resonators coupled to planar transmission lines," *IEEE Trans. Microwave Theory Tech.,* vol. 53, pp. 1451-1460, Apr. 2005.

[49] F. Falcone, T. Lopetegi, J. D. Baena, R. Marqués, F. Martín, and M. Sorolla, "Effective negative-ε stop-band microstrip lines based on complementary split ring resonators," *IEEE Microwave and Wireless Components Letters*, vol. 14, no. 6, pp. 280-282, Jun. 2004.

[50] S. B. Cohn, "Parallel-coupled transmission line resonator filters," *IRE Trans. Microw. Theory Tech.,* vol. MTT-6, pp.223-231, Apr. 1958.

[51] G. L. Matthaei, L. Young, and E. M. T. Jones, *Microwave Filters, Impedance-Matching Network, and Coupling Structures.* Norwood, MA: Artech House, 1980

[52] J. García–García, F. Martín, F. Falcone, J. Bonache, I. Gil, T. Lopetegi, M. A. G. Laso, M. Sorolla, and R. Marqués, "Spurious passband suppression in microstrip coupled line band pass filters by means of split ring resonators," *IEEE Microwave and Wireless Components Letters*, vol. 14, no. 9, pp. 416-418, " Sept. 2004.

[53] M. K. Mandal, P. Mondal, S. Sanyal, and A. Chakrabarty, "Low insertion-loss, sharp-rejection and compact microstrip low-pass filters," *IEEE Microwave and Wireless Components Letters*, vol. 16, no. 11, pp. 600-602, Nov. 2006.

[54] J. D. Baena, J. Bonache, F. Martín, R. M. Sillero, F. Falcone, T. Lopetegi, M. A. G. Laso, J. García–García, I. Gil, M. F Portillo, and M. Sorolla, "Equivalent-circuit models for split-ring resonators and complementary split-ring resonators coupled to

planar transmission lines," *IEEE Transactions Microwave Theory and Techniques*, vol. 53, no. 4, pp. 1451-1461, Apr. 2005.

[55] J. Bonache, I. Gil, J. García–García, and F. Martín, "Novel microstrip bandpass filters based on complementary split-ring resonators," *IEEE Transactions Microwave Theory and Techniques*, vol. 54, no. 1, pp. 265-271, Jan. 2006.

[56] P. Mondal, M. K. Mandal, A. Chakrabarty, and S. Sanyal "Compact bandpass filters with wide controllable fractional bandwidth," *IEEE Microwave and Wireless Components Letters*, vol. 16, no. 10, pp. 540-542, Oct. 2006.

[57] H. Tehrani and K. Chang, "A multi-frequency microstrip-fed annular slot antenna," in *IEEE AP-S Int. Symp. Dig*., 2000, pp. 632-635.

[58] J.S. Chen, "Dual-frequency annular-ring slot antennas fed by CPW feed and microstrip line feed," *IEEE Transactions on Antennas and Propagation*, vol. 53, no. 1, pp. 569-571, Jan. 2005.

[59] C. Hsieh, T. Chiu, and C. Lai, "Compact dual-band slot antenna at the corner of the ground plane," *IEEE Transactions on Antennas and Propagation*, vol. 57, no. 10, pp. 3423-3426, Oct. 2009.

[60] Y. Lee and H. Yang, "Characterization of microstrip patch antennas on metamaterial substrates loaded with complementary split ring resonators ," *Microwave and Optical Technique Letter*, vol. 50, pp. 2131-2135, Aug. 2008.

[61] J. Liu, S. Gong, Y. Xu, X. Zhang, C. Feng, and N. Qi, "Compact printed ultra-wideband monopole antenna with dual band-notched characteristics," *Electronics Letter*, vol. 44, no. 12, 5th Jun. 2008.

[62] H. Zhang, Y.-Q. Li, X. Chen, Y.-Q. Fu, and N.-C. Yuan, "Design of circular/dual-frequency linear polarization antennas basd on the anisotropic complementary split ring reosnator ," *IEEE Transactions on Antennas and Propagation*, vol. 57, pp. 3352-3355, Oct. 2009.

[63] K. Chang, and L.-H. Hsieh, “Microwave ring circuits and related structures” Hoboken, NJ, John Wiley & Sons, 2004.

[64] J. O. McSpadden and J. C. Mankins, “Space solar power programs and microwave ireless power transmission technology,” *IEEE Micro*, vol. 3, no. 4, pp. 46–57, Dec. 2002.

[65] B. H. Strassner and K. Chang, “Microwave power transmission,” in *Encyclopedia of RF and Microwave Engineering*. Hoboken, NJ: Wiley, 2005, vol. 4, pp. 2906–2919.

[66] Y. -H. Suh and K. Chang, “A high-efficiency dual-frequency rectenna for 2.45- and 5.8-GHz wireless power transmission,” *IEEE Transactions Microwave Theory and Techniques*, vol. 50, No. 7, pp.1784-1789, Jul. 2002.

[67] J. O. McSpadden, L. Fan, and K. Chang, “Design and experiments of a high-conversion-efficiency 5.8-GHz rectenna,” *IEEE Transactions Microwave Theory and Techniques*, vol. 46, No. 12, pp.2053-2059, Dec. 1998.

[68] B. Strassner and K. Chang, “5.8-GHz circularly polarized dual-rhombic-loop traveling-wave rectifying antenna for low power-density wireless power transmission applications,” *IEEE Transactions Microwave Theory and Techniques*, vol. 51, No. 5, pp.1548-1553, May 2003.

[69] J. -Y. Park, S. -M. Han, and T. Itoh, “A rectenna design with harmonic-rejecting circular-sector antenna,” *IEEE Antennas and Wireless Propagation Letters*, vol. 3, pp.52-54, 2004.

[70] J. Heikkinen and M. Kivikoski, “Low-profile circularly polarized rectifying antenna for wireless power transmission at 5.8 GHz,” *IEEE Microwave and Wireless Components Letters*, vol. 14, no. 4, pp.162-164, 2004.

[71] M. Ali, G. Yang, and R. Dougal, “A new circularly polarized rectenna for wireless power transmission and data communication,” *IEEE Antennas and Wireless Propagation Letters*, vol. 4, pp.205-208, 2005.

[72] Y. Murao and T. Takano, "An investigation on the design of a transmission antenna and a rectenna with arrayed apertures for microwave power transmission," *Electronics and Communications in Japan*, Part 1, vol. 83, No. 2, pp.1-9, 2002.

[73] L. -H. Hsieh, B. H. Strassner, S. J. Kokel, C. T. Rodenbeck, M. Y. Li, K. Chang, F. E. Little, G. D. Arndt, and P. H. Ngo, "Development of a retrodirective wireless microwave power transmission system," *IEEE AP-S Antennas and Propagation International Symposium Digest*, vol. 2, pp.393-396, Jun. 2003.

[74] K. Hashimoto and H. Matsumoto, "Microwave beam control system for solar power satellite," in *IEEE Proc., Asia-Pacific Radio Science Conference*, pp.616-617, Aug. 2004.

[75] C. Rodenbeck, M. Li, and K. Chang, "A phased-array architecture for retrodirective microwave power transmission from the space solar power satellite," *IEEE MTT-S International Microwave Symposium Digest*, vol. 3, pp.1679-1682, Jun. 2004.

[76] V. F. Fusco and S. L. Karode, "Self-phasing antenna array techniques for mobile communications applications," *IEE Electronics & Communication Engineering Journal*, vol.11, Issue 6, pp.279-286, Dec. 1999.

[77] R. Y. Miyamoto and T. Itoh, "Retrodirective arrays for wireless communications," *IEEE Microwave Magazine*, vol. 3, Issue 1, pp.71-79, Mar. 2002.

[78] W. A. Shiroma, R. Y. Miyamoto, G. S. Shiroma, A. T. Ohta, M. A. Tamamoto, and B. T. Turakumi, "Retrodirective systems," in *Encyclopedia of RF and Microwave Engineering*, K. Chang Ed., Hoboken, NJ, John Wiley & Sons, Inc., vol. 5, pp.4493-4507, 2005.

[79] Y.-J. Ren and K. Chang, "Bow-tie retrodirective rectenna," *IET Eletronics Letters*, vol.42, No. 4, July 2006.

[80] Y.-J. Ren and K. Chang, "New 5.8-GHz circularly polarized retrodirective rectenna arrays for wireless power transmission," *IEEE Transactions Microwave Theory and Techniques*, vol. 54, No. 7, pp.2970-2976, Feb. 2006.

[81] W. C. Brown, “The technology and application of free-space power transmission by microwave beam,” *Proceedings of the IEEE*, vol. 62, no. 1, pp. 11-25, Jan. 1974.

[82] J. O. McSpadden, T. Yoo, and K. Chang, “Theoretical and experimental investigation of a rectenna element for microwave power transmission,” *IEEE Transactions Microwave Theory and Techniques*, vol. 40, No. 12, pp.2359-2366, Dec. 1992.

[83] A. Sedra and K. Smith, Microelectronic circuits, Fourth Edition, New York, Oxford University Press, Inc., 1998.

[84] J. Huang, “Analysis of a microstrip reflectarray antenna for microspacecraft applicati ons,” TDA Progress Report 42-120, pp. 153-173, Feb. 1995.

[85] C. Balanis, *Antenna Theory*, New York, Wiley & Sons, 1982, chap. 15.

[86] A. Yu, F. Yang, A Z. Elsherbeni, J. Huang, and Y. Rahmat-Samii, “Aperture efficienc y analysis of reflectarray antennas,” *Microwave and Optical Technology Letters*, vol. 52, no.2, Feb. 2010.

[87] S. G. Kim, K. Chang, "Ultrawide band transitions and new microwave components us ing double sided parallel strip lines," *IEEE Transactions Microwave Theory and Tech niques*, vol. 2, no. 9, pp. 2148–2152, 2004.

[88] J.X. Chen, J.L. Li, and Q. Xue, "Lowpass filter using offset double-sided parallel-strip lines," *Electron Lett.*, vol. 41, no. 24, pp. 1336–1337, 2005.

[89] J.X. Chen, C.H.K. Chin, K.W. Lau, and Q. Xue, "180° out of phase power divider based on double-sided parallel striplines," *Electronics Letter.*, vol. 42, no. 21, pp. 1229–230, 2006.

[90] K. Chang, "Encyclopedia of RF and Microwave Engineering," Hoboken, NJ, John Wiley &Sons, pp. 780-816, 2005.

[91] Y.C. Zhang, and B.Z. Wang, "Advances in developing transitions in microwave integrated circuits," *Journal of Electronic Science and Technology of China*, vol. 3, no. 1, pp. 40–44, 2005.

[92] Y.H. Suh, and K. Chang, "A wideband coplanar stripline to microstrip transition," *IEEE Microwave and Wireless Components Letters*, vol.11, no.1, pp. 28–29, 2001.

[93] X.Y. Zhang, J.X. Chen, and Q. Xue, "Broadband transition between double sided parallel strip line and coplanar waveguide," *IEEE Microwave and Wireless Components Letters*, vol. 17, no. 2, pp. 103–105, 2007.

[94] R. G. Vaughan, "Polarization Diversity in Mobile Communications", *IEEE Trans. Vehicular Technology*, vol. 39, no.3, Aug. 1990.

[95] C. A. Balanis, "Antenna Theory: Analysis and Design" 3rd ed., Hoboken, NJ, Wiley-Interscience, 2005.

[96] A. Alford and A. G. Kandoian, *"*Ultra-high frequency loop antenna*", Trans. AIEE,* vol.59, pp. 843-848, 1940.

[97] A. J. Fenn, "Arrays of horizontally polarized loop-fed slotted cylinder antennas", *IEEE Trans. Antennas and Propagation,* vol. AP-33, No. 4, pp 375-382, April 1985.

[98] D. S. Kim, C.H. Ahn, Y. T. Im, S. J. Lee, K. C. Lee, and W. S. Park, "A Windmill-shaped Loop Antenna for Polarization Diversity", *IEEE Antennas and Propagation-Society International sym., Honolulu, HI, pp.361-364, June 2007.*

[99] C. C. Lin, L.C. Kuo, and H.-R. Chuang, "A horizontally polarized omnidirectional printed antenna for WLAN applications", *IEEE Trans. Antennas and Propagation*, vol 54, No. 11, part 2, pp 3551-3556, Nov. 2006.

[100] H. R. Chuang, L.C. Kuo, "3-D FDTD design analysis of a 2.4-GHz polarization-diversity printed dipole antenna with integrated balun and polarization-switching circuit for WLAN and wireless communication applications", *IEEE Trans. Microwave Theory and Techniques,* vol. 51, No. 2, part 1, pp 374-381, Feb. 2003.

[101] Wheeler, H. A., "Transmission-line properties of parallel wide strips by a conformal mapping approximation," *IEEE Transactions Microwave Theory and Techniques,* vol. MTT-12, pp. 280-289, May 1964.

[102] Wheeler, H. A., “Transmission-line properties of parallel wide strips separated by a dielectric sheet,” *IEEE Transactions Microwave Theory and Techniques,* vol. MTT-12, pp. 172-185, May 1965.

VITA

Chi Hyung Ahn was born in Samchuk, Republic of Korea. He received his B.S. degree in electrical engineering from Inha University, Korea, in 2002., and his M.S. degree in electronic engineering from Pohang University of Science and Technology, Korea, in 2004. From 2004 to 2005, he was a visiting researcher with the Microwave Electronics Laboratory, University of California at Los Angeles and involved in 2-D metamaterial structure modeling. From 2005 to 2006, he worked at Agilent Korea as technical sales. In 2007, he began working towards his Ph.D. degree in electrical and computer engineering at Texas A&M University, College Station, TX, and was directed by Prof. Kai Chang in the Electromagnetics and Microwave Laboratory. His research interests include conformal antenna arrays, electrically small and multiband antennas, and microwave metamaterial applications, and wireless power transmission. He may be reached through Professor Kai Chang, Department of Electrical and Computer Engineering, Texas A&M University, College Station, TX 77843-3128.